

Surface Chemistry and Corrosion Studies of Zn–Al and Zn–Mg–Al Alloy Coatings

PhD Thesis

Dr. rer. nat.

Faculty of Science
at the
University of Paderborn

submitted by
Katharina Pohl
from Nürtingen

Paderborn, 2013

Defence: 30.04.2013

First referee: Prof. Dr.–Ing. G. Grundmeier

Second referee: Prof. Dr. M. Tiemann

Ich versichere, dass ich diese Arbeit eigenständig verfasst und keine anderen als die angegebenen Quellen und Hilfsmittel benutzt, sowie Zitate kenntlich gemacht habe.

Index

<i>Acknowledgement</i>	v
<i>Abstract</i>	vi
1 State of research and motivation	1
2 Fundamentals	4
2.1 <i>Corrosion of zinc and zinc alloy coated steel</i>	4
2.1.1 <i>General corrosion mechanism under atmospheric conditions</i>	4
2.1.2 <i>General corrosion mechanism under full immersion</i>	9
2.1.3 <i>In-situ Raman spectroscopic analysis of zinc corrosion products</i>	13
2.2 <i>Molecular adhesion on aluminum and zinc oxides</i>	14
2.2.1 <i>Adsorption of monolayers</i>	15
2.2.2 <i>Understanding of interfacial bond formation</i>	18
2.3 <i>Fundamentals of adhesion and de-adhesion of polymers on oxide covered metals</i> 19	
2.3.1 <i>Wet de-adhesion</i>	20
2.3.2 <i>Corrosive de-adhesion of polymers on zinc substrates</i>	21
2.4 <i>Raman spectroscopic analysis of polymer/metal interface</i>	22
3 Theoretical background of applied analytical techniques	25
3.1 <i>Spectroscopic techniques</i>	25
3.1.1 <i>Raman spectroscopy</i>	25
3.1.2 <i>Infrared spectroscopy</i>	27
3.1.3 <i>X-ray photoelectron spectroscopy (XPS)</i>	29
3.2 <i>Electrochemical techniques</i>	30
3.2.1 <i>Scanning Kelvin probe (SKP)</i>	31
3.2.2 <i>Cyclic voltammetry (CV)</i>	32
3.2.3 <i>Scanning Kelvin probe force microscopy (SKPFM)</i>	33
3.3 <i>Microscopic techniques</i>	35
3.3.1 <i>Scanning electron microscopy (SEM)</i>	35
3.3.2 <i>Atomic force microscopy (AFM)</i>	36

3.4	Contact angle measurement.....	37
4	In-situ corrosion analysis of zinc alloy coated steel	39
4.1	Experimental	39
4.1.1	Materials and sample preparation	39
4.1.2	Surface Analysis.....	40
4.1.3	In-situ Raman spectroscopy	40
4.2	Surface morphology and microstructure	41
4.3	Bulk composition of the alloy.....	44
4.4	Electronic surface properties.....	47
4.5	Corrosion processes and mechanisms at different pH.....	50
4.6	Conclusions.....	58
5	In-situ corrosion analysis of zinc magnesium alloy coated steel.....	59
5.1	Experimental	59
5.1.1	Materials and sample preparation	59
5.1.2	Surface Analysis.....	60
5.1.3	In-situ Raman spectroscopy	60
5.2	Surface morphology and bulk composition of the alloy.....	60
5.3	Corrosion process and mechanisms at different pH	63
5.4	Conclusions.....	70
6	In-situ corrosion analysis of oxide covered iron/ zinc alloy cut edges	72
6.1	Experimental	72
6.1.1	Materials and sample preparation	72
6.1.2	Surface Analysis.....	72
6.1.3	In-situ Raman spectroscopy	73
6.2	Cut edge morphology and chemistry	73
6.3	Corrosion process and mechanism.....	75
6.4	Conclusions.....	79

7 Adsorption and stability of self-assembled organophosphonic acid monolayers on plasma modified Zn–Mg–Al alloy surfaces.....	80
7.1 <i>Experimental</i>	80
7.1.1 <i>Materials and Sample Preparation</i>	80
7.1.2 <i>Plasma Surface Chemistry</i>	81
7.1.3 <i>Adsorption and Self-Organization of Organic Acids</i>	81
7.1.4 <i>Surface Analysis</i>	81
7.2 <i>Plasma surface chemistry</i>	83
7.3 <i>Adsorption and self-organization of organic acids</i>	91
7.4 <i>Stability of organic acids on Zn–Mg–Al alloys</i>	96
7.5 <i>Blocking of surface sites oxide covered on Zn–Mg–Al alloys by ODPA SAMs</i>	98
7.6 <i>Conclusions</i>	100
8 Surface chemistry and adhesive properties of plasma modified Zn–Mg–Al alloy coatings	101
8.1 <i>Experimental</i>	101
8.1.1 <i>Modification of the surface by plasma treatment</i>	101
8.1.2 <i>Application of adhesion promoter and the model polymer coating</i>	102
8.1.3 <i>Characterization of the surface chemistry after plasma treatments and APPA adsorption</i>	102
8.1.4 <i>Peel-test measurements</i>	103
8.2 <i>Characterization of the plasma modified samples</i>	103
8.3 <i>Adsorption of APPA on the plasma modified sample surface</i>	108
8.4 <i>The effect of plasma treatments and APPA adsorption on the adhesion of epoxy amine coating on Zn–Mg–Al alloy surfaces</i>	113
8.5 <i>Conclusions</i>	115
9 Overall conclusions and outlook	116
References	119

Abbreviations and symbols 127

List of Figures 129

List of Tables 134

List of Publications 135

Curriculum Vitae 137

Acknowledgement

The present work was performed at the University of Paderborn (UPB) and the Max–Planck–Institute for iron research (MPIE) in the working group of Prof. Dr.–Ing. Guido Grundmeier. I would like to thank him for the opportunity to work under his supervision in Düsseldorf and Paderborn. He always had an open ear and helped me to improve my scientific work with his support and productive discussions.

I would like to thank Prof. Dr. Michael Tiemann for reviewing my thesis and giving me his support.

I would like to thank Dr. Özlem Özcan for many fruitful discussions and for helping me with the corrections of the present work. Further, I would like to thank Dr. Miroslaw Giza. In our collaboration I had the opportunity to learn a lot about hot dipped galvanized steel and X–ray photon spectroscopy.

I am grateful to my dear colleagues M.Sc. Agata Pomorska, Dipl.Chem. Romy Regenspurger, M.Sc. Sandra Szilles, Dr. Berkem Özkaya, M.Sc. Christoph Ebbert and M.Sc. Markus Wiesner who supported me with their comments and helped me anytime. I would also like to thank my former colleagues Dr. Nicole Fink, Dr. Monika Santa and M.Sc. Julia Klemm for the sometimes not technical but always interesting and gainful discussions. Further, I would like to thank Nicole, Brooke and René for the help in technical questions.

Special thanks go to my family. They always supported me and the patience they had during the last years. Last but not least I would like to thank Josef for the support and patience he had during the preparation of this work.

The present work was carried out with the financial support of the Deutsche Forschungsgemeinschaft (DFG) and the Christian Doppler Society.

Abstract

Alloy coated steel is one of the main raw materials of automobile, appliance and construction industries. Binary or ternary mixtures of zinc (Zn), aluminum (Al) and magnesium (Mg) are the most frequently used alloy coatings to increase the corrosion resistance of steel. In most cases the steel sheets are additionally coated with polymeric layers like paints or adhesives.

The design and development of corrosion resistant polymer/zinc interfaces are of high importance for organically coated or adhesively bonded galvanized steel substrates [1–4].

The aim of the present work is to contribute towards a better understanding of the corrosion mechanisms on zinc alloys and to investigate, based on this fundamental knowledge, the applicability of organophosphonic acids for corrosion protection and adhesion promotion on novel Zn–Mg–Al alloys. Even though there is extensive amount of data in the literature on the macroscopic corrosion properties and corrosion resistance of zinc alloy coatings, initial stages of the corrosion processes and the influence of the microstructure of the alloy coating on the corrosion mechanisms is not clarified so far. The chapters 5 – 7 are thus devoted to the analysis of initial stages of corrosion processes by means of in-situ Raman spectroscopy. The influence of the pH and the variation of the electrolyte exchange rate were investigated.

Moreover, the adsorption and stability of organophosphonic acid monolayers on plasma modified Zn–Mg–Al alloys was studied by means of spectroscopic and microscopic techniques. The chemical composition of the plasma treated surfaces and the influence of reducing and oxidizing plasma modifications on the corrosion resistance of zinc magnesium aluminum alloy surfaces was analyzed by means of XPS and cyclic voltammetry, respectively. Furthermore, aminopropylphosphonic acid was investigated as a short-chain bi-functional adhesion promoter between a plasma modified zinc magnesium aluminum alloy coated steel and an epoxy amine adhesive. By means of X-ray photoelectron spectroscopy (XPS) analysis and scanning Kelvin probe (SKP), plasma induced changes of the passive layer were demonstrated.

1 State of research and motivation

The corrosion resistance and the adhesion strength of organic coatings on oxide covered alloys are mainly determined by the surface composition of the alloy, the composition of the organic coating and the interface chemistry between the surface oxides and the coating [1; 5–7]. To be able to substitute surface treatment technologies with high environmental impact such as anodizing or conversion chemistry, new adhesion promoting, ultra–thin films of inorganic or organic compounds have been investigated as advanced interfacial layers for polymer coated aluminum alloys [8–12] and zinc coated steel [1; 3; 5; 13; 14].

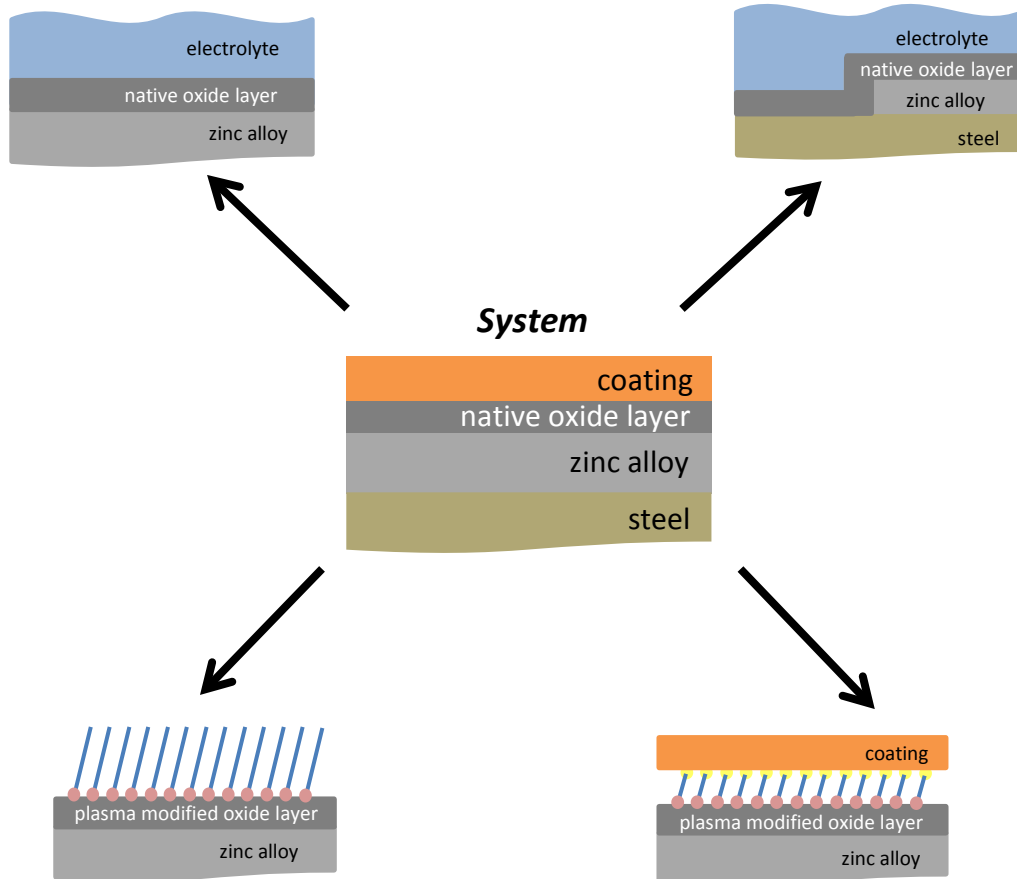
The corrosion mechanisms on alloy coated steel depend strongly on the pH and the CO₂ amount in the electrolyte where carbonate species can form at high pH. Moreover, the chloride concentration and the cations play an important role in the kinetics of the corrosion [15–54]. The presence of defects in the organic coating can cause the corrosive electrolytes to reach the alloy surface which lead to delamination processes. The delamination process of painted zinc coated steel sheets is influenced by various factors such as the water and oxygen permeability of the coating and the adhesion of the coating to the metal oxide surface.

Newly developed Zn–Mg–Al alloys provide increased corrosion protection both with and without an additional polymeric coating in comparison to pure zinc [17; 31; 33; 55–59]. Their surface is covered by a thin oxide film that is mainly composed on MgO, Al₂O₃ and ZnO and their hydroxides [42; 55; 60; 61]. These thin films exhibit special electronic properties that make them suitable for the direct application of thin organic coatings without the need for application of a chemical conversion process [10; 55; 60]. Characterization of Zn–Mg alloy surfaces and the delamination of organic coatings by means of a scanning Kelvin probe were reported by Rohwerder et al. [41; 60]. It was shown that potentials more negative than the free corrosion potential of zinc can be observed under atmospheric conditions with and without a polymer coating. Surface plasma modification [10; 55] and the formation of self–assembled monolayers on metals [10; 55; 62; 63] have been established as surface technologies which do not lead to chemical etching of the metal substrate. Grundmeier et al. illustrated how oxide–covered iron and zinc can be modified with regard to their surface chemistry and oxide thickness [64; 65]. Plasma treatment of stainless steel was investigated

by Kalin et.al. [66]. They showed a strong plasma effect on the microhardness of the surface and layers of 40–60 pm in depth. Very recently, Giza and Grundmeier have shown that Zn–Mg alloy surfaces can be adjusted in their surface potential very effectively by application of reducing and oxidizing plasma treatments [55].

Chapter 5 +6: *In-situ corrosion analysis of zinc alloy coated steel*

Chapter 7: *In-situ corrosion analysis of oxide covered iron/zinc alloy cut edges*



Chapter 8: *Adsorption and stability of self-assembled organophosphonic acid monolayers on plasma modified Zn–Mg–Al alloy surfaces*

Chapter 9: *Surface chemistry and adhesive properties of plasma modified Zn–Mg–Al alloy coatings*

Figure 1.1: *Schematic overview of the scientific approach followed in the present study.*

The aim of the present work is to contribute towards a better understanding of the corrosion mechanisms on zinc alloys and to investigate, based on this fundamental knowledge, the applicability of organophosphonic acids for corrosion protection and adhesion promotion on novel Zn–Mg–Al alloys (Figure 1.1). Even though there is extensive amount of data in the literature on the macroscopic corrosion properties and corrosion resistance of zinc alloy coatings, initial stages of the corrosion processes and the influence of

the microstructure of the alloy coating on the corrosion mechanisms is not clarified so far. The chapters 5 – 7 are thus devoted to the analysis of initial stages of corrosion processes by means of in-situ Raman spectroscopy. The influence of the pH and the variation of the electrolyte exchange rate were investigated.

The adsorption and stability of phosphonic acids on plasma modified Zn–Mg–Al alloys was studied by means of spectroscopic and microscopic techniques. The chemical composition of the plasma treated surfaces and the influence of reducing and oxidizing plasma modifications on the corrosion resistance of zinc magnesium aluminum alloy surfaces were analyzed by means of X-ray photoelectron spectroscopy (XPS) and cyclic voltammetry, respectively.

Furthermore, aminopropylphosphonic acid was investigated as a short-chain bi-functional adhesion promoter between a plasma modified zinc magnesium aluminum alloy coated steel and an epoxy amine adhesive. By means of XPS analysis and scanning Kelvin probe (SKP), plasma induced changes of the passive layer were demonstrated.

2 Fundamentals

Zinc coatings protect the underlying steel in various ways. In general, the zinc coating acts as a barrier layer and separates the steel from the corrosive environment. Zinc itself acts as a sacrificial anode to galvanically protect the underlying steel at defects, scratches and cut edges of the zinc coating [44–46; 53].

This chapter deals with the corrosion of zinc and its alloys, adhesion and corrosive delamination of coatings and the functionalization of the metal surface by monolayers to increase the corrosion resistance.

2.1 Corrosion of zinc and zinc alloy coated steel

Zinc exposed to the atmosphere is covered by a thin and amorphous layer of zinc oxide/hydroxide and when immersed in an electrolyte, these pores play the role of local anodes. Many tests have been established to compare the corrosion properties of Zn alloys under various experimental conditions [15–54].

Corrosion tests can be classified into two main groups, depending on the type of the chosen corrosive load. The first group of tests is conducted under atmospheric conditions. The most common atmospheric corrosion test is the salt spray test simulating discontinuous but repetitive exposure of the samples to corrosive electrolyte [31; 32]. The second group of tests is conducted in immersion mode and simulates the continuous exposure of the samples to the corrosive electrolyte. Salt spray and immersion tests are today the standard testing procedures of automobile and marine industries, respectively.

2.1.1 General corrosion mechanism under atmospheric conditions

In studies performed under atmospheric conditions, the electrolyte composition, humidity, temperature, CO₂ amount was varied and the influence of the cations on the corrosion mechanism was investigated [16–18; 24–32; 59; 67]. In Figure 2.1 an overview of the observed corrosion products on pure zinc is presented.

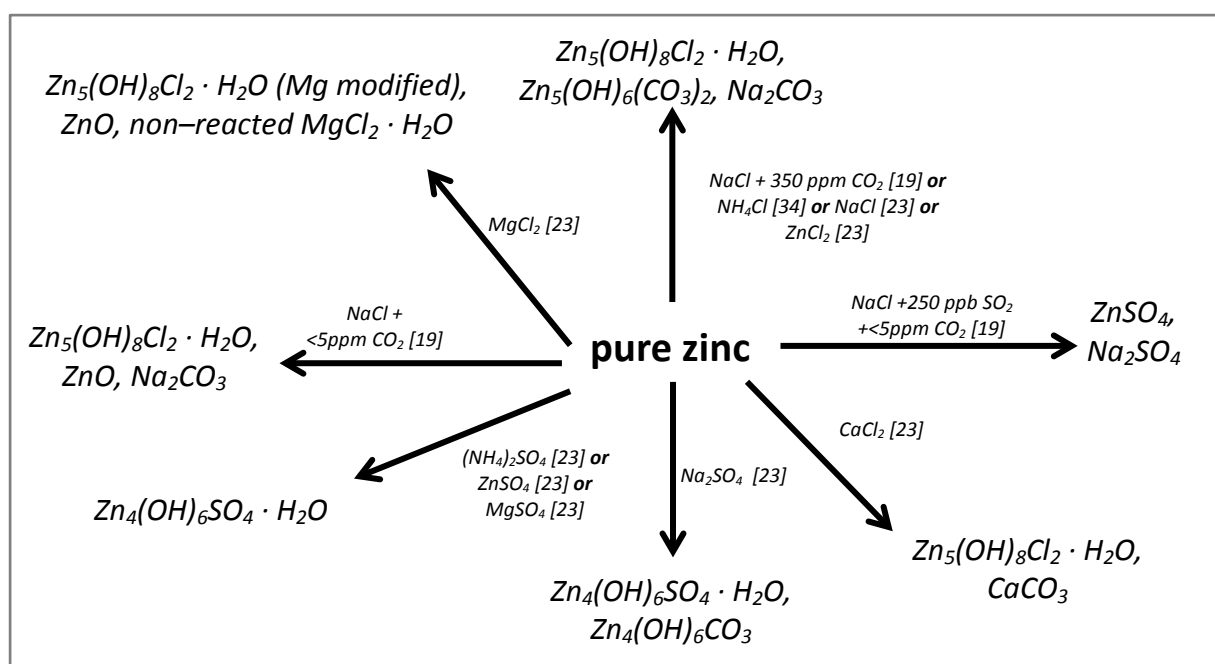


Figure 2.1: General overview of solid corrosion products on pure zinc observed with different electrolyte under atmospheric conditions and long-time exposure.

The chloride containing electrolytes lead to the building of simonkolleite ($Zn_5(OH)_8Cl_2 \cdot H_2O$). Lindström et al. [29] exposed zinc samples with deposits of chlorides and sulphates of sodium, magnesium, ammonium, and zinc to humid air at relative humidity of 95%, temperature of 22° C and carbon dioxide (CO_2) concentration of 350 ppm. The highest metal loss occurred for the samples treated with sodium chloride (NaCl) and sodium sulphate (Na_2SO_4). In the presence of these two salts, a mixture of corrosion products containing large amounts of carbonate was formed. In contrast, the samples treated with other salts primarily formed zinc hydroxychloride ($Zn_5(OH)_8Cl_2 \cdot H_2O$) or zinc hydroxysulphate ($Zn_4SO_4(OH)_6 \cdot H_2O$) in the presence of chlorides and sulphates. The different behavior between sodium, and magnesium and zinc salts was explained by inhibition of cathodic reaction in the presence of Zn^{2+} and Mg^{2+} . These cations form less soluble salts tend to precipitate in a form of hydroxide, oxide, or hydroxy salts in the cathodic areas, which are consequently blocked and unable to act as cathodes. It was also shown that the corrosion rate of zinc in the atmosphere was related to the amount of sodium present on the surface, rather than the amount of chloride or sulphate.

The influence of CO_2 and SO_2 on initial corrosion and secondary spreading effects during NaCl particle induced corrosion on zinc was investigated by Chen et al [25]. The secondary

spreading effect which occurs upon introduction of humid air on NaCl deposited zinc surfaces was strongly dependent on the CO₂ and SO₂ content of the introduced air. Ambient level of CO₂ (350 ppm) resulted in a relatively low spreading effect, whereas the lower level of CO₂ (<5 ppm) caused a much faster spreading over a larger area. The corrosion decreased slightly for NaCl contaminated surfaces when SO₂ was present. This was explained in the report of Svensson et al. [67] by precipitation of zinc hydroxysulphate which decreased the corrosion rate via blocking of the anodic and cathodic sites.

At <5 ppm CO₂, the corrosion was shown to occur more localized, with the formation of simonkolleite (Zn₅(OH)₈Cl₂ · H₂O), zincite (ZnO) and sodium carbonate (Na₂CO₃), and a larger effective cathodic area. At 350 ppm CO₂, the corrosion products simonkolleite, hydrozincite (Zn₅(OH)₆(CO₃)₂) and sodium carbonate and the formation of a larger anodic area was observed. Sodium carbonate was mainly formed in more alkaline areas, in the inner edge of the electrolyte droplet and in the secondary spreading area. Oxidation of sulphur and concomitant sulphate formation was enhanced in the presence of NaCl particles, due to the formation of a droplet, the separation of the anodic and cathodic areas and the accompanying differences in chemical composition and pH in the surface electrolyte.

The effect of different cations on the atmospheric corrosion of carbon steel and zinc was performed by Prosek et al [16], to understand better the role of cations in corrosion processes on metal surfaces being in contact with wet air. The corrosivity of cations of chloride salts for zinc increased in order of Mg²⁺ < Ca²⁺ < Na⁺. The higher corrosion resistance of zinc treated with calcium and magnesium chlorides was connected to prevention of formation of hydrozincite during zinc exposure in wet air. It was observed that zinc weight loss and the carbonate to simonkolleite ratio in corrosion products were correlating well. The principal protective effect of bivalent cations can be seen in the decrease of pH of the surface electrolyte, which was caused by hydrolysis of such cations and subsequent formation of simonkolleite which blocked the cathodic sites.

Furthermore, model zinc–magnesium alloys containing 1–32 wt.% magnesium were analyzed in comparison to pure zinc and pure magnesium [17]. The samples were contaminated with sodium chloride and exposed to humid air for 28 days. The composition of corrosion products was analyzed by means of infrared spectroscopy (FTIR), ion

chromatography (IC), and Auger electron spectroscopy (AES). The corrosion products identified on the samples are listed in Table 2.1.

Table 2.1: Composition of corrosion products on Zn, Zn–Mg, and Mg contaminated with chloride after exposure to humid air [17].

substrate	wt%	corrosion products
pure Zn	100% Zn	hydrozincite $[\text{Zn}_5(\text{OH})_6(\text{CO}_3)_2]$, simonkolleite $[\text{Zn}_5(\text{OH})_8\text{Cl}_2 \cdot \text{H}_2\text{O}]$, sodium carbonate $[\text{Na}_2\text{CO}_3]$
ZnMg1	99% Zn, 1% Mg	hydrozincite $[\text{Zn}_5(\text{OH})_6(\text{CO}_3)_2]$, (less) simonkolleite $[\text{Zn}_5(\text{OH})_8\text{Cl}_2 \cdot \text{H}_2\text{O}]$
ZnMg2	98% Zn, 2% Mg	hydrozincite $[\text{Zn}_5(\text{OH})_6(\text{CO}_3)_2]$, (traces of) simonkolleite $[\text{Zn}_5(\text{OH})_8\text{Cl}_2 \cdot \text{H}_2\text{O}]$
ZnMg4	96% Zn, 4% Mg	hydrozincite $[\text{Zn}_5(\text{OH})_6(\text{CO}_3)_2]$, (traces of) simonkolleite $[\text{Zn}_5(\text{OH})_8\text{Cl}_2 \cdot \text{H}_2\text{O}]$
ZnMg6	94% Zn, 6% Mg	hydrozincite $[\text{Zn}_5(\text{OH})_6(\text{CO}_3)_2]$
ZnMg8	92% Zn, 8% Mg	hydrozincite $[\text{Zn}_5(\text{OH})_6(\text{CO}_3)_2]$
ZnMg16	84% Zn, 16% Mg	hydrozincite $[\text{Zn}_5(\text{OH})_6(\text{CO}_3)_2]$, magnesite $[\text{MgCO}_3]$
ZnMg32	68% Zn, 32% Mg	brucite $[\text{Mg}(\text{OH})_2]$, magnesite $[\text{MgCO}_3]$, possibly sodium carbonate $[\text{Na}_2\text{CO}_3]$
pure Mg	100% Mg	magnesite $[\text{MgCO}_3]$, nesquehonite $[\text{MgCO}_3 \cdot 3\text{H}_2\text{O}]$

For all of the analyzed Zn–Mg alloys with deposited sodium chloride, Zn–based corrosion products dominated in the outer layer of the surface film. They were mixed with a substantial quantity of oxidized magnesium, which was higher than Mg content in the bulk alloys. The relative quantity of oxidized magnesium increased with the depth. They showed that Mg–based products formed an intermediate layer at the oxide/metal interface. The improved corrosion resistance of zinc–magnesium alloys was claimed to be connected with the formation of a magnesium–based film on the metal surface, which ensures stable passivity in chloride environment and limits the efficiency of oxygen reduction.

Two explanations for the enhanced corrosion performance of PVD produced Zn–Mg coatings in chloride containing environment is given by Kawafuku et al. [68]: the formation of a dense layer of simonkolleite, $\text{Zn}_5(\text{OH})_8\text{Cl}_2 \cdot \text{H}_2\text{O}$, plus the long lasting cathodic protection of the novel coating during corrosion. As mentioned earlier, simonkolleite is believed to improve corrosion resistance properties and was detected on electrogalvanized samples together

with zinc oxide. However, on Zn–Mg coated samples produced via PVD only simonkolleite with no additional corrosion product was detected.

Morishita et al. [69–71] carried out X-ray diffraction measurements on Zn–Mg coated corrosion test panels dipped in 5 wt.% sodium chloride solution and found magnesium oxide, beside zinc oxide, zinc hydroxide and simonkolleite on the surface. Comparative samples of pure magnesium, exposed to the same conditions as the Zn–Mg coated specimen, showed magnesium hydroxide as the only corrosion product. Due to the fact that magnesium hydroxide is very porous and non-adherent, this corrosion product will not provide sufficient corrosion protection and has no influence on the enhanced corrosion performance. The authors suppose magnesium oxide to play an important role in the corrosion mechanism, mostly because of morphological rather than chemical effects.

In a later study, a Zn–Mg coating produced via PVD technique was tested in a standard automotive laboratory corrosion test comprising salt spraying, drying and humidity cycles [28]. They found a suppression of corrosion because of the formation of simonkolleite layers on the surface which acts as a barrier for further corrosive attacks. Moreover, the oxygen reduction at cathodes is suppressed by the formation of magnesium hydroxide, $Mg(OH)_2$, which is transformed into a carbonate-containing hydroxide in a next step.

Tsujimura et al. [72] analyzed the behavior of Zn–Al–Mg coatings exposed to a cyclic corrosion test including alternating periods of salt spraying, drying and humidity. The system containing 6 wt.% aluminum and 3 wt.% magnesium showed the best corrosion performance of all samples and simonkolleite was detected as the only corrosion product. Systems containing 4.5 wt.% aluminum and 0.1 wt.% magnesium also form zinc oxide and zinc hydroxide beside simonkolleite. The authors assume that, among others, the main reason for the enhanced corrosion performance is the formation of a magnesium-containing simonkolleite species.

Investigations on artificial rust particles synthesized from aqueous solutions dissolving $ZnCl_2$, $AlCl_3$ and $MgCl_2$ were carried out by Ishikawa et al. [73]. The formed rust consists of mixed hydroxide chlorides of Zn(II), Al(III) and Mg(II) $[Zn(II)_wAl(III)_xMg(II)_y]^{(2w+3x+2y)+} (OH)_{2w+3x+2yz} Cl_z \cdot nH_2O$ and appears in form of plate particles. Their ability to agglomerate in a dense, compact layer is suggested to be the main reason for the enhanced corrosion resistance of Zn–Al–Mg alloys.

Schuerz et al [31; 32] studied the corrosion behavior of Zn–Al–Mg coatings prepared by hot–dip galvanizing. Conventional hot–dip galvanized zinc coated (Z) and novel hot–dip galvanized Zn–Al–Mg alloy coated (ZM) steel sheet samples with a coating thickness of 7 μm were exposed to standardized salt spray test and cross–sections of the corrosion samples were analyzed by using SEM and EDX. They observed that Z corrosion proceeds very fast and the steel substrate was attacked even after 100 h of exposure. ZM samples showed a different behavior where the entire metallic ZM coating was converted into a stable, adherent aluminum–rich oxide layer, which protected the steel substrate against corrosive attacks. This layer was claimed to be the main reason for the enhanced corrosion resistance of the ZM coating in sodium chloride–containing environment.

2.1.2 General corrosion mechanism under full immersion

To study in more detail the corrosion mechanism immersion corrosion tests in chloride containing environment were performed. The stability of the corrosion products was shown to depend on the chloride concentration and the pH (Figure 2.2).

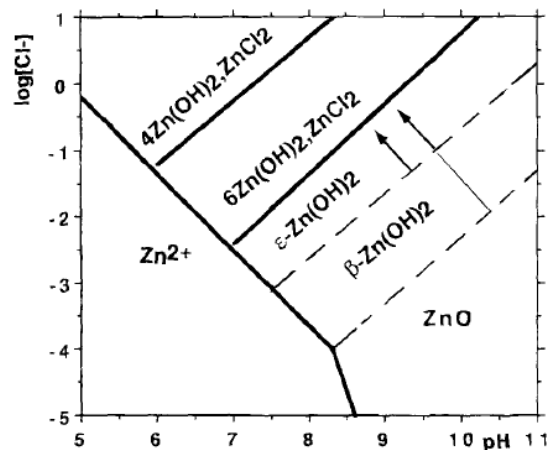


Figure 2.2: Stability diagram of zinc corrosion products taken from Reference [21].

Feitknecht [74–76] developed a theory of corrosion in chloride containing aqueous solution by means of investigating local micro–electrodes and studied the appearance of corrosion products in different zones, associated to local variations of pH. The complexity of the redox reactions which can take place in such conditions is illustrated in Figure 2.3.

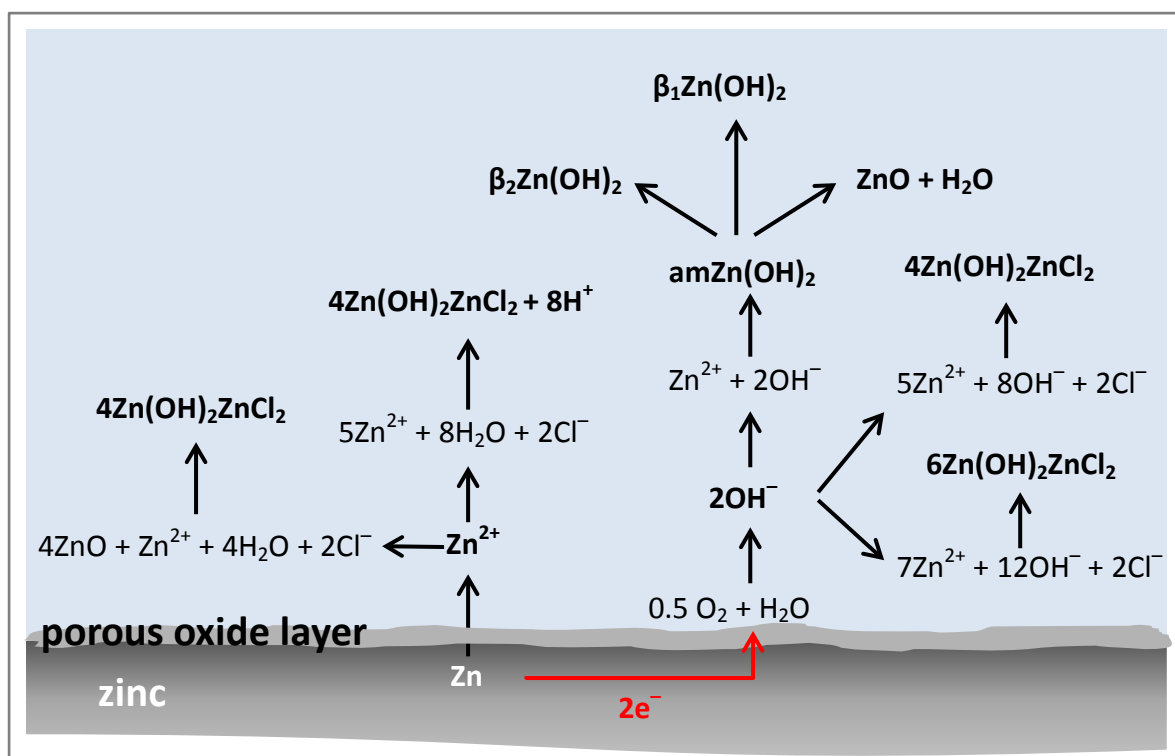


Figure 2.3: Scheme of the corrosive reaction in 0.5 M NaCl and the formation of possible corrosion products [74–76].

Dafydd et al [34] investigated the oxygen reduction reaction by rotating disc electrode in 0.86 M (5%) aqueous sodium chloride containing 0.05 M disodiumtetraborate ($\text{Na}_2\text{B}_4\text{O}_7 \cdot 10\text{H}_2\text{O}$) and 0.07 M NaOH, which gave a buffered pH of 9.6. Zinc in deaerated solution showed current peaks due to the quasi-reversible oxidation of surface zinc to Zn(OH)_2 . Aluminum remained hydroxide covered throughout the process and the voltammetric charge calculated by integration under the current peaks was roughly proportional to the volume fraction of zinc present in the alloy composition. To this extent, the zinc component of alloy coatings behaved electrochemically like free zinc. The potential dependent state of zinc at the metal–electrolyte interface was claimed to determine the pathway of cathodic O_2 reduction. Cathodic current–potential curves obtained from the $\text{Zn}_{0.1}\text{Al}$ alloy coating in aerated solution have shown two diffusion limited current regions. These correspond to a predominantly $2e^-$ reduction process occurring at potentials where zinc was Zn(OH)_2 covered and a predominantly $4e^-$ reduction process occurring at potentials where zinc was in bare metal state. Other Zn–Al coatings did exhibit similar cathodic current–potential characteristics. However, for $\text{Zn}_{4.3}\text{Al}$ limiting currents in the Zn(OH)_2 covered region were increased, corresponding to the stoichiometric number of electrons (ne^-) = 2.8 at 0.86 V. For

Zn55Al limiting currents in the bare zinc region were decreased, corresponding to $ne^- = 2.8$ at 1.06 V. These findings were consistent with $ne^- = 2.8$ at 0.86 V vs SHE on the Zn–Al eutectic phase present within both the Zn4.3Al and Zn55Al coatings, with the aluminum–rich phase in Zn55Al remaining substantially inert.

All Zn–Al alloy coatings have shown considerably lower overpotentials for $2e^- O_2$ reduction than pure zinc, for which no limiting currents were observed in the $Zn(OH)_2$ covered region. Aluminum itself was virtually inert as an O_2 cathode and the higher activity of the Zn–Al coatings was therefore ascribed to electrocatalysis by traces of iron derived from the steel substrate and incorporated into the coatings during hot–dipping. Rates of $2e^-$ cathodic O_2 reduction on the Zn–Al alloy coatings remained substantially diffusion controlled up to the free corrosion potential. Consequently, under free corrosion conditions the stable HO_2 and H_2O_2 products of $2e^- O_2$ reduction were likely to accumulate to levels at which they might reasonably be expected to influence processes of organic coating failure.

Bernard et al. [21] identified the different corrosion products on pure and electrodeposited zinc specimens during exposure to sodium chloride solutions with varying amount of oxygen. Additionally, the influence of polarization on the building of zinc corrosion products was also studied. The morphology and the crystallographic structure of the corrosion products were analyzed by scanning electron microscopy and X–ray diffraction. In order to analyze the influence of the pH on the modification of $Zn(OH)_2$, two different sodium hydroxide solutions were used. The substrate, electrolyte composition, exposing time and electrochemical treatment used in these works are listed in Table 2.2 with the observed corrosion products.

On pure zinc samples exposure times up to three days showed the building of ZnO products. In the case of decarbonated solution crystallized ZnO was found. Longer exposure times showed the formation of $Zn(OH)_2$ and $ZnCl_2$ formation with vary amount of these two components. The absence of $ZnCO_3$ in these cases was only observed in decarbonated solutions. This was also observed on electrodeposited zinc layers. In the case of low concentrated sodium chloride solution after seven days only different modifications of zinc hydroxide was observed.

Table 2.2: Corrosion products observed during in-situ corrosion experiments in chloride containing environment.

substrate	electrolyte	exposed time	electrochemical treatment	corrosion products
pure zinc	0.03 M NaCl	12 days	polarization at -1V/SCE	$3\text{Zn(OH)}_{2-x}\text{Cl}_x \cdot 2\text{ZnCO}_3$ [21]
	0.5 M NaCl	7 days	–	Inner layer $4\text{ZnOH}_2\text{ZnCl}_2$ [21]
	decarbonated 0.03 M NaCl	3 days	galvanostatic conditions: 0.1 mA/cm^2	crystallized ZnO [21]
	0.03 M NaCl	2 days	polarization at -1V/SCE	amorphous ZnO [21]
	0.1 M NaOH	30 days	–	$\epsilon\text{-ZnOH}_2$ [21]
	0.5 M NaOH	30 days	–	$\gamma\text{-ZnOH}_2$ [21]
	5M KOH + 0.5 M ZnO			cathodic polarization (-1.549 V)
			anodic polarization (-1.25 V , 30mA/cm^2)	ZnO, Zn(OH)_4^{2-} [77]
10 min / 4 h			anodic polarization (-1.1 V)	10 min: ZnO, Zn(OH)_4^{2-} 4h: ZnO, Zn(OH)_4^{2-} [77]
electro-deposited zinc layer	decarbonated 0.03 M NaCl	4 days	anodic polarization 0.022 mA/cm^2	$\epsilon\text{-ZnOH}_2$ 4ZnOH_2 , ZnCl_2 [21]
	decarbonated 0.03 M NaCl	9 days	anodic polarization 0.022 mA/cm^2	6ZnOH_2 , ZnCl_2 [21]
	0.03 M NaCl	7 days	–	$\beta\text{-ZnOH}_2$, $\gamma\text{-ZnOH}_2$, $\epsilon\text{-ZnOH}_2$ [21]

Hugot Le Goff [77] studied the corrosion products in high concentrated potassium hydroxide electrolyte with ZnO and the influence of cathodic and anodic polarization (Table 2.2). Under these conditions, ZnO was found to be the main component of passive or blocking layers on zinc without traces of hydroxide. They suggest two different formation mechanisms of the passive layer under these polarization potentials:

- Near the dissolution peak, passivation was induced by precipitation of zinc oxide on the electrode surface from a supersaturated zincate electrolyte.
- In the passive range, passivation was observed due to the growth of a zinc oxide layer by a solid-state mechanism.

2.1.3 In-situ Raman spectroscopic analysis of zinc corrosion products

Raman spectroscopy allows the identification of several products likely to form during corrosion of zinc immersed in chloride-containing solutions. Furthermore, it enables the identification of each of the crystalline species of the same category of compounds, such as zinc hydroxide [21; 77; 78].

Bernard et al. [21; 78] identified amorphous and native ZnO, ϵ -ZnOH₂, β -ZnOH₂ and 4ZnOH₂ZnCl₂ by means of in-situ Raman spectroscopy. The corrosion conditions and the arising corrosion products are listed in Table 2.2 in the previous paragraph. They confirmed their results obtained with the Raman analysis of the corrosion products by means of X-ray diffraction. The corrosion products which were observed in their studies and the assigned peaks are specified in Table 2.3.

The main Raman peaks of ZnO can be assigned to five modes: 100 cm⁻¹ (E₂), 330 cm⁻¹ (multiphonon), 375 cm⁻¹ (A₁ transverse), 440 cm⁻¹ (E₂) and a broad band at 540–580 cm⁻¹ (multiphonon) [79]. In the case of a higher crystallinity grade of ZnO, the peak intensity of 440 cm⁻¹ was higher in comparison to a poorly crystallized ZnO and the 560 cm⁻¹ peak was decreasing with poorer crystallinity [21; 79; 80].

Amorphous ZnOH₂ and α -ZnOH₂, which are unstable, were not observed by Bernard [21], although Feitknecht et al [74–76] proposed the formation during the first steps of precipitation. The β -, γ - and ϵ -ZnOH₂ were found as corrosion products by Bernard et al [21]. The main peaks were the lattice vibrations which are assigned in the region below 200 cm⁻¹, the ν -Zn-O in the region of 300–500 cm⁻¹ and the OH vibration in the range of 3100 – 3400 cm⁻¹. The exact peak assignments are listed in Table 2.3 and depending on the type of ZnOH₂ the characteristic peaks show slight shifts.

Table 2.3: Peak position and assignment to corrosion products observed during in-situ corrosion by Raman spectroscopy.

Corrosion products	Raman peaks
amorphous, native ZnO layer	broad band: 300–600 cm^{-1} , max located around 560 cm^{-1} [21; 78]
ZnO	330 cm^{-1} , 440 cm^{-1} , 570 cm^{-1} , 1070 cm^{-1} , 1140 cm^{-1} [21; 78]
ϵ -ZnOH ₂	130 cm^{-1} , 150 cm^{-1} , 210 cm^{-1} , 250 cm^{-1} , 370 cm^{-1} , 380 cm^{-1} , 480 cm^{-1} , 720 cm^{-1} , 760 cm^{-1} , 1030 cm^{-1} , 1050 cm^{-1} , 1080 cm^{-1} , 3190 cm^{-1} , 3260 cm^{-1} [21; 78]
γ -ZnOH ₂	130 cm^{-1} , 180 cm^{-1} , 360 cm^{-1} , 400 cm^{-1} , 440 cm^{-1} , 700 cm^{-1} , 830 cm^{-1} , 1070 cm^{-1} , 3160 cm^{-1} , 3250 cm^{-1} [21; 78]
β -ZnOH ₂	170 cm^{-1} , 210 cm^{-1} , 250 cm^{-1} , 300 cm^{-1} , 380 cm^{-1} , 420 cm^{-1} , 740 cm^{-1} , 800 cm^{-1} , 1030 cm^{-1} , 1080 cm^{-1} , 3100 cm^{-1} , 3150 cm^{-1} , 3250 cm^{-1} , 3340 cm^{-1} [21; 78]
4ZnOH ₂ ZnCl ₂	210 cm^{-1} , 260 cm^{-1} , 390 cm^{-1} , 730 cm^{-1} , 910 cm^{-1} , 1030 cm^{-1} , 3450 cm^{-1} , 3480 cm^{-1} , 3580 cm^{-1} [21; 78]
ZnOH ₄ ²⁻	465 cm^{-1} [77]
ZnCl ₂	250 cm^{-1} [21; 78]
ZnCO ₃	740 cm^{-1} , 1060 cm^{-1} , 1370 cm^{-1} , 1540 cm^{-1} [21; 78]

Zinc hydroxychloride shows a characteristic Raman spectrum and two strong peaks are observed in the lower wavenumber region at 260 cm^{-1} , assigned to a Zn–Cl bond and 390 cm^{-1} , attributed to a Zn–O vibration. Additionally, zinc hydroxychloride is characterized by two strong OH fundamental stretching bands at 3450 and 3480 cm^{-1} .

In strongly alkaline ZnO solutions as predominant species Zn(OH)₄²⁻ ions were identified at 465 cm^{-1} [77; 81–84]. Four vibrations were assigned to ZnCO₃ vibration modes ν_1 at 1060 cm^{-1} , ν_4 at 740 cm^{-1} and ν_3 at 1540/1370 cm^{-1} .

2.2 Molecular adhesion on aluminum and zinc oxides

The corrosion resistance and the adhesion of organic coatings on oxide covered metal alloy surfaces is of high importance for the integrity of the composite system and is mainly determined by the alloy composition, the surface chemistry of the alloy as well as by the

composition of the organic coating and its adhesion to the alloy surface. Monomolecular layers have been investigated as new advanced interfacial layers for polymer-coated aluminum and zinc alloys [9; 11]. The bond between the coating and the oxide covered metal substrate has to be strong enough to withstand mechanical stress within the composite and must be inert to any electrochemical or purely chemical attack [9].

2.2.1 Adsorption of monolayers

Long chain alkylphosphonic acids have been shown to adsorb and self-organize on a number of oxides such as silicon oxide and mica, as well as oxide covered metals such as tantalum, aluminum, silicon, zinc, magnesium, stainless steel [85–98]. Organic acids are mostly deposited from a dilute organic or aqueous solution [99–101]. At the beginning the sample is covered by solvent molecules and a competitive adsorption takes place. After an island like growth [102], the SAM adsorption continues until all solvent molecules are replaced by SAM molecules. The adsorption of a molecule is based on the interaction of the head group with the surface which is in many cases a kind of acid–base interaction. For example the principles of the binding of SAMs on the oxyhydroxide surface of aluminum were investigated by Allara et al. [103] and more recently by Maege et al. [8]. The driving force of the adsorption is the formation of a surface salt [8] and leads to a bidental bonding structure [8; 104].

The density of the monolayer and its ordering mainly depends on the intermolecular interactions of the tail structure [105]. Other important parameters for the formation are the head group functionality and the surface chemistry. It is well known that organophosphonic acids interact strongly with hydroxyl groups on various surfaces via acid–base interaction or coordinative bond formation [8; 12; 106]. Moreover, recent studies have shown that a high density of surface hydroxyl groups promotes the adsorption of organic acids, which leads to an improvement of the observed adhesion [10; 107; 108].

Giza et al. [10] have demonstrated that an oxygen plasma pre-treatment of the oxyhydroxide surface of aluminum accelerates the adsorption kinetic of ODPA. Mainly responsible for the ordering process is the tail structure, especially the length of the alkyl chain. The influence of chain length during the self-assembling process of different

organophosphonic acids was analyzed by Allara et al. [103] and recently by Gawalt et al. [109; 110]. The intermolecular forces have shown to play a very important role in the formation of a densely packed monolayer. Long alkyl chains are known to interact via van der Waals interactions and result in the deposition of highly ordered films [103].

The position and intensity of CH₃ and CH₂ vibration modes can give insights in the orientation of the molecules against the sample surface normal. A geometrical estimation for the calculation of the azimuthal angle is [111; 112]:

$$\frac{I_{CH_2}}{I_{CH_3}} = \frac{2n \cos (90^\circ - \alpha)^2}{3 \cos (35^\circ - \alpha)^2} \quad (2-1)$$

where I is the intensity of the according CH valence vibration bands, n is the number of methylene groups in the alkyl chain and α is the angle between the alkyl chain axis and the surface normal. The main assumptions for this kind of calculation are an all-trans conformation of the alkyl chain and a smooth surface [112].

The stability of SAMs is of high interest for a successful surface functionalisation. According to Allara et al. [105], the SAM formation is driven by substrate/head group interactions, intermolecular interactions and terminal group/ambient interactions and is also crucial for the stability of a formed SAM.

A study by Thissen et al. [106] revealed the dependency of SAM stability on the crystal orientation of the surface. ODPa monolayers were adsorbed on four different aluminum oxide surfaces and their stability in water was studied. The bonding stability was discussed based on the interfacial bonding type, the adsorption free energies in competition with water and involved adsorption geometries [106]. The poor stability on single crystalline Al₂O₃(001) surfaces has indicated an extremely important role of the local atomic structure of the aluminum oxide surface in the formation of stable organophosphonic acid films in competition to water [106].

Especially in case of weak surface/adsorbate interactions, the intermolecular interactions, primarily van der Waals interactions (enlarged with the chain length), are crucial for the stability against desorption during rinsing processes [63; 109]. Quinones et al. [109] reported that as the chain length of organophosphonic acids adsorbed on a NiTi surface decrease, different deposition conditions such as an increase in concentration and temperature were

necessary to promote film formation [109]. Furthermore, the stability of organophosphonic acid SAMs on NiTi as a function of the chain length was studied by Maxisch et al. [63]. The terminal/ambient interactions were controlled by the chemistry of the tail end. The presence of a CH₃ group leads to a hydrophobic behaviour [113] and reduce the solubility of the monomer in polar solvents.

Thissen et al [11] investigated in the formation and stability of octadecylphosphonic acid (ODPA) layers on Zn–Al alloy coatings. On Zn–Al alloys with higher Al–content ($\geq 5\%$) such as Zn–5%–Al and Zn–55%–Al, the formation of self–assembled monolayers (SAMs) of ODPA was observed. For small concentrations of Al (Zn–0.5%–Al) the Al–oxide containing passive film was not stable enough to prevent dissolution and precipitation of the phosphonate salt film. While the passive films of Zn–5%–Al and Zn–55%–Al were shown to consist of a continuous film of aluminum oxyhydroxides, the one on Zn–0.5%–Al was shown to be a mixed Zn, Al–oxyhydroxide. Furthermore the stability of the SAM in aqueous solutions was studied by means of contact angle measurements. The water contact angles measured on the alloys with SAM were stable over several immersion cycles but it was observed that the value of the contact angles depended on the respective surface structure and composition. A lower contact angle was observed for the Zn–5%–Al alloy in comparison to the Zn–55%–Al. They assumed that the surface of the Zn–5%–Al was not completely covered with the SAM and also that ODPA adsorbed strongly only in those areas where the Al–content is high.

Bi–functional organophosphonates are promising candidates for the molecular engineering of polymer/oxide/metal bonding. For adhesive promotion, functional end groups like COOH, OH or NH₂ groups can be used [9; 114–116]. The phosphonic acid group chemically adsorbs on the oxide–covered metal, whereas second functionality e.g. amino group is able to form covalent bonds to an organic coating or an adhesive. In previous section it was mentioned that, surface hydroxyl groups promote the adsorption of organophosphonic acid group and the adhesion of the phosphonate group is based on acid–base interactions [106]. The driving force is the formation of a surface salt as already described for long–chain carboxylic acids by Allara and Nuzzo [103] and recently by Terryn and co–workers [107; 108]. Adolphi et al. [95] showed that by the adsorption of organophosphonic acids on aluminum oxide as well as on tantalum oxide surfaces, bi–dentates are formed via the two hydroxyl functions of

the phosphonic acid, whereas the adsorption on titanium oxide surfaces led to the formation of tridentates. Pahnke and Rhe have demonstrated the possibility to promote the adhesion of organic layers to oxide covered Al surface via a photochemical reaction by the effective coupling of benzophenone containing organophosphonates [117].

Wapner et al. [9] investigated the adsorption of a short-chain aminopropylphosphonic acid (APPA) as adhesion promoting monomolecular layer at aluminum/polymer interfaces. As head group, an amine function similar to the functional group of the adhesive binder was chosen to allow crosslinking between the adhesion promoter and the adhesive. Additionally, a single step application of the APPA by mixing it as an additive to the adhesive formulation was studied. The surface characterization showed that an adsorbed APPA layer was formed on the aluminum oxyhydroxide surface via acid-base interactions in a bi-dentate conformation. It was observed that an enrichment of the adhesion promoter at the substrate surface could be achieved, which also influenced the crack growth along the interface. Additionally, it was shown that the interfacial enrichment of the adhesion promoter reduced the rate of the filiform corrosion with a performance similar to the two-step route via adsorbing the aminophosphonic acid from an aqueous solution prior to the coating with the adhesive.

2.2.2 Understanding of interfacial bond formation

The adsorption of alkyl-phosphonic on aluminum surfaces is an acid-base reaction. The driving force is the formation of a surface salt [8] and this fact is well known from the spontaneous adsorption of long-chain n-alkanoic acids [103]. Gawalt et al [88; 110] and Hoque [94; 104] investigated and developed a mono and bidentate binding model (Figure 2.4). Thissen et al [11] investigated in the formation and stability of octadecylphosphonic acid (ODPA) layers on Zn-Al alloy coatings. On Zn-Al alloys with higher Al-content ($\geq 5\%$) such as Zn-5%-Al and Zn-55%-Al, the formation of self-assembled monolayers (SAMs) of ODPA was observed. For small concentrations of Al (Zn-0.5%-Al) the Al-oxide containing passive film was not stable enough to prevent dissolution and precipitation of the phosphonate salt film. While the passive films of Zn-5%-Al and Zn- 55%-Al were shown to

consist of a continuous film of aluminum oxyhydroxides, the one on Zn–0.5%–Al was shown to be a mixed Zn, Al–oxyhydroxide.

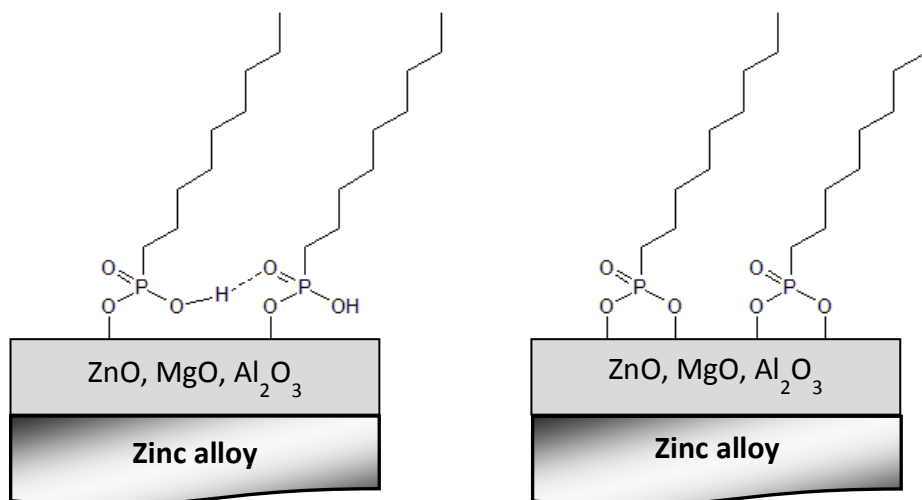


Figure 2.4: Schematic of mono- and bi-dentate binding model developed in the literature [8; 104; 110].

Giza et al. [10] have demonstrated that an oxygen plasma pre-treatment of the oxyhydroxide surface of aluminum accelerates the adsorption kinetic of ODPA. Mainly responsible for the ordering process is the tail structure, especially the length of the alkyl chain. The influence of chain length during the self-assembling process of different organophosphonic acids was analyzed by Allara et al. [103] and recently by Gawalt et al. [109; 110]. The intermolecular forces have shown to play a very important role in the formation of a densely packed monolayer. Long alkyl chains are known to interact via van der Waals interactions and result in the deposition of highly ordered films [103].

2.3 Fundamentals of adhesion and de-adhesion of polymers on oxide covered metals

The adhesion of polymer coatings on metal substrates is governed by the interatomic and intermolecular interaction at the interfaces. The understanding of the adhesion properties between the adhesive and the substrate is of crucial importance for the development of more versatile and efficient polymer/steel interfaces. Awaja [118] and Packham [119] described the fundamental theories of adhesion and reported that the pioneering work of

McBain and Hopkins [120] led to the development of the modern adsorption and mechanical theories of adhesion. In general terms, two main adhesion and de-adhesion mechanism can describe the interfacial phenomena: The first one is the adsorption of the polymer on the metal surface by physisorption or chemisorption and the second one is the mechanical interlocking of a polymer and a rough surface, where the increased adhesive strength is due to the enlarged surface area and subsequent increase molecular bonding interactions.

Two de-adhesion processes can take place in the polymer/metal interface. The first process is the interaction of water with the polymer which can lead to swelling or to degradation of the coating, followed by a loose of adhesion. This mechanism of wet de-adhesion was developed by Funke et al [121–123].

The second process is the so called corrosive de-adhesion which takes place in presence of an aggressive corrosive environment due to delamination processes [124–132]. More details about the corrosive de adhesion will be given in the next chapter.

2.3.1 Wet de-adhesion

The adsorption of water in a polymer coating is always given [113; 133–145]. Defect such as sites of fracture or hairline cracks, normally the case of altered systems, increase this effect due to the building of capillaries. The water diffusion in the polymer based coating change the mechanistic stability of these systems. The performance of the coatings are changed near the interface metal oxide/ polymer, stress inside the polymer coating, change of the chemical composition of the metal oxide layer, de-adhesion of the polymer due to change of the secondary interaction or thin water film between metal oxide/ polymer interface, increase of water amount at impurities which contains ions.

Comparison of the fracture picture in dry atmosphere and with high humidity shows de-adhesion at the metal oxide/polymer interface. In many publications a critical amount of the humidity was described. Lefebvre [145] has shown for example this critical value for epoxyamine adhesives. Özcan et al [146] studied the effect of ZnO nanorod film deposition on the adhesion between a zinc surface and a model epoxy-based adhesive and showed an improve in the adhesion in the presence of the ZnO nanorod film.

2.3.2 Corrosive de-adhesion of polymers on zinc substrates

The corrosion of bare zinc and zinc alloy coated steel surfaces in the presence of water and oxygen was described in Chapter 2.1. To prevent the direct contact of such surfaces with the corrosive environment, organic coatings are often applied as a corrosion protection measure [51; 124; 125; 127–132; 147–153].

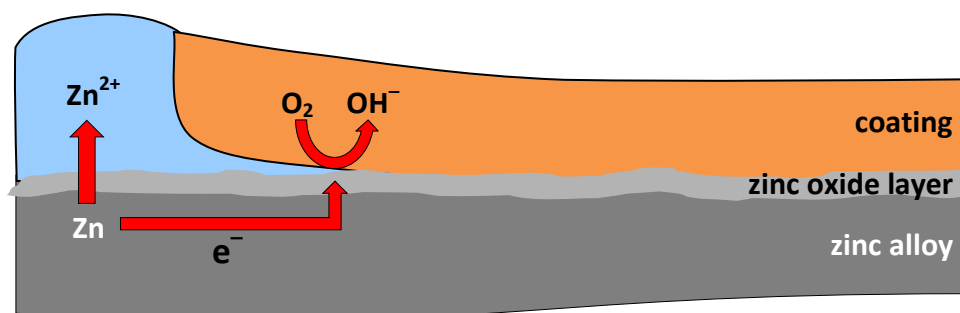


Figure 2.5: Schematic of the electrochemical reaction during the cathodic delamination process.

When a defect occurs in the organic coating an electrochemical cell forms in the presence of aerated electrolyte. In the defect the electrochemical reactions of zinc dissolution and oxygen reduction take place (Figure 2.5). The oxygen reduction takes place at the edge of the defect and could in principle also occur at the intact polymer/oxide/metal interface. But due to the diffuse electric double layer it is kinetically strongly inhibited.

The exposed polymer/metal interface gets attacked by the aggressive electrolyte and oxygen reduction increases at the reaction front at the polymer/steel interface. During oxygen reduction highly reactive oxygen species are formed which lead to degradation of the polymer/metal bonds and de-adhesion of the polymer. The hydroxide concentration at the polymer/metal interface increases as oxygen is reduced. The process of cathodic delamination is well described in the literature with results obtained by means of SKP, adhesion tests, XPS and ToF-SIMS surface analysis techniques [37–39; 51; 129; 130; 147; 150; 151; 154–158].

Posner et al. [51; 130; 151; 153; 158] studied in detail the cathodic delamination process on bare zinc and zinc covered with a polymer coating. Zinc oxides being not stable in the alkaline environment generated by the oxygen reduction were already discussed in Chapter 2.1. [77]. In the defect area the zinc dissolution takes place and the monitored potential is due to Zn/Zn^{2+} . In the transport area, the potential is found to be determined by $Zn/Zn(OH_4)^{2-}$. The combined oxygen reduction and zinc dissolution in the transport area was shown to buffer the pH and limit the degradation of the polymer/Zn interface. In some cases, wet de-adhesion mentioned in chapter 2.4 occurs at the same time as cathodic delamination. Nazarov et al. [15] described SKP studies of wet de-adhesion and explain that the potential determined by SKP is sensitive to the adhesion state of polymer and metallic surface.

2.4 Raman spectroscopic analysis of polymer/metal interface

Bernard et al. [20; 78] studied the underpaint corrosion of zinc-coated steel exposed to chloride containing solutions by means of Raman spectroscopy. Raman spectroscopy enables in-situ measurements in aqueous media and allows the analysis of surface areas of about $1 \mu\text{m}^2$ dimension. Bernard [20; 78] has performed their analysis through an organic coating, which was possible with the selection of a resin without fluorescent additives. Additionally, the influence of a conversion layer (chromatation or phosphatation) was investigated. Zinc hydroxychloride and zinc oxide/hydroxide were identified as corrosion products underneath the coating and this confirmed the hypothesis of large pH variations occurring under the paint in relation to local chloride concentration. Zinc hydroxychloride was claimed to be the result of anodic dissolution of zinc, whereas zinc oxide would form at cathodic sites after the formation of the amorphous hydroxide.

There were only small qualitative differences between the protections caused by the conversion treatments; they both delayed the blistering and the delamination. The corrosion mechanism occurring on zinc with the chromate layer remains rather similar to the mechanisms occurring on bare zinc. The chromatation layer, in spite of its porosity, disabled the passage of CO_2 which on the other hand favored the formation of hydroxychloride. Additionally, the chromatation treatment did increase the adhesion of the polymer coating,

which also suppressed the corrosion process. On the phosphated specimens, the growth of the cathodic corrosion products seemed to be hindered. The initial steps of the corrosion process could not be monitored because of an insufficient amount of corrosion products and the poor crystallinity of am-Zn(OH)₂.

More fundamental studies were performed by Santa et al [159]. A surface enhanced Raman spectroscopic setup was used for in-situ studies of the deterioration of thiazole/gold and thiazole/silver interfaces during interfacial ion transport processes induced by a KBr electrolyte. A self-assembled monolayer of 2-mercaptobenzothiazole (MBT) was adsorbed on surface enhanced Raman spectroscopy active gold and silver surfaces.

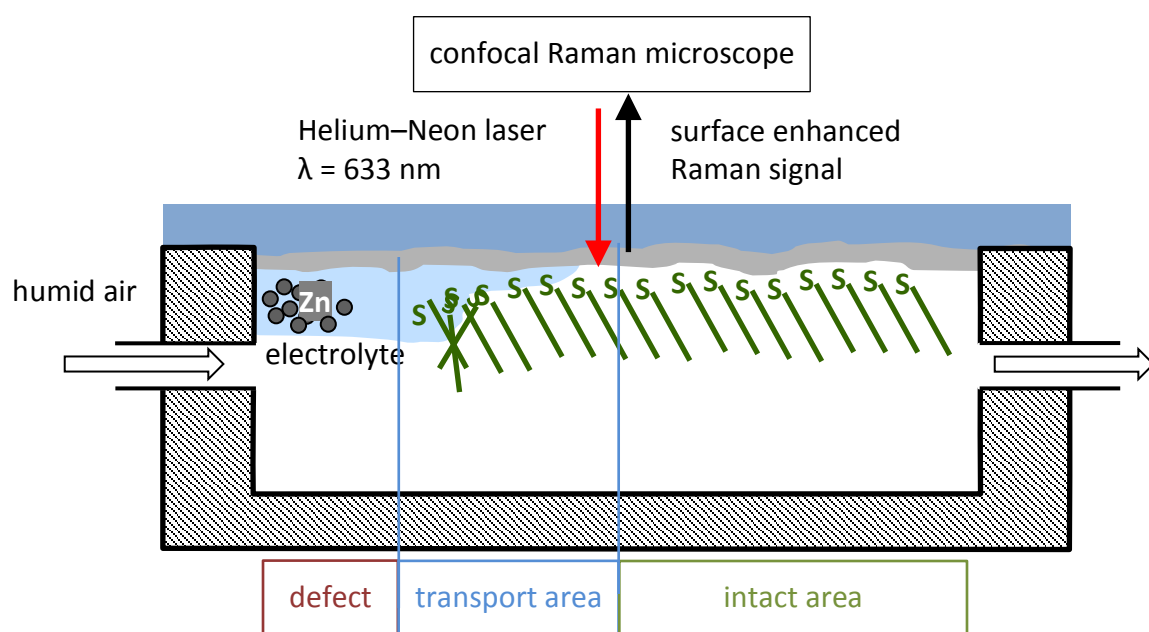


Figure 2.6: Scheme of the backside-SERS setup for the in-situ investigation of ion transport processes along the sample surface according to Reference [159].

Oxygen reduction induced ion transport and electrolyte spreading processes were initialized along the organic/substrate interface and the resulting changes of the structural monolayer constitution were monitored by Raman spectroscopy. SKP potential profiles indicated that liquid spreading on these samples proceeded similar to the mechanism of cathodic delamination. ToF-SIMS experiments proved a formation of hydroxide species in the region of electrolyte transport as well as the exclusion of bromide ions from this area. SKP potential profiles reflected the potassium distribution. The presence of MBT did not significantly inhibit the spreading process neither on gold nor on silver. SERS spectra showed that a

degradation of the MBT/metal interface proceeds in two steps. When it was initially affected by the electrolyte front, the adsorption geometry of MBT readjusts. During the second deterioration stage a distinct geometrical reorganisation and partial desorption of the monolayer occurred. The thiol head group was oxidized to sulphite and sulphate during ongoing interfacial oxygen reduction processes at alkaline pH. Even though SERS spectra were quite similar for MBT adsorption and monolayer degradation on Au and Ag, they nevertheless point at slightly different molecular geometries before and after interfacial electrolyte transport processes affected the monolayer.

3 Theoretical background of applied analytical techniques

The aim of this section is to give a brief introduction into the surface characterization techniques used in this study.

3.1 Spectroscopic techniques

The interactions of photons with material can cause absorption or scattering processes which can be used in a wide range of spectroscopic techniques. In the following sections Raman spectroscopy, Infrared spectroscopy and X-ray photoelectron spectroscopy are described.

3.1.1 Raman spectroscopy

Raman spectroscopy is performed by exposing the sample to monochromatic light and detecting the scattered light.

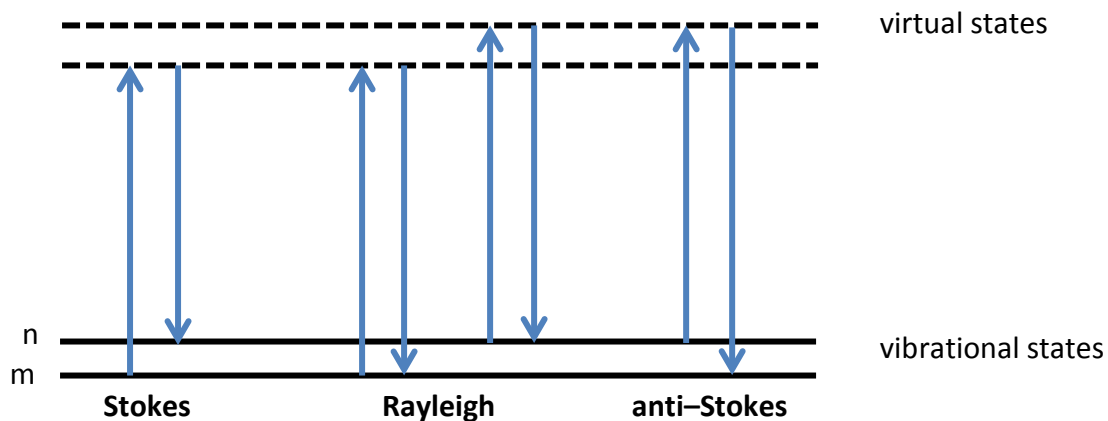


Figure 3.1: Schematic of the Rayleigh and Raman scattering process [160].

The dominant scattering process is the elastic scattering and is called Rayleigh scattering. The second scattering is the inelastic process where small shifts of the frequency occur and

is called Raman scattering. The Raman and Rayleigh scattering are illustrated in Figure 3.1 for one vibration.

The scattering is a result of the interaction of the light with the molecule and the followed distortion of the electron cloud. The amount of distortion of the cloud is depending on the ability of the electrons to get polarized. The interaction of the electromagnetic field of the incident electromagnetic wave E on the electron cloud occurs in all directions and can be described as dipole change μ (eq. 3.1) [161; 162].

$$\mu = \alpha E \quad (3-1)$$

The electric field of the incident electromagnetic wave with the frequency ν_0 causes a periodic change of the dipole moment and the molecule emits light with the same frequency (Rayleigh scattering). The time dependent induced dipole moment can be expressed as:

$$\mu = \alpha E_0 \sin 2\pi\nu_0 t \quad (3-2)$$

Further the polarisability based on the vibrational displacement can be written as:

$$\alpha = \alpha_0 + \frac{\partial \alpha}{\partial Q} Q_0 \cos(2\pi\nu_{vib} t) \quad (3-3)$$

Using common trigonometric relations equation 3.2 can be written as:

$$\mu = \alpha_0 E_0 \cos(2\pi\nu_0 t) + \frac{\partial \alpha}{\partial Q} \frac{Q_0 E_0}{2} [\cos(2\pi(\nu_0 - \nu_{vib})t) + \cos(2\pi(\nu_0 + \nu_{vib})t)] \quad (3-4)$$

At three distinct frequencies dipole moments are induced ν_0 , $(\nu_0 - \nu_{vib})$ and $(\nu_0 + \nu_{vib})$. The first frequency corresponds to the Rayleigh scattering and the shifted frequencies are corresponding to the Raman scattering.

3.1.2 Infrared spectroscopy

Fourier transform infrared spectroscopy (FTIR) provides information about the chemical bonding or molecular structure of materials. The infrared light interacts with the molecules and at characteristic frequencies at which the molecule is excited to vibration or rotation. Due to the initiation of the vibration a dipole moment change is occurring. The extent of the dipole moment change and the orientation of the dipole to the light vector assign the absorption intensity. Maximum absorption appears with maximum dipole change and if the dipole and the light vectors are parallel.

Absorption, reflection and scattering processes weaken the intensity of the interacting light and this loss of intensity $-dI$ can be described as:

$$-dI = k I c dx \quad (3-5)$$

with the intensity of the beam I , the absorption factor k and the length dx and the concentration c of the illuminated material [162].

Two vibration classes are defined. First is the valance vibration ν which leads to deformations along the bonding axis of the atoms. This vibration can be on the one hand symmetric and on the other hand asymmetric. The second class is the deformation vibration δ which can be separated in the rocking, twisting and wagging vibration. During the vibration the dipole moment of the molecule is changed inducing an alternating electric field which interacts with the electric field of the IR light. Absorption occurs, when the frequency of the irradiated light is similar to the natural frequency of the molecule vibration. The adsorption of a biatomic molecule can be calculated to:

$$\bar{\nu} = \frac{1}{2\pi\bar{c}} \sqrt{\frac{k}{\mu}} \quad (3-6)$$

with the wavenumber $\bar{\nu}$, the light speed \bar{c} , the force constant k and the reduced mass of the two atoms μ .

For the studies of metallic surfaces reflection spectroscopy is used. Infrared reflection absorption spectroscopy is influenced by the electronic structure of the metallic surface, the

angle of incidence (AOI) and the polarization of the incoming light. Based on the principles of electrostatic, the electrical field of a metallic surface is homogenous over the whole surface and the electric field vector is perpendicular to the surface [163]. The polarization state of the incoming IR-light can be parallel (p-) or perpendicular (s-) to the plane of incidence (Figure 3.2).

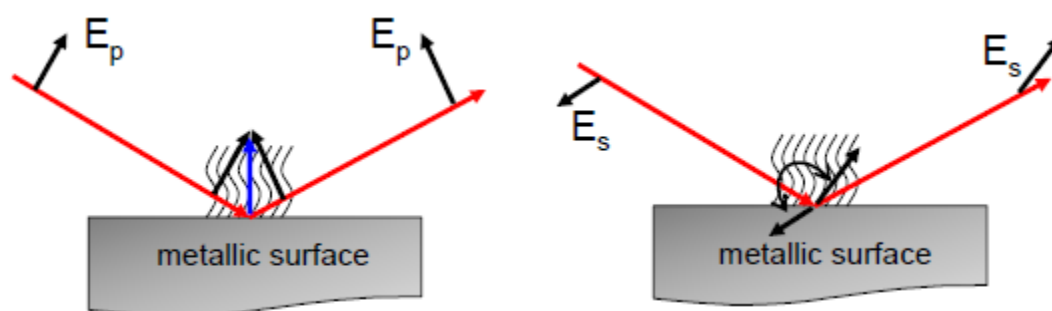


Figure 3.2: Schematic drawing of IRRA spectroscopy as a function of the polarization state taken from Reference [164].

Depending on the AOI and polarization state, the IR light can interact with this electric field vector (Figure 3.3).

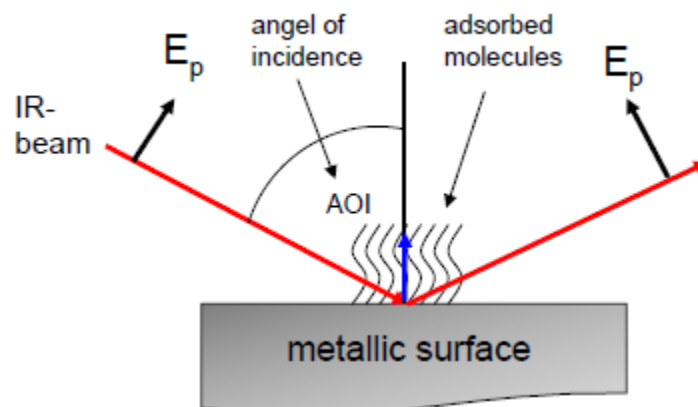


Figure 3.3: Schematic of IRRA spectroscopy taken from Reference [164].

In the case of p-polarization, the electric field vector of the light and the surface are directed in the same plane. The directions of the vectors approach with higher AOI and the IR light is enhanced. This is known as surface enhancement and can increase the surfaces sensitive by

a factor up to 25 [165]. The correlation between the reflection and the AOI of p-polarized light is shown in Figure 3.4.

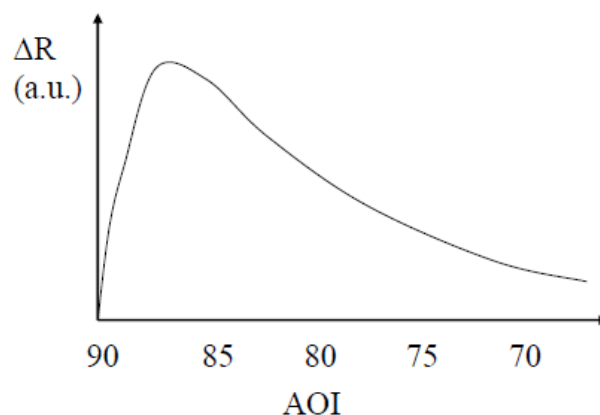


Figure 3.4: Reflection curve of p-polarized light as a function of the AOI taken from Reference [164].

This enhancement effect is only effective for p-polarized light. In the case of s-polarization, a phase shift of 180° is induced so that a standing wave is formed with a junction located directly at the surface and no surface information is collected [166]. For IRRA spectroscopy often p-polarized light is used due to this effect.

In contrast to IRRAS, with PM-IRRAS p- and s-polarized light are measured simultaneously and offers the possibility to obtain a differential reflectance spectrum of the surface and adsorbed layers without reference spectra [129–130]. Additional advantages of this technique are the elimination of signals from atmospheric water vapor and carbon dioxide. Further details concerning IR spectroscopy can be found in the common literature [161; 162].

3.1.3 X-ray photoelectron spectroscopy (XPS)

X-ray photoelectron spectroscopy is a surface chemical analysis technique with high surface sensitivity and a depth of information of around 5 nm. It gives qualitative and quantitative information about the sample surface. X-rays are focused at the sample surface, absorbed and lead to emission of electrons [167; 168]. The kinetic energy E_{kin} of the emitted electrons can be expressed as:

$$E_{kin} = h\nu - E_{bind} - \Phi_{sample} \quad (3-7)$$

and is characteristic for elements their chemical state with E_{bind} as binding energy of the electron and Φ_{sample} as electron work function of the sample.

The binding energy is evaluated using the kinetic energy measured by the detector which is conductively coupled to the sample. The binding energy is described by the following equation:

$$E_{bind} = h\nu - E_{kin(Detector)} - \Phi_{Detector} \quad (3-8)$$

with kinetic energy $E_{kin(Detector)}$ measured by the detector and the electron work function of the detector $\Phi_{Detector}$. In a simplified form, the intensity (I) of a photoelectron peak from a homogenous solid is expressed by:

$$I = J\rho\sigma K\lambda \quad (3-9)$$

With photon flux J , the concentration of the atom or ion in the solid ρ , cross section for photoelectron production (specific for element and energy being considered) σ , a term which includes all of the instrumental factors K and the electron attenuation length λ [167]. After correction of the detected intensities with sensitivity factors F which includes the terms σ , K and λ as well as additional features of the photoelectron spectrum such as characteristic loss features, a quantitative analysis can be performed. The surface composition calculated by this method assumes that the specimen is homogenous distributed in the sample volume queried by XPS. This is rarely the case, but for a comparison of similar specimens this method is still valuable. For a more precise analysis angle dependent XPS could be applied to ensure the lateral homogeneity and to elucidate the hierarchy of overlayers present [167].

3.2 Electrochemical techniques

Redox reactions, which takes place in a solution at the interface of an electrode (a metal or a semiconductor) and an electrolyte (ionic conductor), can be analyzed with a wide range of electrochemical techniques. In the following sections scanning Kelvin probe, cyclic voltammetry and scanning Kelvin probe force microscopy are described.

3.2.1 Scanning Kelvin probe (SKP)

The Kelvin probe is a non-contact and non-destructive technique which measures the work function difference $\Delta\Phi_S^{Ref}$ of a needle (reference) and the substrate surface [37; 154; 169].

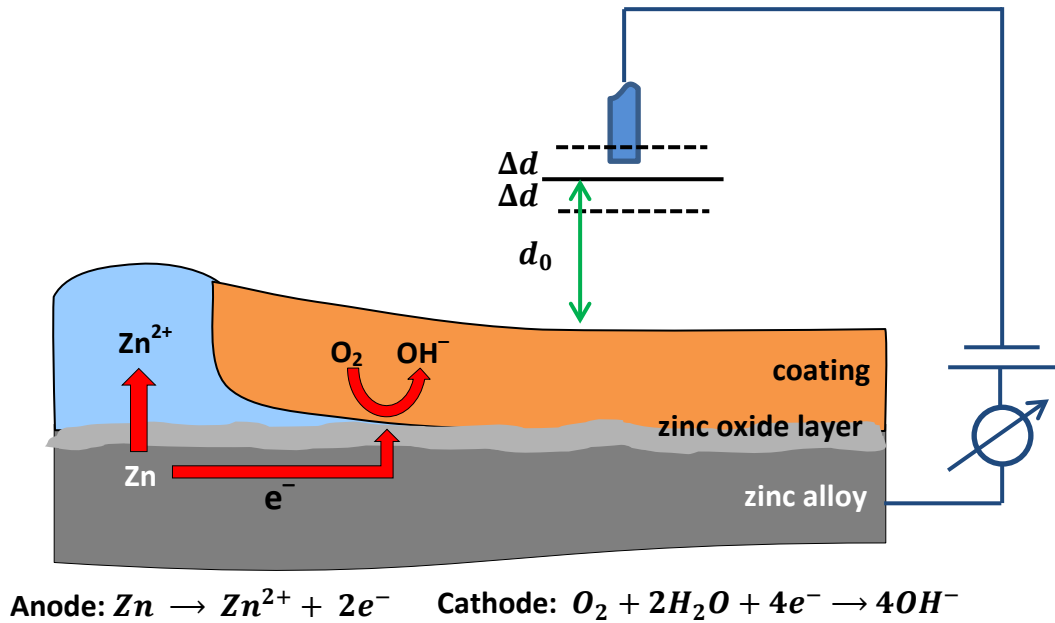


Figure 3.5: Schematic of the Kelvin probe setup [152; 170].

A capacitor is formed between the Kelvin Probe and the substrate surface and due to the vibration of the needle the capacitance is varied. A schematic of the setup is shown in Figure 3.2.

The resulting capacitance can be calculated by the following equation:

$$C = \frac{Q}{U} = \varepsilon\varepsilon_0 \frac{A}{d_0 + \Delta d \sin \omega t} \quad (3-10)$$

with the dielectric constant and the permittivity of free space ε and ε_0 , the frontal tip area A , the distance d_0 between sample surface and tip and the tip vibration frequency ω . The detected interface potential can be correlated to standard hydrogen electrode after calibration to a known potential system like $Cu/CuSO_4$ [148; 171].

This setup allows the detection of potential changes of the surface chemistry due to modification of the surface composition or due to electrochemical reactions.

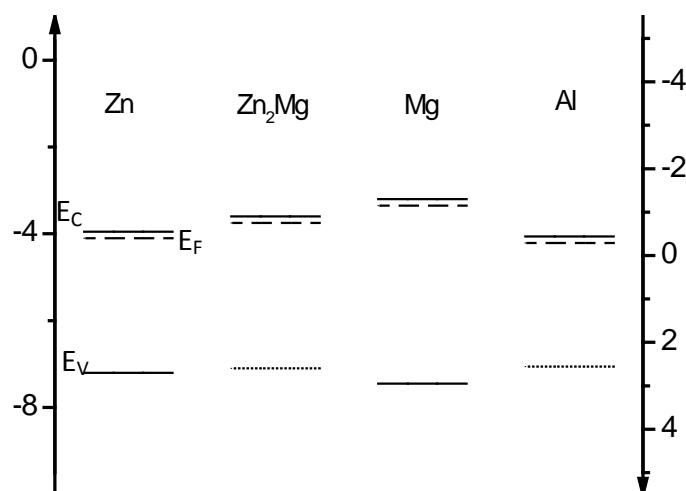


Figure 3.6: Scheme of the bulk band structure of the passive oxides of zinc, Zn_2Mg , magnesium and aluminum. Valence band position E_V and conduction band position E_C are indicated with a solid line. Fermi levels E_F are indicated with dotted line. The positions of the bands in the electronic structure were taken from reference [60]. For the positions of the conduction band edge of aluminum, Kelvin Probe measurements of Özkanat et al. [172] were used and the band gaps of the passive layer were taken from Reference [173], thus providing the position of the valence band. The valence band position of Zn_2Mg and aluminum is indicated by a dotted line.

According to Hausbrand et al [60] the potential of passivated zinc, Zn_2Mg and magnesium were measured and the band structure of this specimen were sketched. In Figure 3.6 the band structure for these metal/metal oxide and for aluminum is shown. Additionally Hausbrand et al. [60] correlated the band gap of the passive films with the electrode potential and was found to be linear for n-type semiconductors. The passive layers in dry ambient atmosphere might be considered as semiconductors covered with chemisorbed oxygen complexes [60].

3.2.2 Cyclic voltammetry (CV)

Cyclic voltammetry (CV) can be described as a potentiodynamic electrochemical measurement as described in detail in [174]. The working electrode potential is ramped linearly versus time and the resulting current density is measured. This ramping is known as the experiment's scan rate and is shown in Figure 3.7.

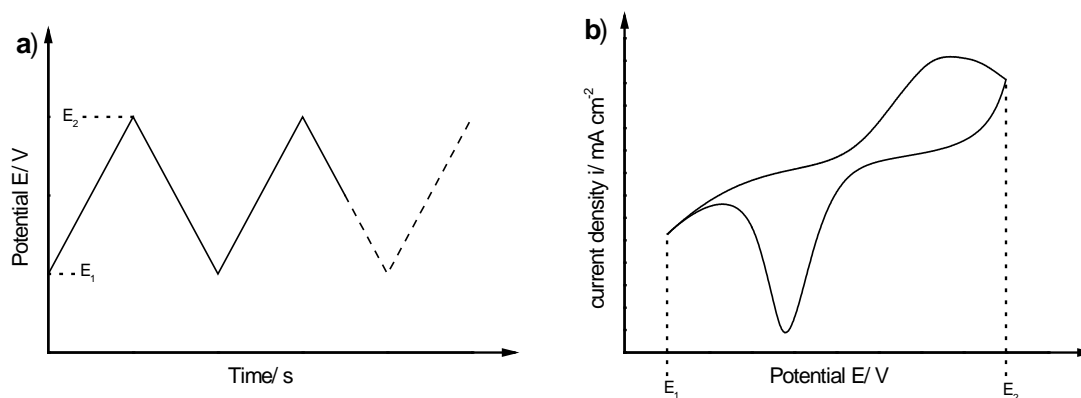


Figure 3.7: Potential–time curve at the working electrode in the cyclic voltammetry [174].

Positive and negative turn–round potential, E_1 and E_2 are usually chosen in aqueous electrolyte to lie between the hydrogen and oxygen evolution potential. If a material can be reduced by the electrolyte, than the current density will increase as the ramped potential reaches the reduction potential of the material, but decreases as the concentration of the material is depleted close to the electrode surface. If the redox couple is reversible than the former reduced material can be reoxidized when the oxidation potential is reached. For ideal systems the current densities between the oxidation and reduction process are equal and the oxidation and reduction peaks in the voltage versus current density plot have a similar shape. The amount of charge which is transferred to the electrolyte when the material is reduced or oxidized is directly proportional to the surface area which is in contact with the electrolyte. If parts of the surface are covered with a barrier film which cannot be oxidized or reduced at potentials when the metal substrate can be oxidized or reduced, than the protected area can be directly calculated by the difference of the charge transfer on an unprotected and a partially protected surface [175; 176].

3.2.3 Scanning Kelvin probe force microscopy (SKPFM)

The scanning Kelvin force microscopy technique is similar to the scanning Kelvin probe technique but on a diminutive size. Also here the work function difference between a probe, in this case a cantilever and tip with conductive coating, and a substrate surface is measured.

In Figure 3.3 the principle of the measurement and the setup is shown. This technique is implemented in an Atomic Force Microscope which is described in detail in Chapter 3.3.2.

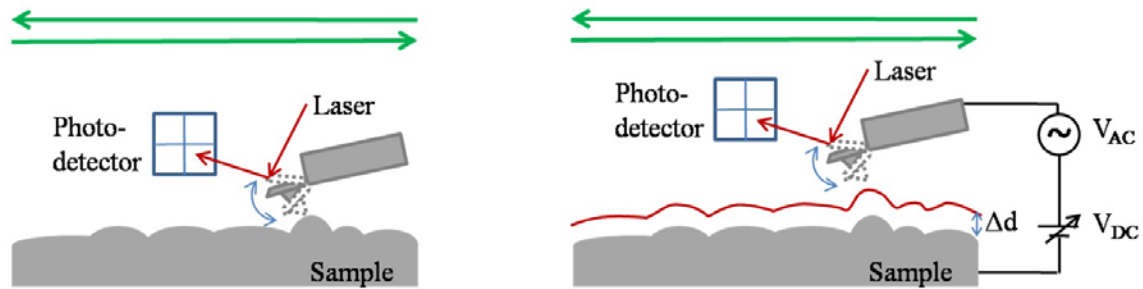


Figure 3.8: Schematic setup of scanning Kelvin probe force microscopy (SKPFM) [177].

The measurements are performed in the Dynamic-Contact (DC) mode. In this mode the cantilever is oscillating in its resonance frequency. When the cantilever is now moved towards the sample surface forces are acting with the cantilever which are due to the interaction of the cantilever and the sample surface. For the "lift mode" SKPFM measurement each line is scanned twice. The first scan records the topography profile. The second scan is performed with a certain distance (in the range of 50 nm) to the surface and to collect the potential information of the surface an AC voltage (range of 3V) is applied to the tip. Then the cantilever follows the pre-recorded topography profile.

The capacitor formed by tip/cantilever and sample stores a certain electric energy and can be described by [178]:

$$W_{cap} = \frac{1}{2}V^2C \quad (3-11)$$

with $V = \Delta\psi - U_{ac} + U_{ac} \sin \omega t$. The electric force is given by:

$$F_e = -\frac{dW_{cap}}{dz} = \frac{1}{2}V^2 \frac{dC}{dz} = \frac{1}{2}V^2C' \quad (3-12)$$

The total electric force can then be expressed by:

$$F_e = \frac{1}{2} \left\{ (V_{dc} - \Delta\psi_{sample}^{Ref})^2 + \frac{1}{2} V_{ac}^2 \right\} C' + C' (V_{dc} - \Delta\psi_{sample}^{Ref}) V_{ac} \sin \omega t + \frac{1}{4} C' V_{ac}^2 \cos \omega t \quad (3-13)$$

Hence, the force modulation at frequency ω becomes zero for $V_{dc} = \Delta\psi_{sample}^{Ref}$. During this scan, the magnitude of the oscillations at the stimulating frequency is nulled on a point-by-point basis during the lift mode rescan by applying a DC voltage to the tip which balances the Volta potential difference and thus the surface charge [178]. The magnitude of the required DC voltage directly yields the Volta potential difference [177].

3.3 Microscopic techniques

Optical and electron microscopy is widely used to characterize the morphology of materials. The interactions of electromagnetic radiation/electron beams with material can cause diffraction, reflection, or refraction and this scattered radiation or another signal can be collected in order to create an image. In the case of scanning probe microscopy, the interaction of a scanning probe with the surface of the object of interest. In the following sections scanning electron microscopy and atomic force microscopy are described.

3.3.1 Scanning electron microscopy (SEM)

The SEM allows a detailed surface analysis of condensed materials. Electrons are generated by a hot cathode or by Schottky field emission. They are accelerated up to 50 keV and then focused on the surface by electromagnetic lenses. Secondary (below 50 eV) and backscattered electrons (50 eV to acceleration voltage) result upon contact with the specimen. They are detected and used for imaging. Interaction area and depth depend on the acceleration voltage and the elemental composition of the sample material.

Secondary electrons are formed by inelastic interaction of primary electrons with surface atoms. Either a chamber detector or an in-lens detector can be used for their detection. Chamber detectors are mainly Everhart-Thornley detectors that use a grid with an applied voltage between -200 to $+200$ V. The electrons hit a scintillation counter and the generated

photons are amplified by a photomultiplier. High electron yields lead to lighter and lower electron yields to darker pixels in the image. In-lens detectors also collect the electrons by an applied voltage but the detection of the electrons happens by a semiconductor. When an electron hits the detector, it generates electron-hole pairs that lead to an electric signal. In-lens detectors allow much smaller working distances than chamber detectors and collect the electrons at the point of impact. This leads to higher resolution in contrast to the chamber detectors.

SEM does not give any chemical information about the substrate, but Auger electrons and X-rays are formed by the interaction of electrons with the sample. By means of electron dispersive X-ray analysis elemental composition of the substrate is evaluated in a depth of few micrometers [170; 179].

3.3.2 Atomic force microscopy (AFM)

Atomic force microscopy (AFM) is a scanning probe technique, where a cantilever with a sharp tip is used to scan the sample. The detection mechanism of AFM is based on the forces acting between the tip and the surface Figure 3.9. When the tip approaches the sample surface, the cantilever will be deflected due to these forces according to Hooke's law. Measurements can be performed in controlled gas atmospheres, in ultra-high vacuum but also in electrolytes and solvents. The mode of the detected forces depends on the measurement environment. In general information can be acquired on the capillary forces, chemical bonding, electrostatic forces, mechanical contact forces and van der Waals forces. There are multiple measurement modes available in commercial AFM systems. The most common one is known as the "Contact Mode", where the cantilever is approached and pressed onto the surface at a constant force and then scans the surface to gather topography information. The detector does not only collect the deviation of the signal in the z-direction but also records the deviations in x/y, depending on the slow scan direction. These deviations enable the collection of valuable lateral force signal and therefore facilitate the detection of chemically or mechanically inhomogeneous regions on the samples.

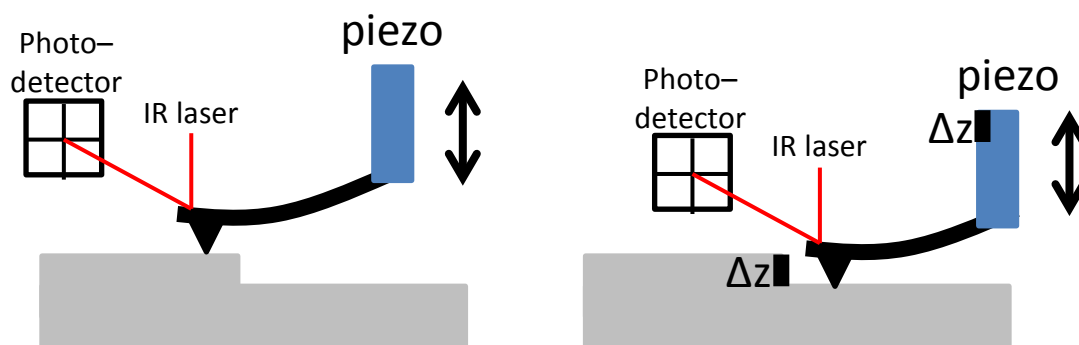


Figure 3.9: Schematic setup of atomic force microscopy in contact mode.

For the samples with sensitive nature, like thin films where contact mode imaging becomes destructive and where the water meniscus formation at the tip cannot be prevented "Dynamic-Contact (DC) Mode" was developed. In this method the cantilever is driven to oscillate up and down at near its resonance frequency. Due to the interaction of forces acting on the cantilever when the tip comes in the proximity of the surface, the amplitude of this oscillation decreases due to the forces acting between the tip and the surface. At all instances, an electronic servo uses the piezoelectric actuator to control the height of the cantilever above the sample. This servo continuously adjusts the height of the tip to keep the amplitude of the cantilever oscillation stable during the scanning process. The images produced by DC mode are based on the intermittent contacts of the tip with the sample surface.

At the same time the phase image which records the modulation of the phase of the oscillation carries information on the chemistry and adhesive properties of the surfaces. For many applications phase images produced during DC mode imaging can provide high contrast for heterogeneous samples with low topography contrast.

3.4 Contact angle measurement

Contact angle measurements are performed to know the ability of a liquid to cover a surface. The contact angle θ of a liquid droplet on the sample surface is a function of the surface tension of the solid/liquid interface and the surface tension of the solid surface. The

wettability can be quantified by the Young equation which establishes a correlation between the contact angle θ and the solid/gas interface tension γ_{SG} :

$$\gamma_{SG} = \gamma_{SL} - \gamma_{LG} \cos \theta \quad (3-14)$$

with the solid/liquid interface tension γ_{SL} and the liquid/gas interface tension γ_{LG} .

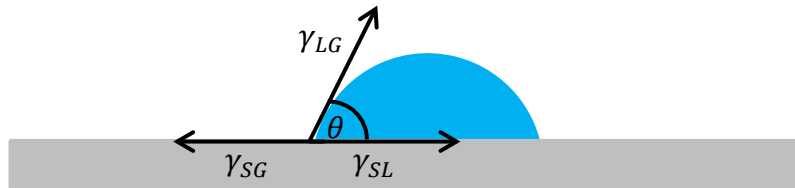


Figure 3.10: Contact angle between liquid drop and solid surface.

Different procedures are developed for the calculation of surface energies from contact angle measurements. Fowkes introduced an additive approach, describing the bulk phase as a sum of independent contributions from different types of intermolecular interactions. Owens and Wendt extended this approach to the interaction of polar liquids and surfaces [180]. They measured the contact angles of three different solvents – deionized water with pH = 6.8, ethylene glycol and diiodomethane – where the polar (γ_L^P) and dispersive (γ_L^D) components of the surface tension of are known. The surface energies of the observed system can be expressed by:

$$\gamma_L \cos(\theta + 1) = 2\sqrt{\gamma_S^D \gamma_L^D} + 2\sqrt{\gamma_S^P \gamma_L^P} \quad (3-15)$$

assuming that the total free energy at a surface can be considered as a sum of contributions.

4 In-situ corrosion analysis of zinc alloy coated steel

The initial corrosion of hot dipped galvanized steel in pH 3, 7 and 11 containing 0.05 M sodium chloride was investigated by means of Raman spectroscopy. To prevent pH changes of the electrolyte during the measurement due to oxygen reduction the experiments were performed under a high electrolyte flow. Additionally the microstructure of the zinc layer was analyzed by means of electron backscatter diffraction (EBSD) to investigate the influences of the microstructure on the corrosion process. Furthermore the surface morphology and bulk composition was characterized by scanning electron microscopy and energy dispersive X-ray spectroscopy, respectively. The electronic surface properties were measured with scanning Kelvin probe force microscopy (SKPFM). The Raman spectra showed different composition of the oxide layer after the exposure to the electrolyte dependent on the pH. In the case of pH 3 a slow dissolution of zinc was observed. In neutral pH the amount of oxide and hydroxide was on the grain increasing and at the grain boundary the amount stayed constant. At pH 11 the amount was slowly increasing at all points.

4.1 Experimental

4.1.1 Materials and sample preparation

If not indicated otherwise, all chemicals were of p.a. grade (pro analysis) and were used as supplied without any further purification. As substrates hot-dip galvanized steel sheets (Z) were used as samples of technical interest. The interstitial free Z steel (sheet thickness 0.85 mm) was supplied by voestalpine Stahl GmbH (Linz, Austria) in the non-skin passed state, i.e. without being temper rolled after application of the zinc coating. The thickness of the zinc coating (alloy composition: Zn + 0.05% Al) after hot dip galvanizing was 7.5 μm . Samples were cut from the supplied material in 10 by 10 mm² samples and cleaned in three different solvents in an ultra-sonic bath for 20 min to remove oils and surface contaminations. As solvents tetrahydrofuran (THF), iso-propanol and ethanol with analytical grade (Merck KGaA, Darmstadt, Germany) were used. After every solvent treatment the samples were dried under flow of dry air.

4.1.2 Surface Analysis

Prior to the in-situ corrosion test the surface morphology and chemistry was analyzed by means of microscopic and spectroscopic techniques. The morphology and the surface composition was verified by means of a SEM with a field emission gun (LEO 1550VP) combined with an energy-dispersive x-ray spectroscopy (EDX) unit (Oxford Instruments). The EDX measurements were performed at an accelerating voltage of 20 kV and a working distance of 8 mm, which results in a penetration depth of electrons higher than 1 μm .

Surface topography and electronic surface properties were investigated by means of SKPFM (MFP3D – Asylum Research, Santa Barbara, CA), equipped with an anti – vibration table and custom designed noise – insulation chamber. For the SKPFM measurements highly doped silicon cantilever were used (NSC15, doped, AIBS, MikroMasch, Tallinn, Estonia). The spring constant of each AFM cantilever was calibrated via thermal tune method. The principles of data collection for SKPFM measurements includes as a first step the gathering of topography information by means of a pair of trace and retrace scans. In the second step the selected potential is applied to the AFM-tip and the topographical information collected in the first step is used to track the surface potential information. The tip follows the topography of the measured line with a user defined distance from the surface. In all the SKPFM measurements in this paper the tip to surface distance and the tip voltage during the potential measurement were set to 50 nm and 3 V, respectively.

To analyze the microstructure of the electron backscatter diffraction (EBSD) measurements were carried out on the surface with an area of $300\mu\text{m}^2$ using a scanning electron microscope working at a nominal voltage of 20 kV.

4.1.3 In-situ Raman spectroscopy

The corrosion products were analyzed during the corrosion process by means of a confocal Raman microscope. The Raman spectra were obtained using a InVia Renishaw confocal Raman microprobe system (Renishaw plc, UK) equipped with an Leica DM 2500 M confocal microscope and an air cooled HeNe laser ($\lambda = 632.8 \text{ nm}$). Measurements were performed using a HCX APO L63x immersion objective for water with a numerical aperture of 0.9 and a

1800 grooves/mm diffraction grating. The laser power was set to 1.75 mW and an exposure time of 30 s. The in-situ Raman spectroscopic measurements were performed within a custom made cell with an electrolyte volume of 3 ml and a scheme of the setup is shown in Figure 4.1. The flow through cell is equipped with a three electrode setup to measure also the potential during the corrosion process. The samples were exposed to pH 3, 7 and 11 containing 0.05 M sodium chloride solution and time dependent Raman spectra were taken in intervals of 20 min.

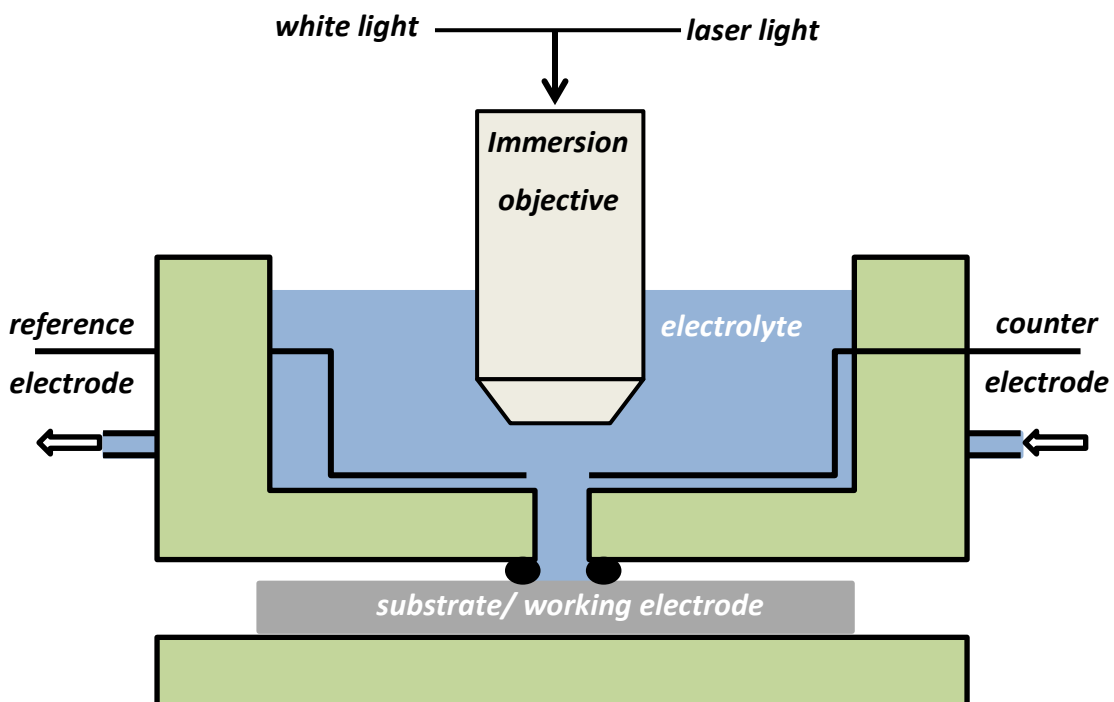


Figure 4.1: Scheme of the applied Raman spectroscopic setup for the in-situ investigation of corrosion processes.

Prior to the Raman measurement microscopic pictures were taken which allows us to set always certain points on the sample to be measured.

4.2 Surface morphology and microstructure

Due to the aluminum addition and iron dissolution in the galvanizing zinc bath the considered zinc coating is alloyed with a small amount of Al and Fe according to the solubility of these elements in liquid zinc [181–183]. After emersion from the bath, the zinc

layer is cooled by gas-wiping dies blowing air or nitrogen. Solidification of zinc grains has been shown to start at the steel/coating interface [181]. The delivered samples were oiled to reduce the atmospheric corrosion process. Therefore the samples were solvent cleaned before performance of the measurement.

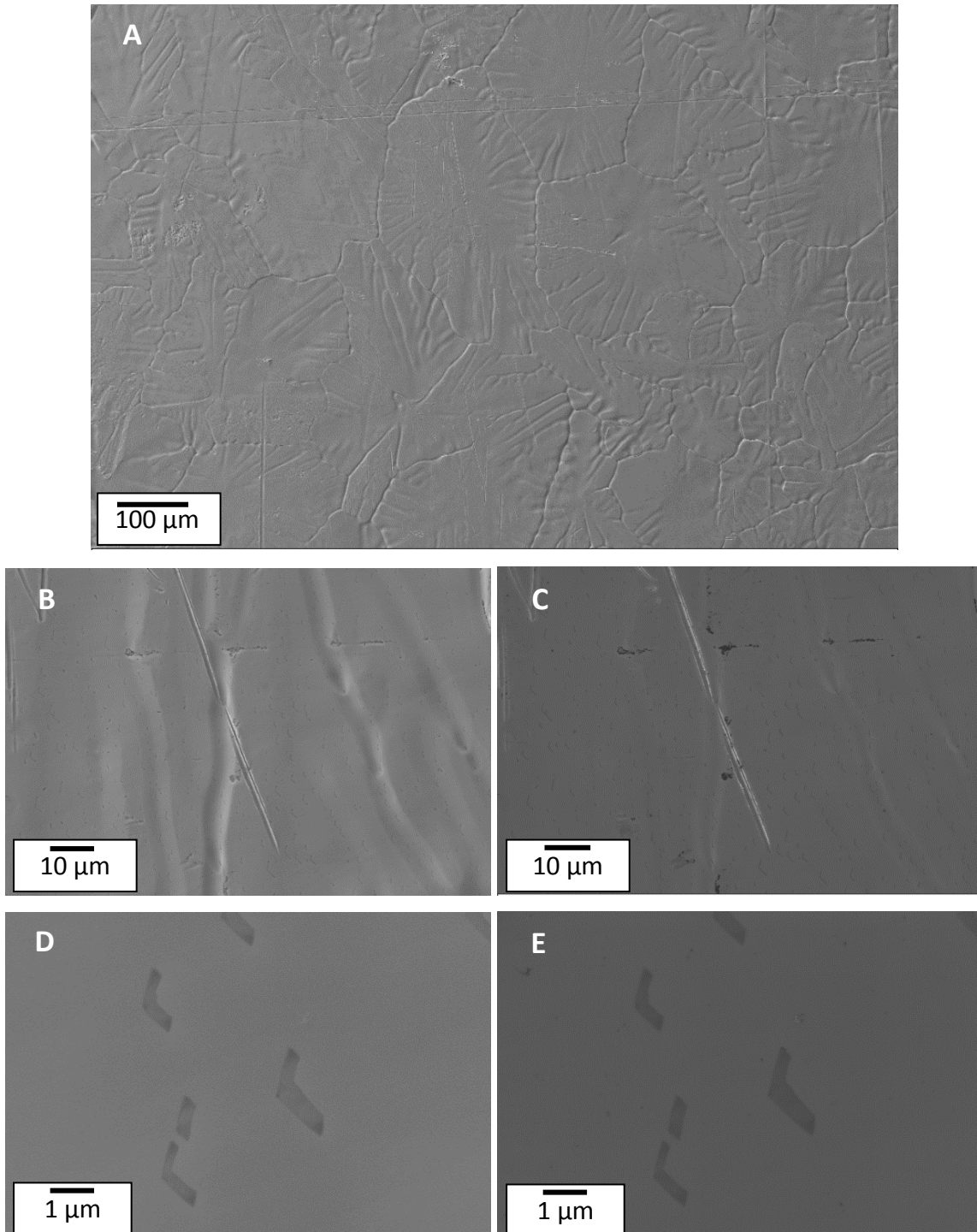


Figure 4.2: SEM analysis of hot-dipped galvanized steel surface, SEM parameters: WD = 4.9 mm and EHT = 20.0 kV, (A) Mag = 100x, Detector = SE 2, (B, C) Mag = 1kx and (D, E) Mag = 10kx, (A, C) Detector = SE 2 and (C, E) InLens.

Figure 4.2 shows the morphology of the solidified coating. Zinc grains are dendritic and the in-plane grain size ranges from $200 \mu\text{m}^2$ to $600 \mu\text{m}^2$. Magnified images are shown in Figure 4.2B, C, D and E of the Z. The pictures on the left side were detected with the SE2 detector which detect the topography of the sample. The images on the right side were taken with the InLens detector and this detector is more sensitive to material differences.

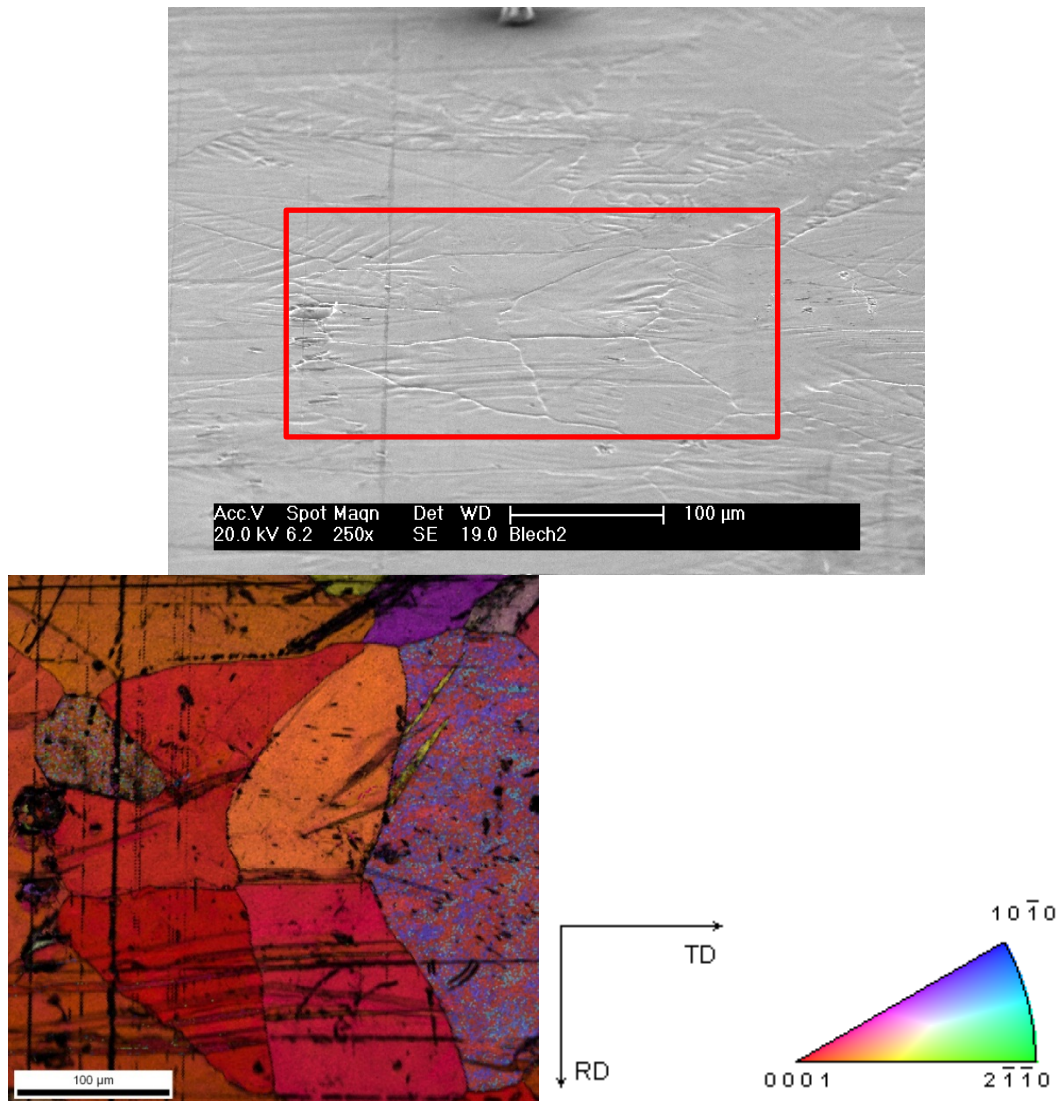


Figure 4.3: SEM image 70° tilted and EBSD grain orientation mapping, red frame area of EBSD image and the inverse pole figure.

The topography of the dents in Figure 4.2B is clearly demonstrated. However this dents show no significant chemical difference which is shown in Figure 4.2C. The surface looks smooth. A homogenous distribution of inclusions was observed on several grains. These inclusions were further magnified and the images are shown in Figure 4.2D and E. The

bommerang – shaped inclusions are smooth included in the surface layer (Figure 4.2D and E).

The solidification of Zn–Al coatings is strongly influenced by the fact that the melt is constrained between the steel substrate (in fact the intermetallic formed at the steel–coating interface) and the free surface is in contact with air. These two interfaces offer a high density. The coatings are strongly anisotropic, with most zinc grains having their c–axis normal to the sheet plane [181; 182]. This is due to the hot–dip solidification process. In Figure 4.3 the SEM image and the corresponding EBSD map is shown. The red frame marks the area where the EBSD map was taken. The EBSD map shows the crystalline structure of the bulk coating. The EBSD grain orientation is strongly determined by 0001 which was also observed by Boehm–Courjault et al [181].

4.3 Bulk composition of the alloy

The composition of the employed alloy was studied by means of energy dispersive X–ray spectroscopy. The SEM picture is shown in Figure 4.4 with the complementary EDX analysis of the local aluminum, carbon, zinc and oxygen content. In the SEM picture inclusions on the grains are seen which have different shapes and incidence. On two grains the inclusion are point–shaped and on the third grain the inclusions are dash–shaped. Additionally surface defects were observed. The EDX maps present the concentration of the element in this area. No and very low concentrations are shown in white. At the grain boundaries a higher content of aluminum and oxygen were observed. Additionally, the surface defects show higher oxygen content. The carbon and zinc contents are homogenous distributed on the surface. However, the composition of the inclusions on the grains could not be resolved with this magnification.

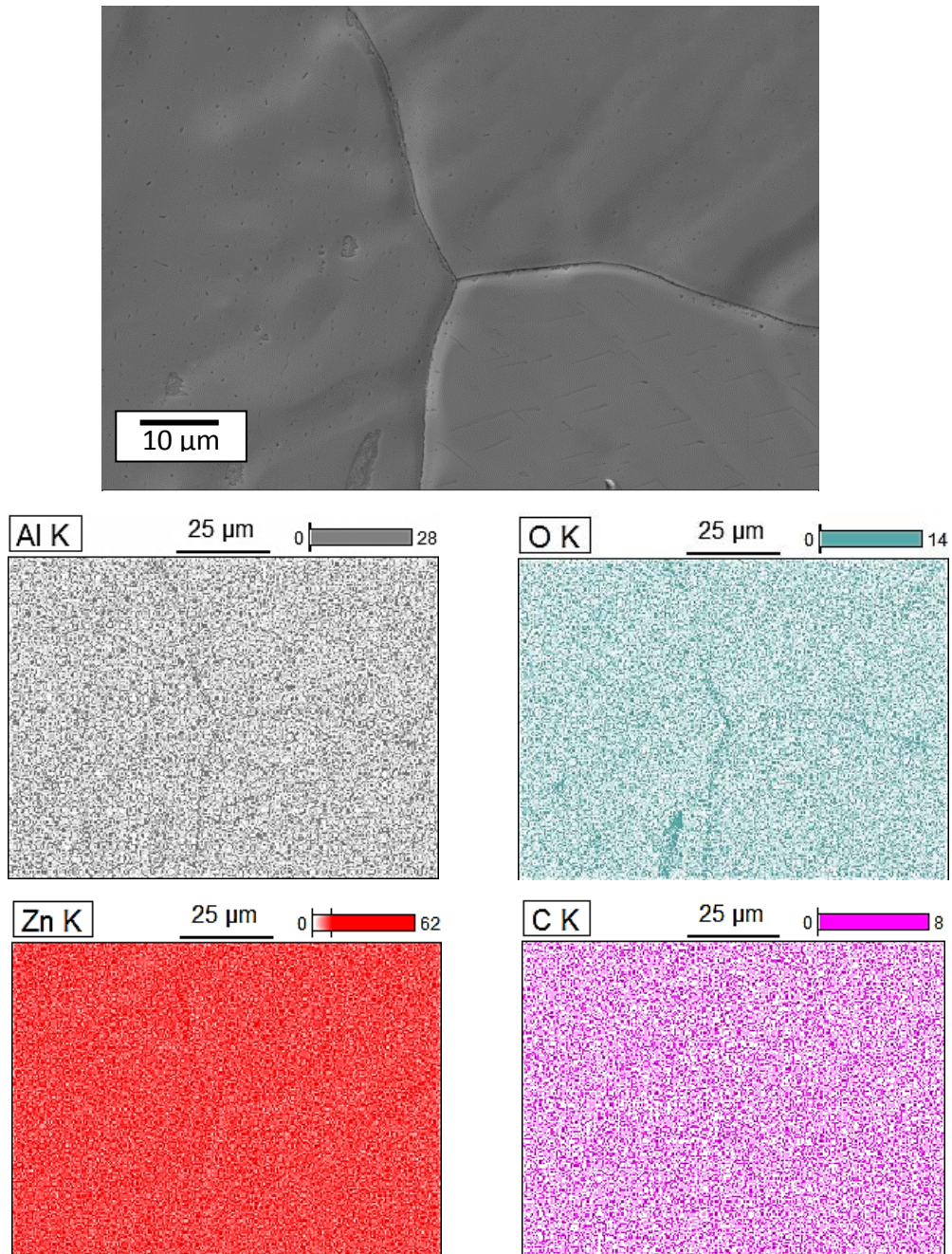


Figure 4.4: SEM analysis (top) and EDX mappings of local Al, O, Zn and C content of hot-dipped galvanized steel surface. SEM parameters: Mag = 1kx, WD = 4.8 mm, Detector = SE 2, EHT = 20.0 kV.

The picture was further magnified to have a closer view on the inclusions (Figure 4.5). Several EDX points were measured and are highlighted in the SEM picture. In Table 4.1 the composition of the certain points are listed.

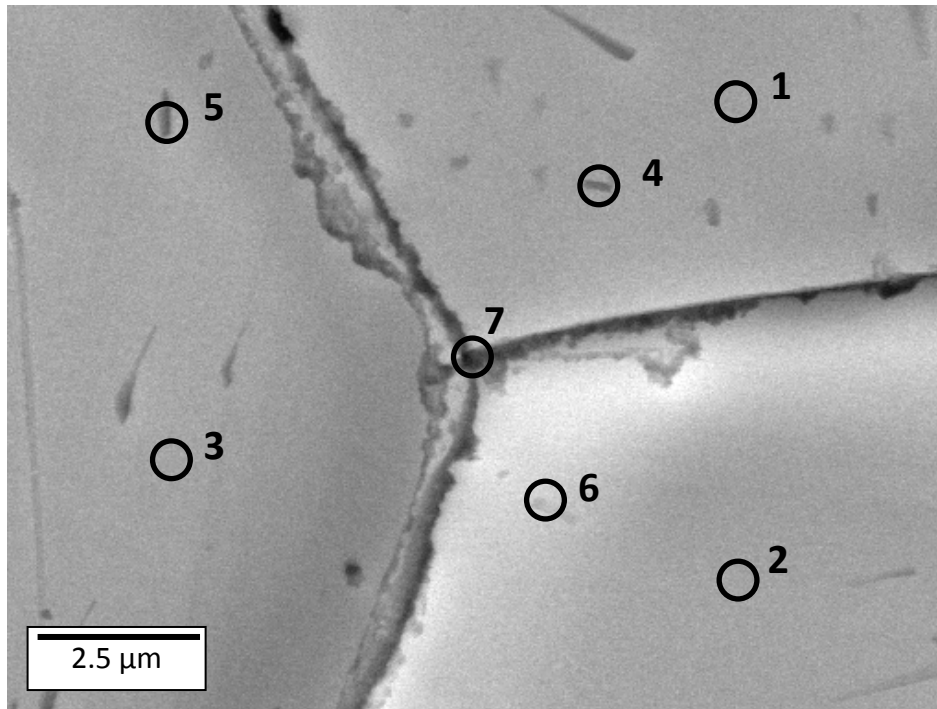


Figure 4.5: SEM analysis and EDX analysis of hot-dipped galvanized steel surface, SEM parameters: Mag = 8kx, WD = 4.8 mm, Detector = SE 2, EHT = 20.0 kV.

The points 1 to 3 were set as reference next to the inclusions which were measured at points 4 to 6. Point 7 was set in the middle of the grain boundary where the three grains hit each other.

Table 4.1: Composition of certain points measured with EDX and assigned in Figure 4.5.

	C-K	O-K	Al-K	Fe-K	Zn-K
pt 1	2.02	0.23	0.53	0.93	96.29
pt 2	2.04	0.26	0.48	1.07	96.16
pt 3	1.97	0.24	0.47	0.97	96.35
pt 4	1.59	0.14	7.98	0.95	89.34
pt 5	1.92	0.40	3.88	1.03	96.76
pt 6	2.44	0.27	2.96	0.91	93.42
pt 7	1.36	1.89	2.18	1.01	93.56

The highest amount in all points is the Zn amount which is always over 90%. The carbon amount is more or less constant and is ranging from 1.6% to 2.5%. Also the iron content stays constant. The aluminum concentration is changing the most in comparison to the percentage amount on the sample. The highest amount is seen in point 4 which was set on

one of the point shaped inclusions. The highest amount of oxygen is observed at the grain boundaries and additionally an increased amount of aluminum this is also seen in the EDX mappings in Figure 4.4. However, the EDX point measurements show a higher amount of oxide and aluminum at the grain boundaries and in the scratches on the grains a higher amount of oxygen is observed.

4.4 Electronic surface properties

In Figure 4.6 the topography image obtained by AFM and the complementary SKPFM image is presented with a topography and potential cross section. The scan size was 80 μm by 80 μm . The topography image Figure 4.6A shows a roughness of around 320 nm and the potential image Figure 4.6B shows a potential distribution of about ± 100 mV. The potential image shows features which are independent of the topography and distributed on the surface. The white spots are corresponding to higher potentials and black vice versa. The particles like structure can be attributed to Al/Fe inclusions and the darker area to damages in the oxide layer. In the area marked with the red frame was zoomed in and topography and potential mapping was evaluated again.

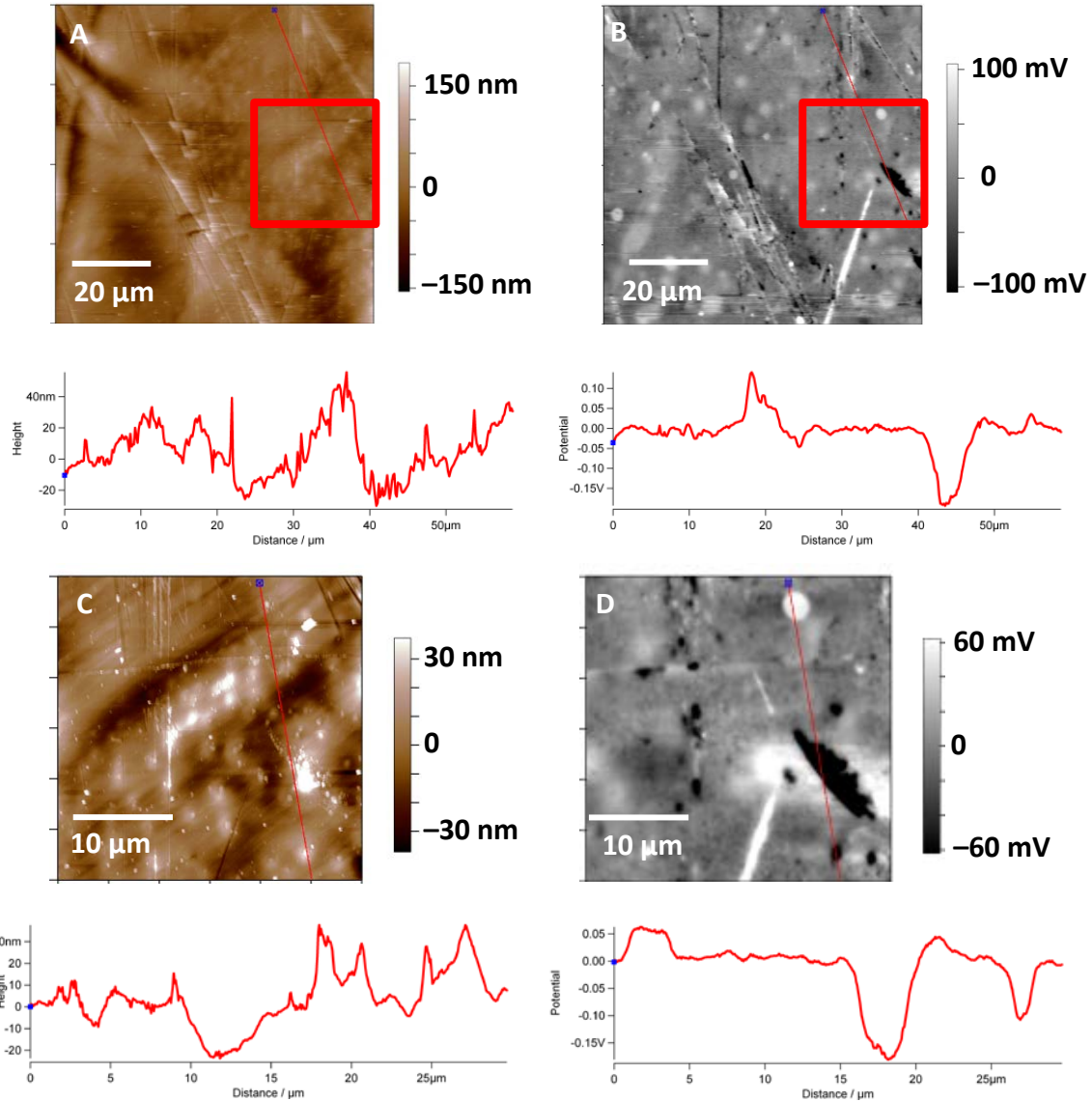


Figure 4.6: AFM (A, C) and SKPFM (B, D) images of a grain, first row (A, B) 80 nm by 80 nm scan area, second row 30 nm by 30 nm scan area, closer view in the area marked with the red frame, topography (A, C) and potential (B, D).

In Figure 4.6C the magnified AFM image and in Figure 4.6D the corresponding SKPFM image is shown. The height difference is around 70 nm and the potential is in the range of around ± 60 mV. The cross sections show again independence of the potential from the topography. However, the inclusions are embedded in the surface layer and a higher potential is observed.

To further analyze the potential difference EDX was performed after SKPFM measurements. In Figure 4.7 the performed SKPFM topography and potential images are shown. The images

were performed directly on the boundary of two grains (Figure 4.7). The top shows the microscopic picture and the red frame marks the area where the SKPFM measurement was performed. In Figure 4.7 the topography image obtained by AFM and the complementary SKPFM image. The roughness is about 450 nm and the potential is in the range of around ± 80 mV.

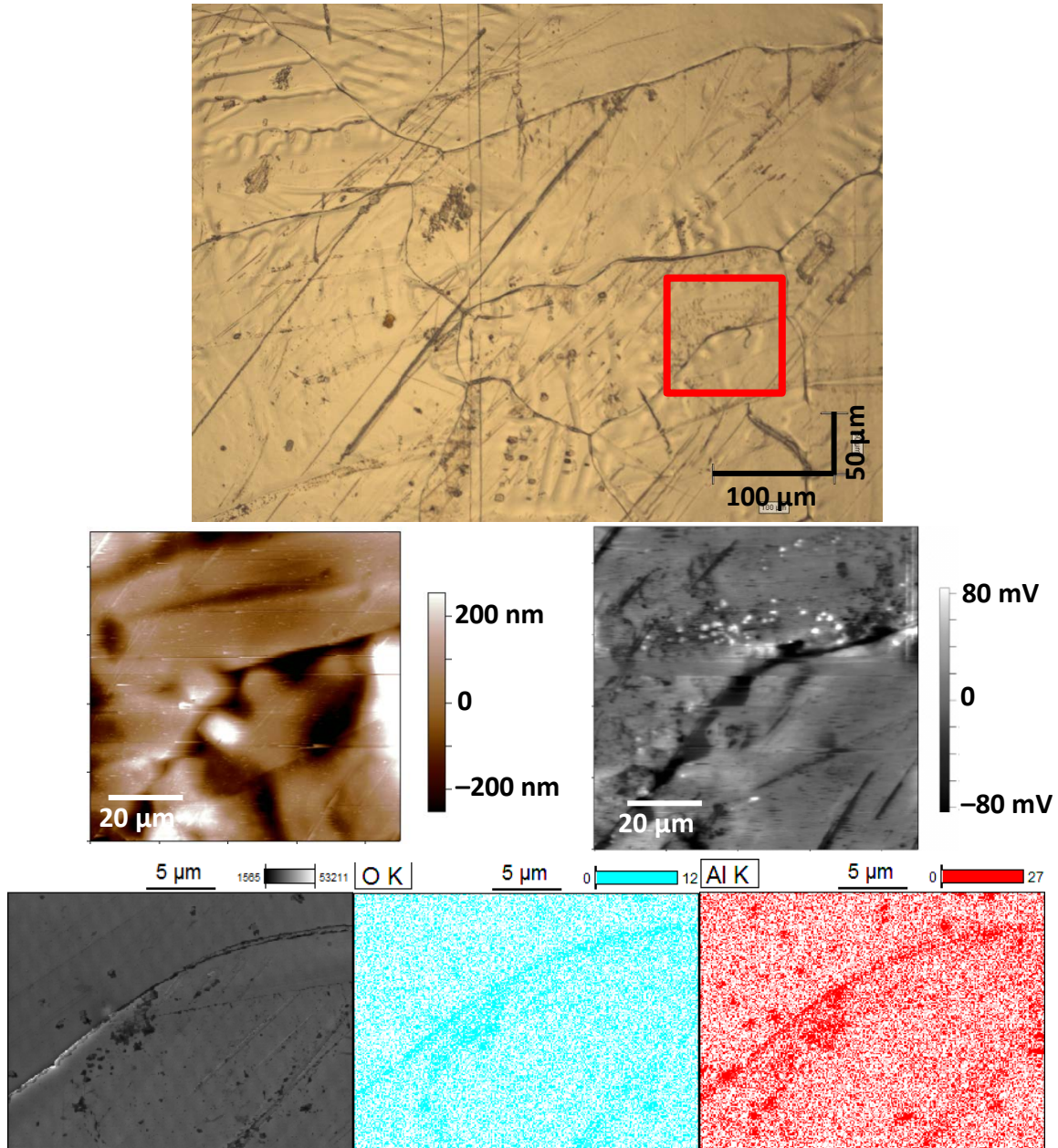


Figure 4.7: First row: microscopic picture. Second row: AFM (left) and SKPFM (right) image of a grain boundary, topography (left) and potential (right). Last row: SEM analysis (left) and EDX mappings of Al and O content at the before measured SKPFM area. SEM parameters: Mag = 1kx, WD = 4.8 mm, Detector = SE 2, EHT = 20.0 kV.

On the EDX mappings a higher surface concentration of aluminum and oxygen is observed, especially in the region of the grain boundary. On spots on the upper grain higher aluminum content is observed. However, the SKPFM measurements show higher potential spots on the surface corresponding to the aluminum/iron inclusions observed in the EDX maps.

4.5 Corrosion processes and mechanisms at different pH

The in-situ corrosion process was studied in 0.05 M NaCl at pH 7 as electrolyte. During the corrosion the open circuit potential was monitored and every 20 min Raman maps were performed.

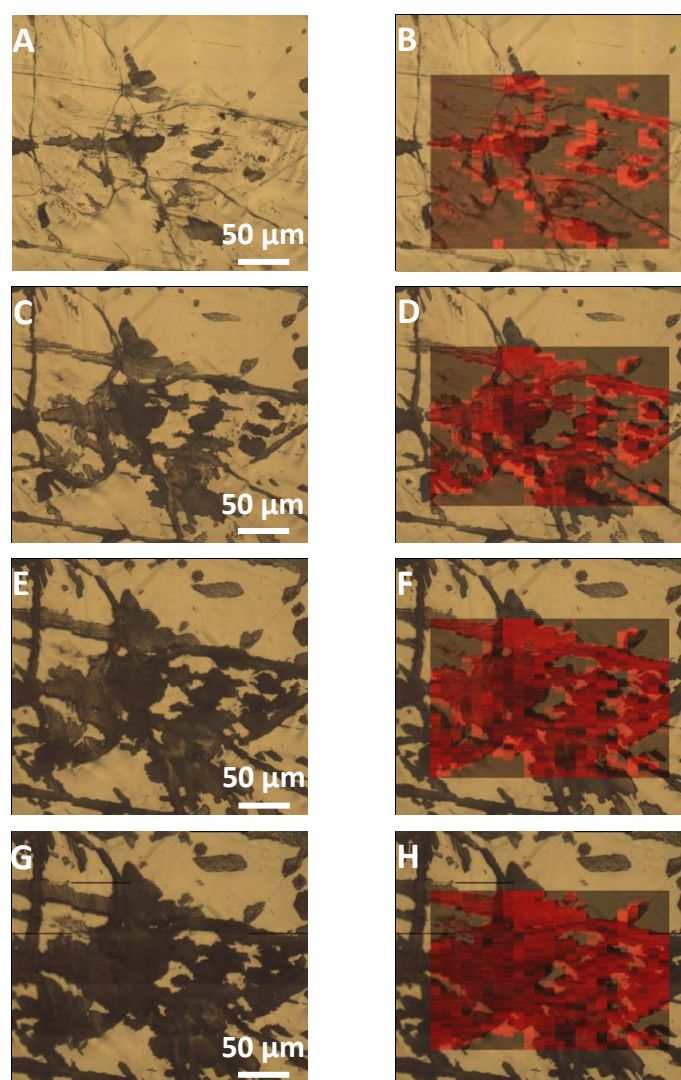


Figure 4.8: (A, C, E and G): Microscopic images of the zinc surface at 0, 20, 40 and 60 min related to the exposure to 0.05 M NaCl at pH 7. (B, D, F and H): Raman images at 430 cm^{-1} . (A and B): 0 min; (C and D): 20 min; (E and F): 40 min; (G and H): 60 min.

In Figure 4.8 the microscopic images and Raman maps of the zinc surface exposed to 0.05 M NaCl in neutral pH are shown. The sample was exposed 60 min to the electrolyte. In the microscopic images the growth of corrosion products during the exposure to the electrolyte was observed. The initial corrosion starts at defects on the zinc surface and at the grain boundaries. In Figure 4.9 a comparison of the Raman spectra are shown. The Raman spectra showed four different peaks which can be, according to Bernard [19–21] and Le Goff [22], assigned to ZnOH_2 , ZnO and ZnCO_3 . As main corrosion product ZnO and ZnCO_3 are observed. The peak at 430 cm^{-1} , which is presented in the Raman maps in Figure 4.8, is assigned as the Zn–O vibration.

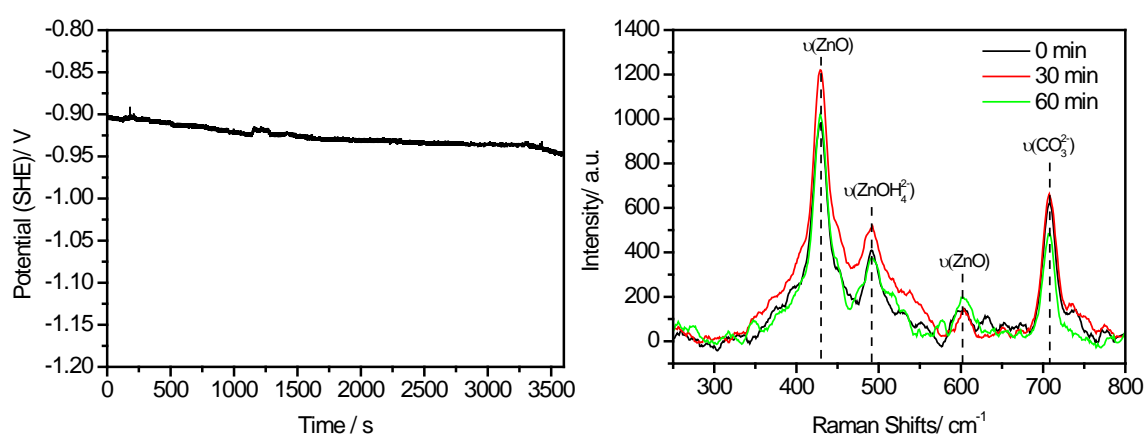


Figure 4.9: Left: Open circuit potential of the zinc surface measured during the experiment. Right: Comparison of the Raman spectra of the zinc surface at 0, 30 and 60 min related to the exposure to 0.05 M NaCl at pH7.

The potential recorded during the measurement started at $-0.9\text{ V}_{\text{SHE}}$ and showed a minute decrease during the exposure of around 50 mV (Figure 4.9) which could be due to the formation of corrosion products during the measurement. Additionally the pH was measured after the experiment and a significant increase to pH 13 was observed. At high pH according to Feitknecht et al [74–76] the formation of ZnO in chloride containing solution is stabilized. The initial potential is higher compared to the OCP measurements Hausbrand et al [60] performed in chloride containing borate buffer. This effect could be due to the not buffered electrolyte and therefore the increase of the potential.

Further the in-situ corrosion process was studied in 0.05 M NaCl at pH 3, 7 and 11. The electrolyte flow rate was set to 0.5 ml/min. During the corrosion the open circuit potential was monitored and every 20 min Raman measurements were performed.

In Figure 4.10 the microscopic pictures of the zinc surface exposed to neutral pH are shown. The sample was exposed 100 min to the electrolyte with a flow rate of 0.5 ml/min. In the microscopic images no significant change was observed. The potential recorded during the measurement started at $-1.1 V_{SHE}$ and showed a decrease during the exposure of around 100 mV (Figure 4.11). Pure zinc showed emerged in borate buffer containing 0.5 M NaCl a slight higher OCP of about $-1.05 V_{SHE}$ according to the experiments performed by Hausbrand et al. [60].

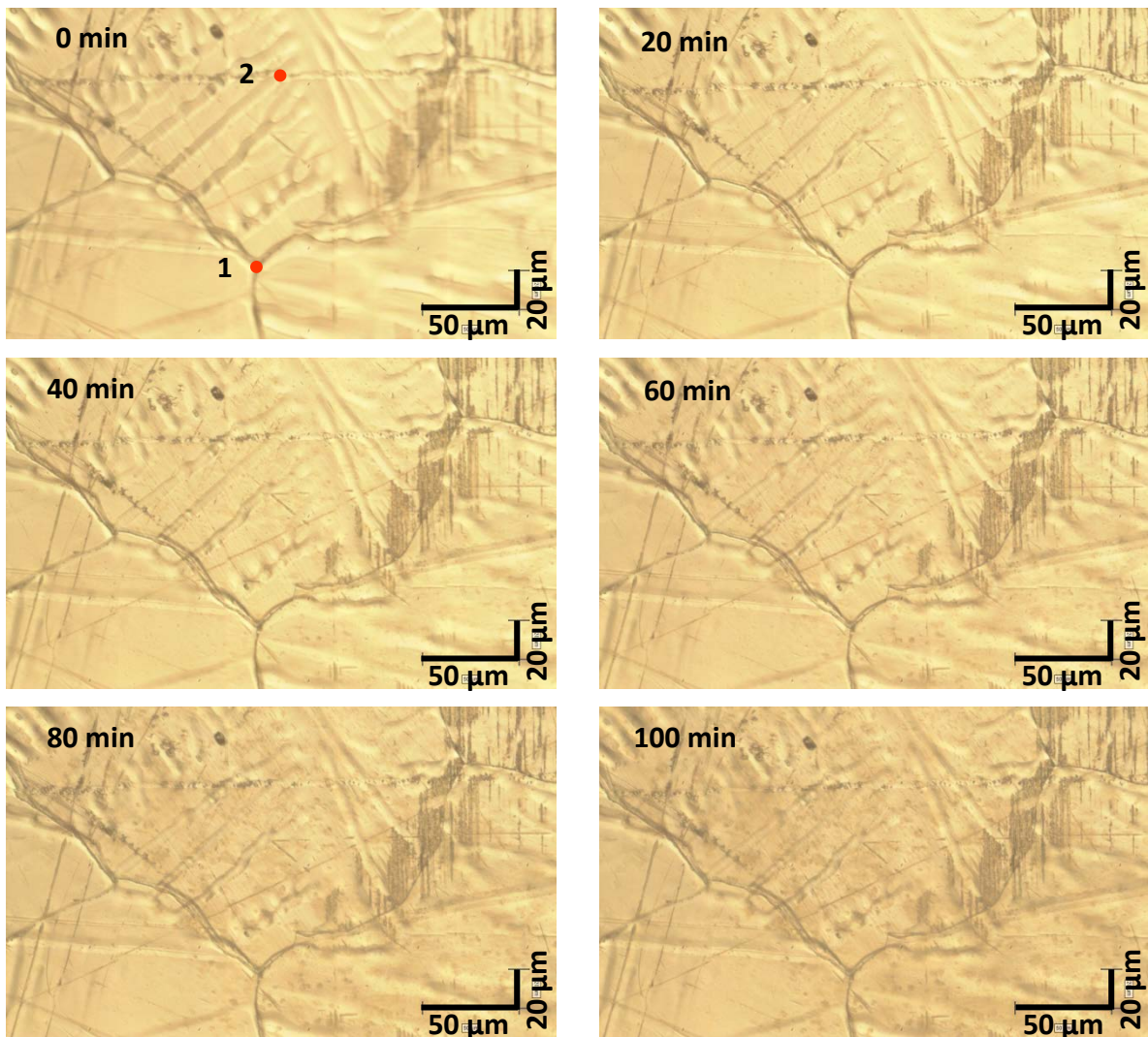


Figure 4.10: Microscopic images of the zinc surface at 0, 20, 40, 60, 80 and 100 min related to the exposure to 0.05 M NaCl and 0.5 ml/min flow at pH 7. ●: measurement points of the Raman spectra.

The Raman spectra taken at the red point marked in the microscopic picture in Figure 4.10 are shown in Figure 4.11. The measurement point 1 was set on a grain boundary and the

measurement point two on the grain. The Raman spectra show five different peaks which can be, according to Bernard [19–21] and Le Goff [22], assigned to ZnOH_2 , ZnO and ZnCO_3 .

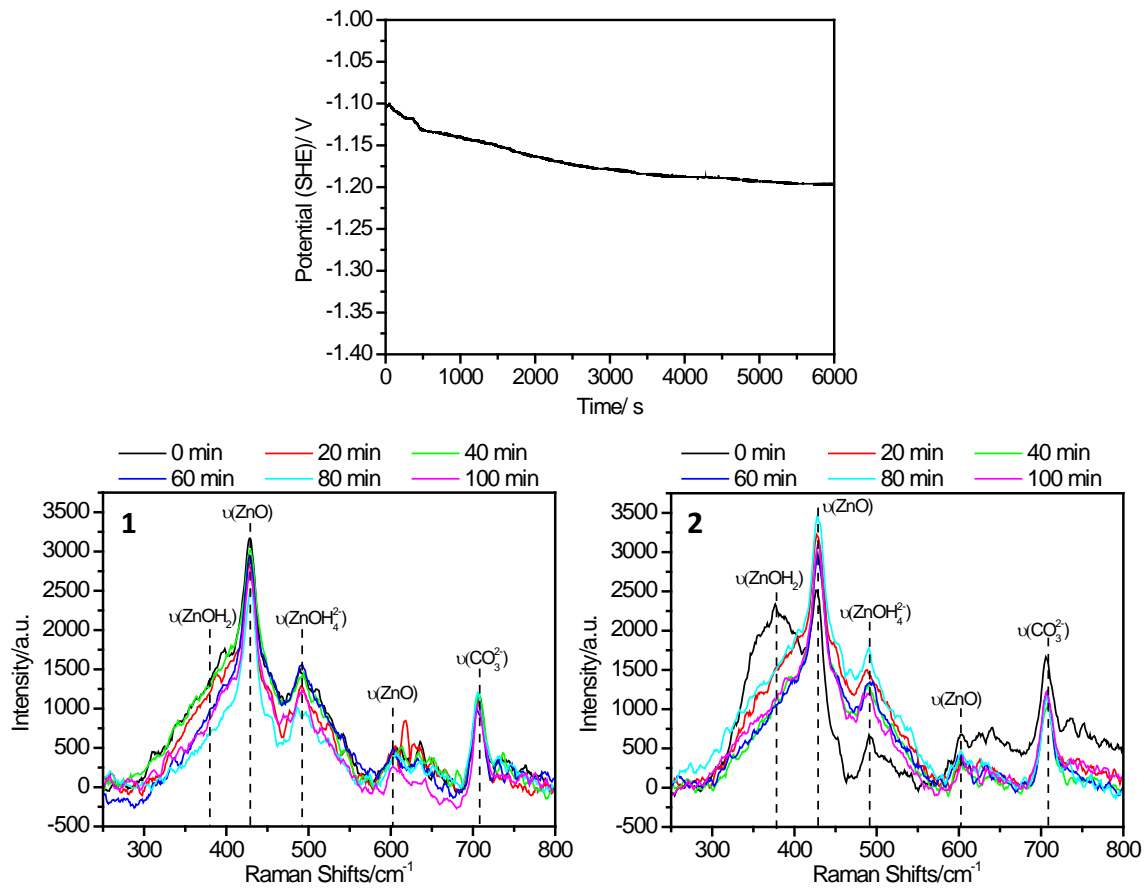


Figure 4.11: Top: Open circuit potential measured during the experiment. Raman spectra at 0, 20, 40, 60, 80 and 100 min related to the exposure to 0.05 M NaCl and 0.5 ml/min flow at pH 7.

The carbonate peak at 702 cm^{-1} stayed constant during the exposure at both points. At the grain boundary (Figure 4.11 Point 1) the ZnO and ZnOH_2 amount is slowly decreasing, which could be due to dissolution of zinc and this was also observed by Klemm et al [184]. At point 2 an increase of ZnO and ZnOH_2 was observed. However the equilibrium of the zinc corrosion was very fast reached.

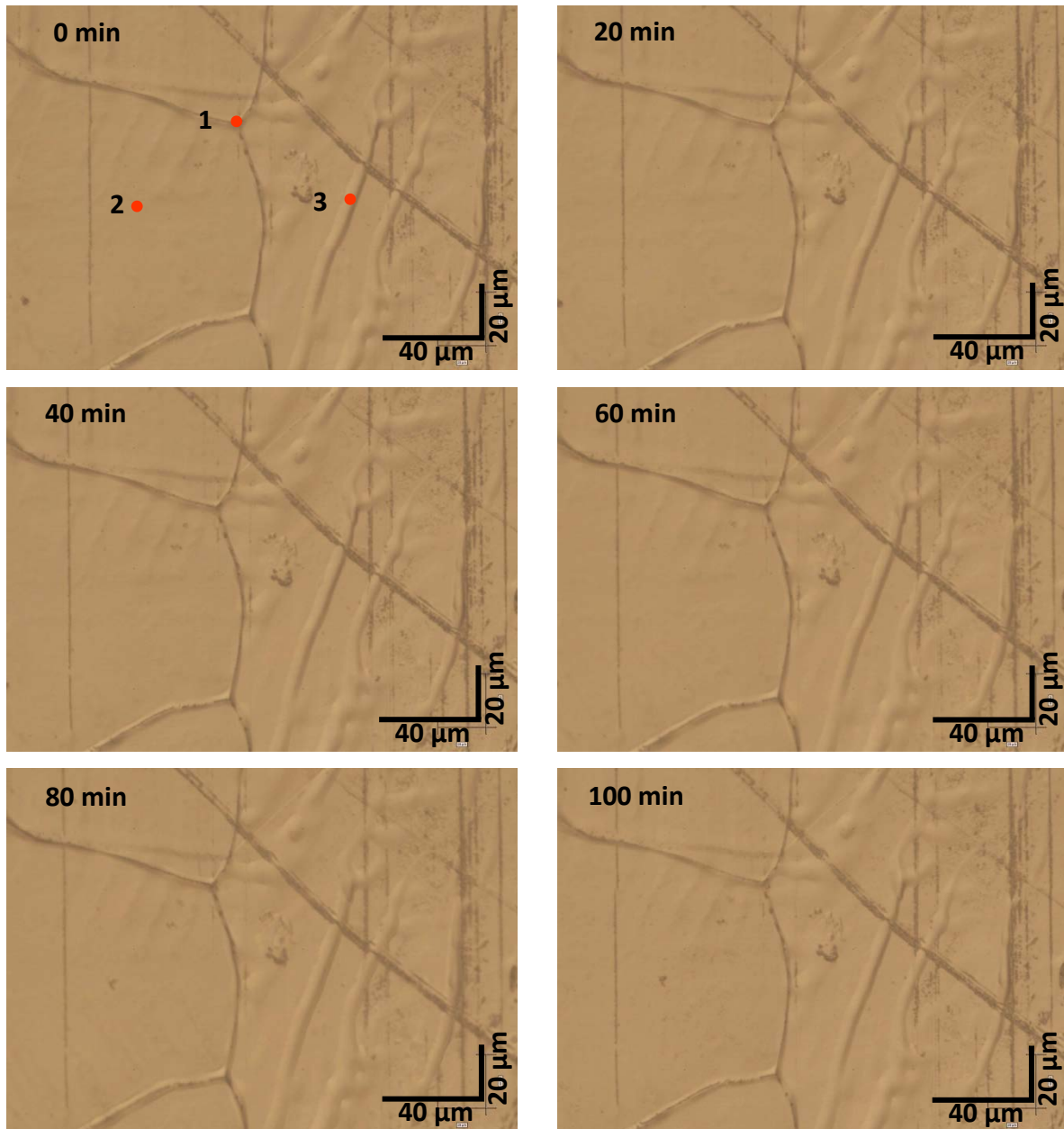


Figure 4.12: Microscopic images of the zinc surface at 0, 20, 40, 60, 80 and 100 min related to the exposure to 0.05 M NaCl and 0.5 ml/min flow at pH 3. ●: measurement points of the Raman spectra.

In Figure 4.12 the microscopic pictures of the zinc surface exposed to pH 3 are shown. The sample was exposed 100 min to the electrolyte with a flow rate of 0.5 ml/min. In the microscopic images no significant change was observed during the exposure. The potential recorded during the measurement started at $-1.35 V_{\text{SHE}}$ and showed an increase during the exposure of around 75 mV (Figure 4.13). Hausbrand et al [60] also observed a decrease of the OCP with decreasing pH.

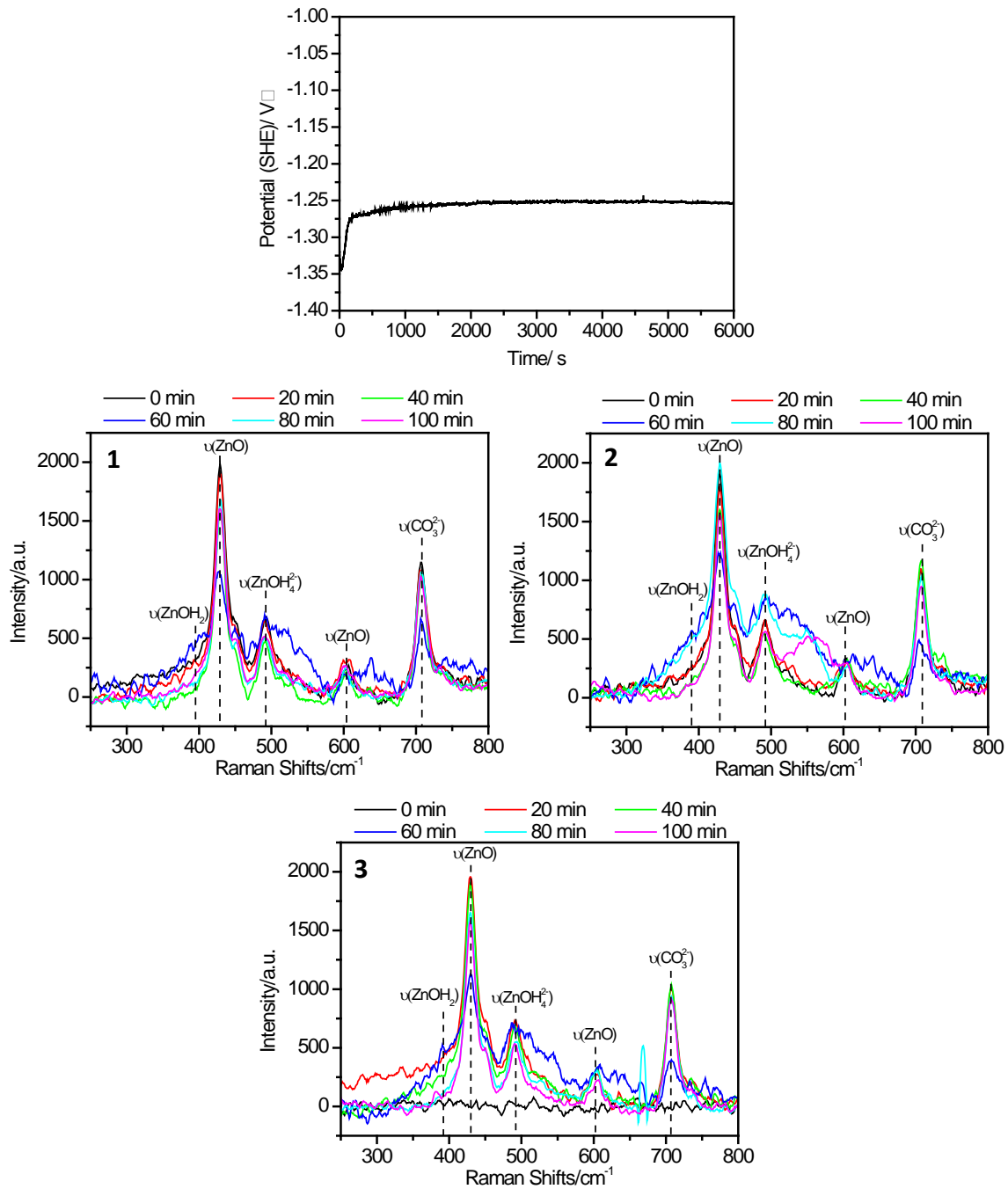


Figure 4.13: Top: Open circuit potential measured during the experiment. Raman spectra at 0, 20, 40, 60, 80 and 100 min related to the exposure to 0.05 M NaCl and 0.5 ml/min flow at pH 3.

The Raman spectra taken at the red points are marked in the microscopic picture in Figure 4.12 and are shown in Figure 4.13. The measurement point 1 was set on a grain boundary, the measurement point 2 on the grain and the third point was set on a dent in the grain. The Raman spectra show five different peaks which can be, according to Bernard [19–21] and Le Goff [22], assigned to ZnOH_2 , ZnO and ZnCO_3 .

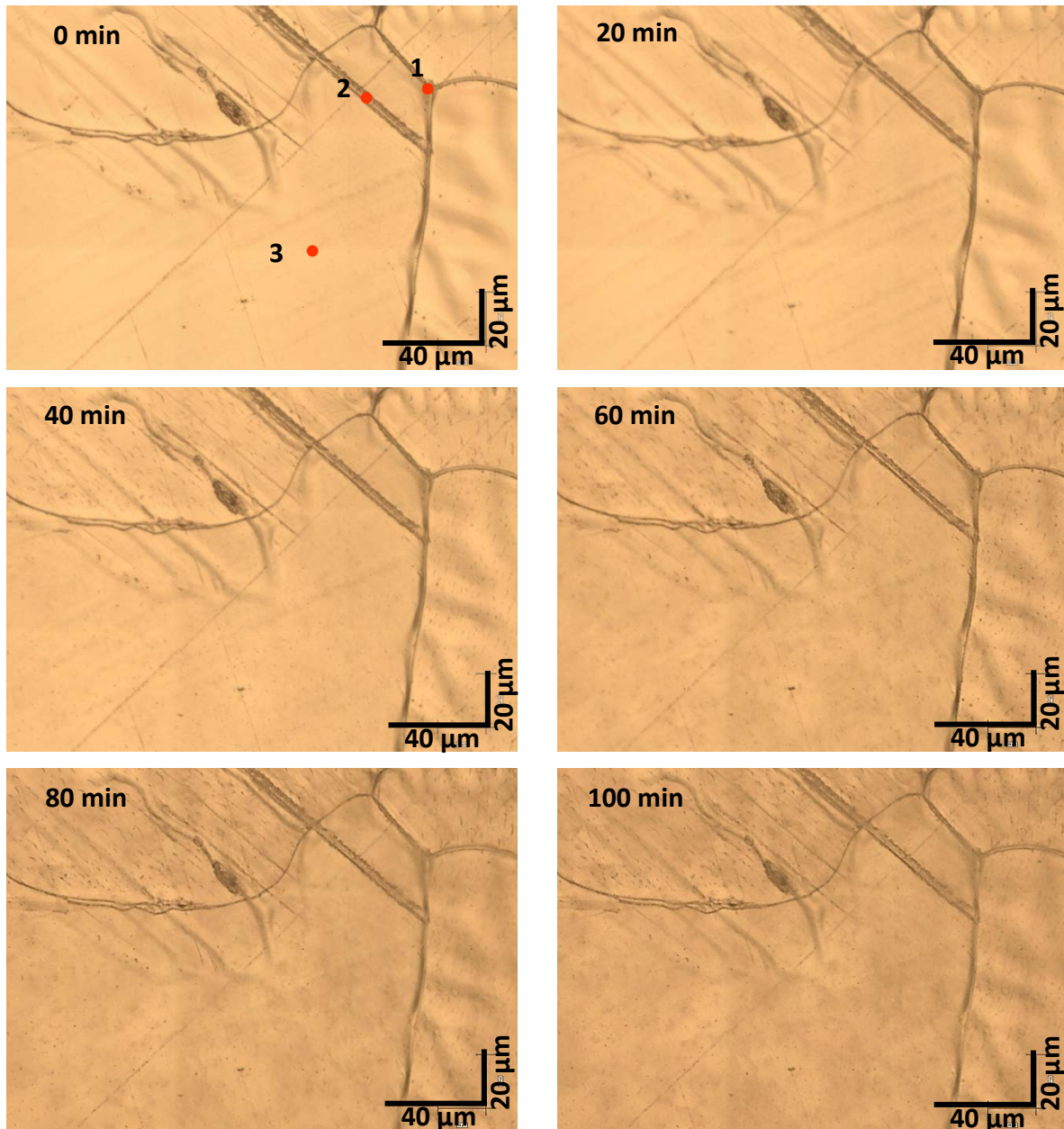


Figure 4.14: Microscopic images at 0, 20, 40, 60, 80 and 100 min related to the exposure to 0.05 M NaCl and 0.5 ml/min flow at pH 11. •: measurement points of the Raman spectra.

At measurement points one and two Raman peaks of zinc hydroxide, carbonate and oxide were observed. The carbonate peak at 702 cm^{-1} was increasing during the exposure. The amount of hydroxide and oxide was slowly decreasing. The third measurement point showed neither zinc oxide, hydroxide nor carbonate peak in the beginning which could be due to a very thin oxide layer in this area. After 20 min the zinc oxide and hydroxide peaks strongly increased. During the further exposure the amount of hydroxide and oxide was slowly decreasing.

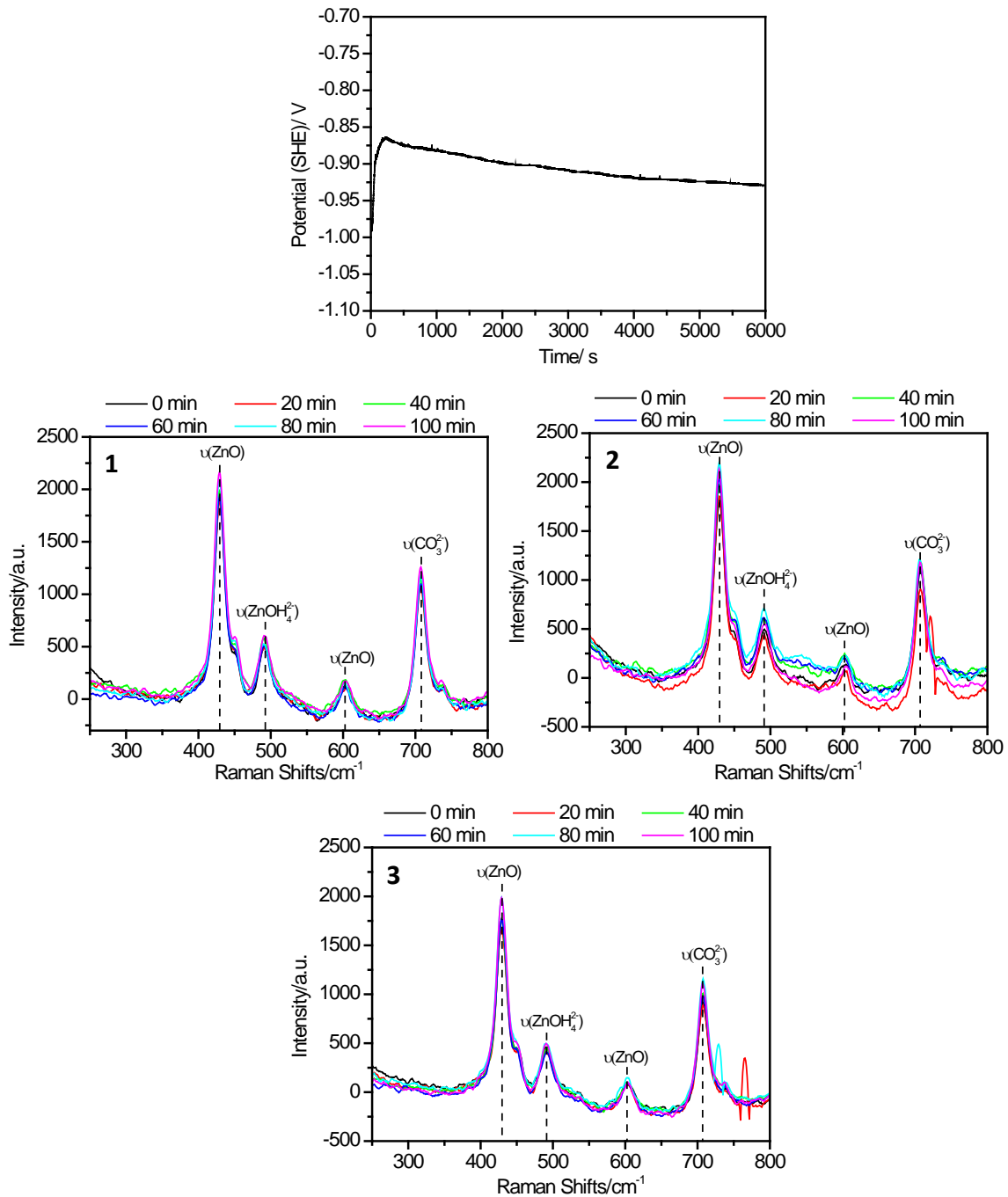


Figure 4.15: Top: Open circuit potential measured during the experiment. Raman spectra at 0, 20, 40, 60, 80 and 100 min related to the exposure to 0.05 M NaCl and 0.5 ml/min flow at pH 11.

In Figure 4.14 the microscopic pictures of the zinc surface exposed to pH 11 are shown. The sample was exposed 100 min to the electrolyte with a flow rate of 0.5 ml/min. In the microscopic images after 40 min the inclusion on the grains are visible. The potential recorded during the measurement started at $-1.0 V_{\text{SHE}}$ and showed an increase in the first few seconds during the exposure of around 125 mV (Figure 4.15). Afterwards the potential

slowly decreased. The Raman spectra, taken at the red point marked in the microscopic picture in Figure 4.14 is shown in Figure 4.15.

The measurement point 1 was set on a grain boundary, the measurement point two on a scratch in the grain and the third point was set on the grain. The Raman spectra show four different peaks which can be, according to Bernard [19–21] and Le Goff [22], assigned to ZnOH_2 , ZnO and ZnCO_3 . The carbonate peak at 702 cm^{-1} stays during the exposure at both points constant and the ZnO and ZnOH_2 amount is slowly increasing, which could be due to thickening of the oxide layer.

4.6 Conclusions

The SEM images clearly demonstrated inclusions on the surface and by means of EDX this inclusions could be identified as aluminum/iron particles on the surface. Additionally the SKPFM measurements showed potential differences on the grain independent of the topography which could be assigned to the inclusions observed in SEM and EDX. The EBSD measurement has shown the preferred orientation of the crystallized zinc underneath the native oxide layer to be 0001.

The in-situ corrosion analysis performed in 0.05 M NaCl showed the growth of mainly zinc oxide preferred at the grain boundaries and at defects on the surface. Additionally an increase of the pH was observed which stabilize the formed zinc oxide on the surface. The Raman spectra obtained during electrolyte flow showed different composition of the oxide layer directly after the exposure to the electrolyte dependent on the pH. In the case of pH 3 the dissolution and oxidation of zinc were in equilibrium therefore the OCP stayed constant during the exposure. In neutral and alkaline pH the OCP was 100 mV decreasing. At pH 7 the amount of zinc oxide and hydroxide increased on the grain and stayed constant at the grain boundary. At pH 11 the amount of zinc oxide and hydroxide was slowly increasing at all points.

5 In-situ corrosion analysis of zinc magnesium alloy coated steel

The initial corrosion of hot dipped galvanized zinc magnesium alloy coated steel was investigated by means of Raman spectroscopy in pH 3, 7 and 11 containing 0.05 M sodium chloride solution. To prevent pH changes of the electrolyte solution due to oxygen reduction the measurement were performed under a high electrolyte flow. Additionally the surface morphology and bulk composition was characterized by means of scanning electron microscopy (SEM) and energy dispersive X-ray spectroscopy (EDX), respectively. The Raman spectra showed different composition of the oxide layer after the exposure to the electrolyte dependent on the pH. In the case of pH 3 and pH 11 the zinc (hydr)oxide and carbonate stayed constant during the exposure. In pH 7 the zinc hydr(oxide) and carbonates were during the measurement dissolving.

5.1 Experimental

5.1.1 Materials and sample preparation

If not indicated otherwise, all chemicals were of p.a. grade (pro analysis) and were used as supplied without any further purification. As substrates hot-dip galvanized zinc magnesium coated steel sheets (ZM) were used as samples of technical interest. The interstitial free ZM steel (sheet thickness 0.85 mm) was supplied by voestalpine Stahl GmbH (Linz, Austria) in the non skin passed state, i.e. without being temper rolled after application of the zinc coating. The thickness of the zinc coating (alloy composition: Zn + 2% Al + 2% Mg) after hot dip galvanizing was 7.5 μm . Samples were cut from the supplied material in 10 by 10 mm² samples and cleaned in three different solvents in an ultra-sonic bath for 20 min to ensure complete removal of any oils or surface contaminations. As solvents tetrahydrofuran (THF), iso-propanol and ethanol with analytical grade (Merck KGaA, Darmstadt, Germany) were used. After every solvent treatment the samples were dried under flow of dry nitrogen.

5.1.2 Surface Analysis

Prior to the in-situ corrosion test the surface morphology and chemistry was analyzed by means of SEM, AFM and EDX. Morphological characterization and surface composition was verified by means of a SEM with a field emission gun (LEO 1550VP) combined with an energy-dispersive x-ray spectroscopy (EDX) unit (Oxford Instruments). The measurements were performed at an accelerating voltage of 20 kV and a working distance of 8 mm, which results in a penetration depth of electrons higher than 1 μm .

5.1.3 In-situ Raman spectroscopy

The corrosion products were analyzed during the corrosion process by means of a confocal Raman microscope. The Raman spectra were obtained using a InVia Renishaw confocal Raman microprobe system (Renishaw plc, UK) equipped with an Leica DM 2500 M confocal microscope and an air cooled HeNe laser ($\lambda = 632.8 \text{ nm}$). Measurements were performed using a HCX APO L63x immersion objective for water with a numerical aperture of 0.9 and a 1800 grooves/mm diffraction grating. The laser power was set to 1.75 mW and an exposure time of 30 s. The in-situ Raman spectroscopic measurements were performed within a custom made cell with an electrolyte volume of 3 ml. A scheme of the setup is shown in Figure 4.1. The flow through cell is equipped with a three electrode setup to measure also the potential during the corrosion process. The samples were exposed to pH 3, 7 and 11 containing 0.05 M NaCl solution and the time dependent Raman spectra were taken in intervals of 40 min. Prior to the Raman measurements microscopic pictures were taken.

5.2 Surface morphology and bulk composition of the alloy

Due to the addition of aluminum and magnesium and the iron dissolution in the galvanizing zinc bath the considered zinc coating is alloyed with a small amount of these elements according to their solubility in liquid zinc [181–183]. After emersion from the zinc bath, the zinc layer is cooled by gas-wiping dies blowing air or nitrogen. The morphology of the samples surface is shown in Figure 5.1.

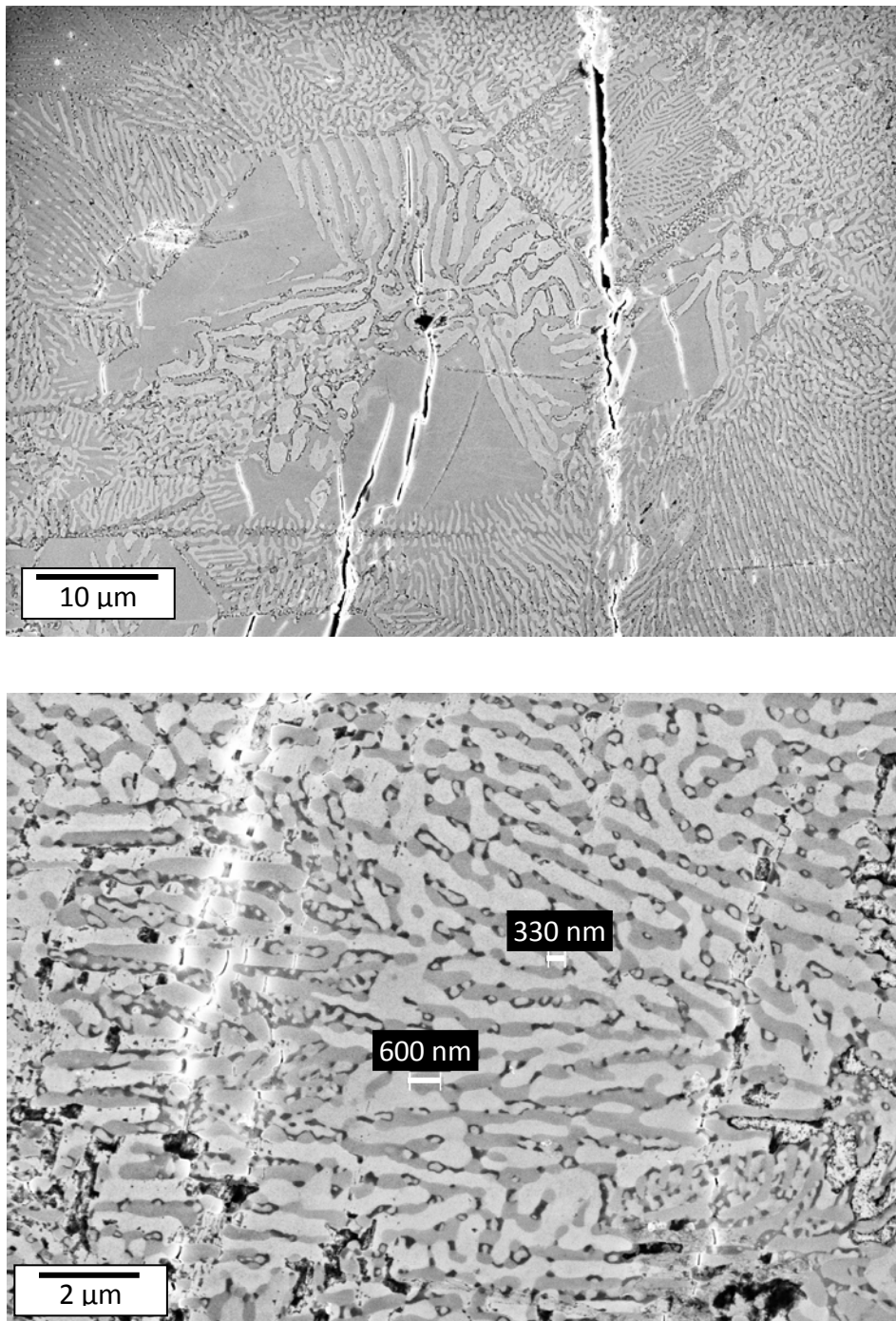


Figure 5.1: Top: SEM analysis of zinc magnesium aluminum coated steel surface. SEM parameters: Mag = 5kx, WD = 9 mm, Detector = InLens, EHT = 8.0 kV. Bottom: SEM analysis of zinc magnesium aluminum coated steel surface, SEM parameters: Mag = 20kx, WD = 9 mm, Detector = InLens, EHT = 10.0 kV.

The Zn–Mg–Al coating has a complex micro–structure composed of several different phases, it was shown that the topmost surface is covered by a smooth, homogeneous oxide layer

consisting of a mixture of magnesium oxide and aluminum oxide, exhibiting a higher amount of magnesium than aluminum and a total film thickness of 4.5 to 5 nm [185]. In Figure 5.1 larger grains are observed with areas of 5 μm by 7 μm and areas with striped structure. In Figure 5.1 bottom the striped structure is enlarged and the stripes have a width of below 1 μm and a length of some μm .

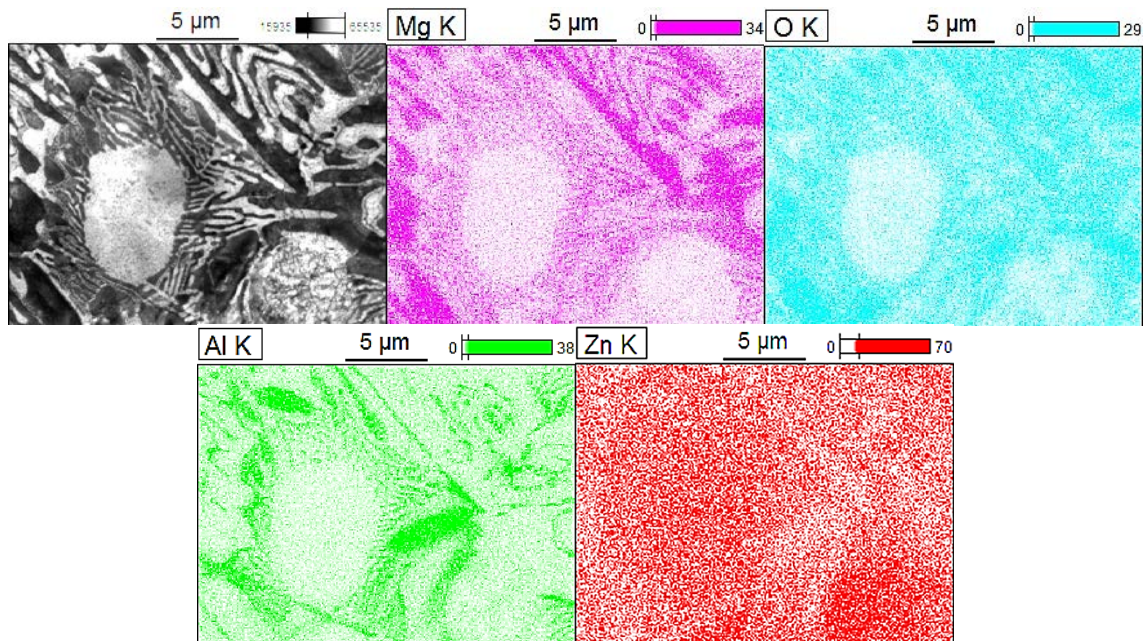


Figure 5.2: First row: SEM analysis (left) and EDX mappings of local Mg, O, Al and Zn content of hot-dipped galvanized steel surface. SEM parameters: Mag = 5kx, WD = 5 mm, Detector = SE 2, EHT = 20.0 kV.

The bulk composition of the employed alloy was studied by means of energy dispersive X-ray spectroscopy. The SEM picture is shown in Figure 5.2 with the complementary EDX analysis of the local content of aluminum, magnesium, zinc and oxygen. In the SEM picture larger areas and the striped like structure is observed. The larger area seems to consist of zinc with fewer amounts of aluminum and magnesium. Also the oxide layer seems to be thinner in comparison to the striped like structure. The stripe like structure consists of two grains. The areas which are illustrated in the SEM in white consist mostly of aluminum and the black areas have higher magnesium content.

5.3 Corrosion process and mechanisms at different pH

The in-situ corrosion process was studied in 0.05 M NaCl at pH 7. During the corrosion process the open circuit potential was monitored and every 30 min Raman spectra were obtained.

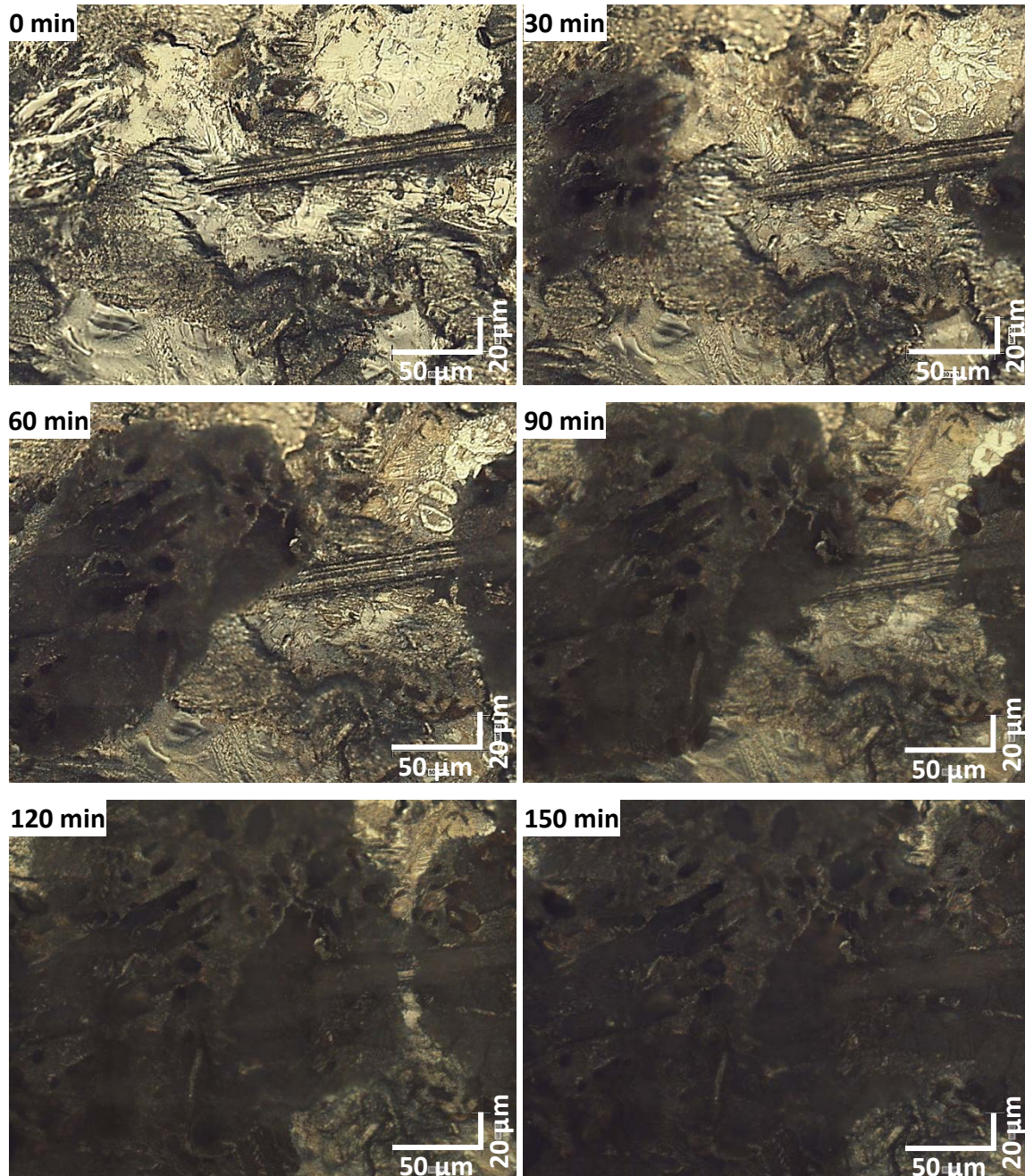


Figure 5.3: Microscopic images of Zn–Mg–Al alloy coated steel at 0, 30, 60, 90, 120 and 150 min related to the exposure to 0.05 M NaCl at pH7.

In Figure 5.3 the microscopic pictures of the ZM surface exposed to neutral sodium chloride solution are shown. The sample was exposed 150 min to the electrolyte. The corrosion

started at several points on the surface and was growing over the surface with time. This behavior was also observed by Sullivan et al [186] with time lapse imaging.

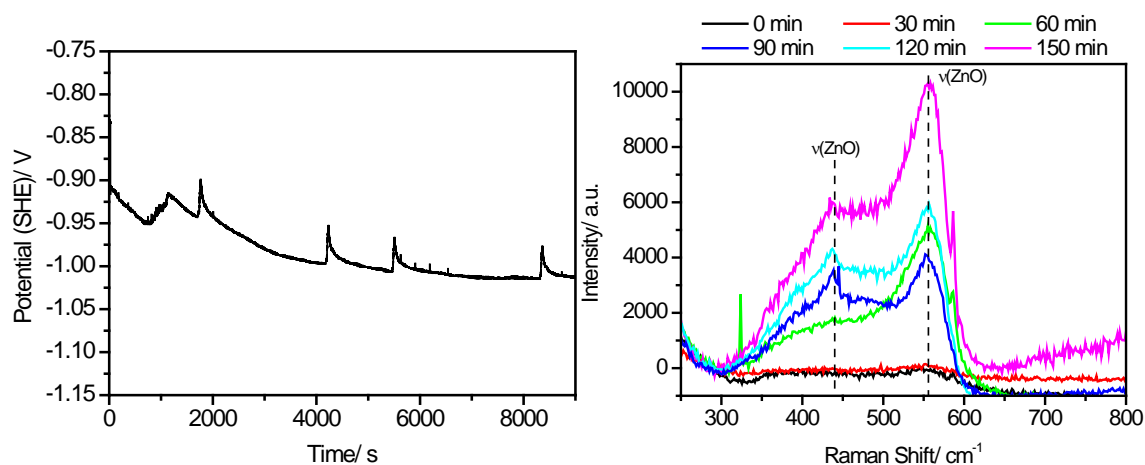


Figure 5.4:Left: Open circuit potential of the zinc magnesium surface measured during the experiment. Right: Comparison of the Raman spectra of the zinc magnesium surface at 0, 30, 60, 90, 120 and 150 min related to the exposure to 0.05 M NaCl at pH7.

The potential recorded during the measurement started at $-0.9 V_{SHE}$ and showed a minute decrease during the exposure of around 100 mV (Figure 5.4) which could be due to the formation of corrosion products during the measurement. Additionally the pH was measured after the exposure and a significant increase to pH 13 was observed. Comparisons of the Raman spectra are shown in Figure 5.4. The Raman spectra showed two peaks which can be, according to Bernard [19–21] and Le Goff [22], assigned to ZnO. At high pH the formation of ZnO in chloride containing solution is stabilized according to Feitknecht [74–76]. The initial potential is higher compared to the results of Hausbrand et al [60]. This could be due to the change of the pH during the measurement.

Further the in-situ corrosion process was studied in 0.05 M NaCl with varied pH and with 0.5 ml/min flow through. During the corrosion process the open circuit potential was monitored and every 40 min Raman measurement was performed.

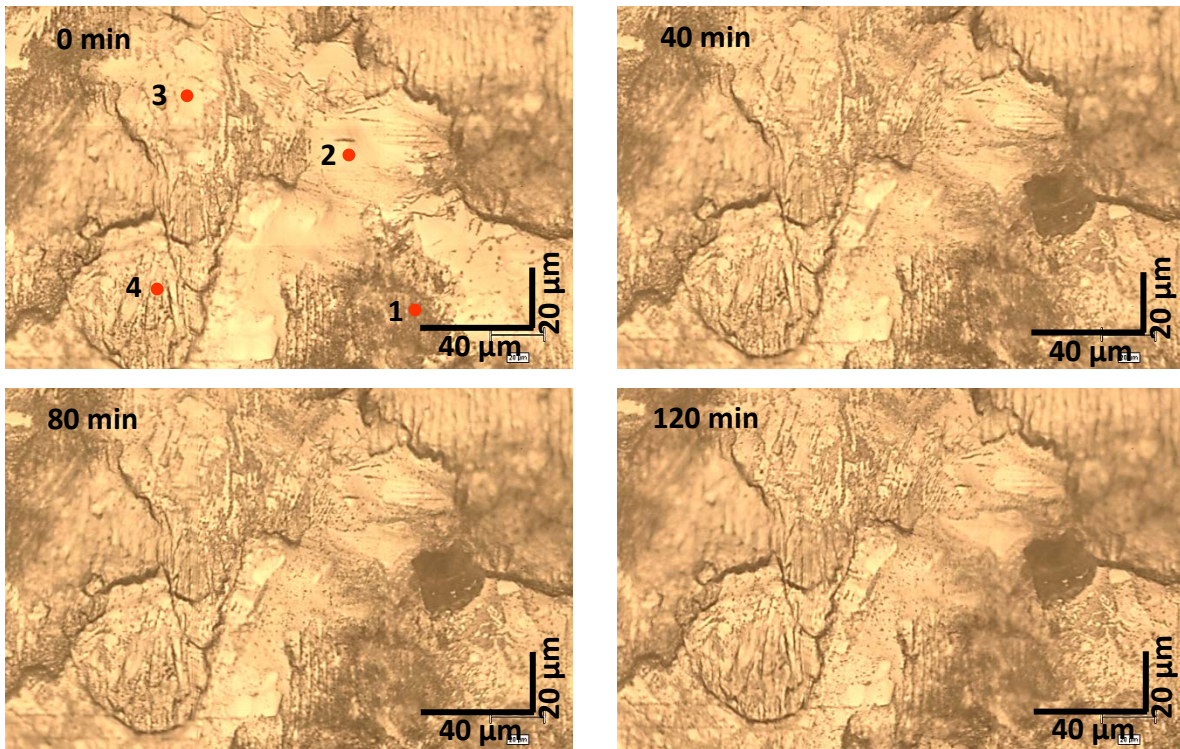


Figure 5.5: Microscopic images at 0, 40, 80 and 120 min related to the exposure to 0.05 M NaCl and 0.5 ml/min flow at pH 3. • : measurement points of the Raman spectra.

In Figure 5.5 the microscopic pictures of ZM exposed to pH 3 are shown. The sample was exposed 120 min to the electrolyte under flow. In the microscopic images no significant change is observed. The potential recorded during the measurement started at $-1.35 V_{SHE}$ and increased in the first ten minutes to $-1.27 V_{SHE}$ (Figure 5.6) and was then constant. The Raman spectra taken at the red points marked in the microscopic picture in Figure 5.5 are shown in Figure 5.6. The points were set at areas with different bulk composition. The Raman spectra show four different peaks which can be, according to Bernard [19–21] and Le Goff [22], assigned to $ZnOH_2$, ZnO and $ZnCO_3$.

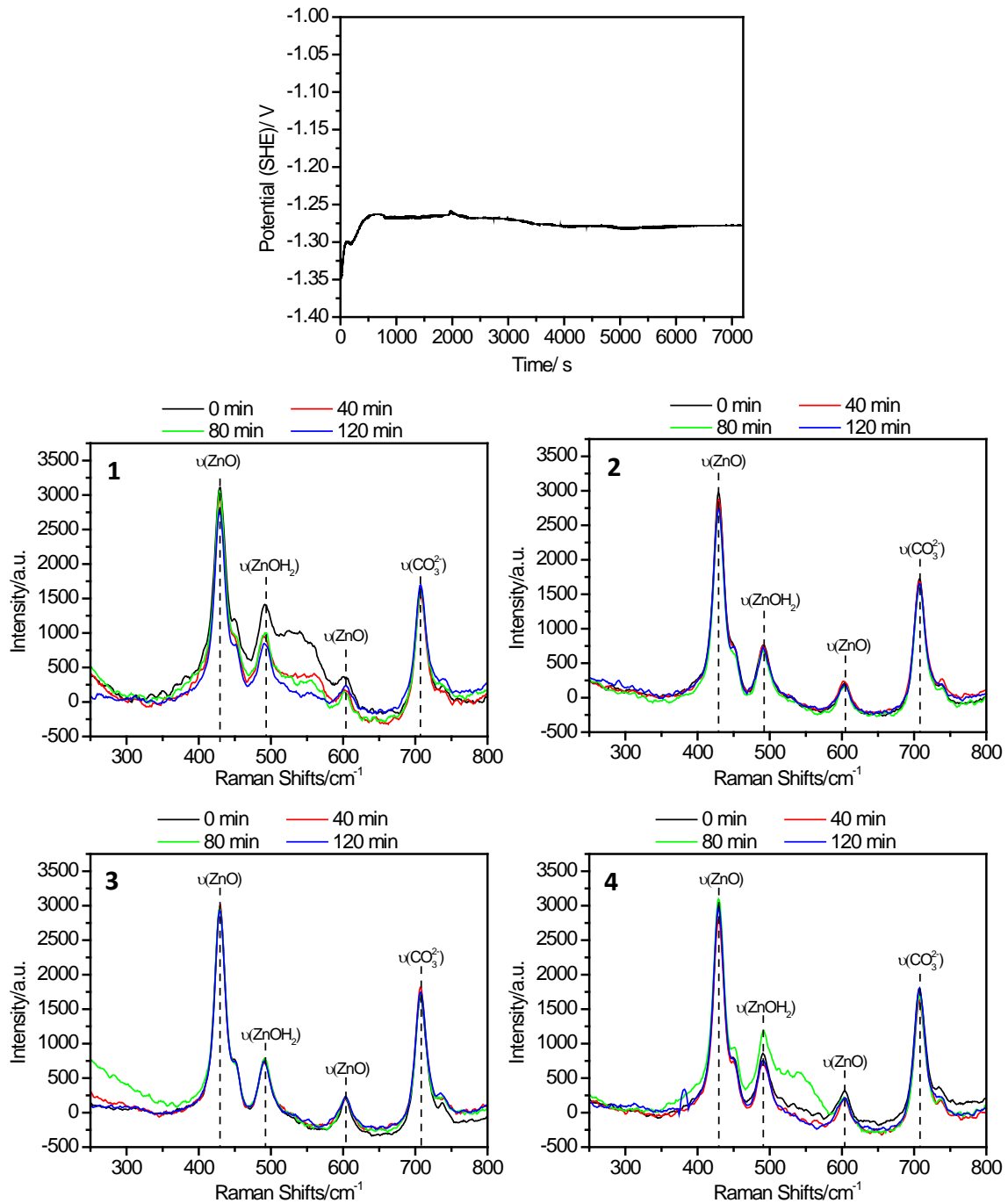


Figure 5.6: Top: Open circuit potential taken during the experiment. Raman spectra at 0, 40, 80 and 120 min related to the exposure to 0.05 M NaCl and 0.5 ml/min flow at pH 3.

In Figure 5.7 the microscopic pictures of ZM exposed to neutral pH are shown. The sample was exposed 120 min to the electrolyte under flow. In the microscopic images no significant change is observed.

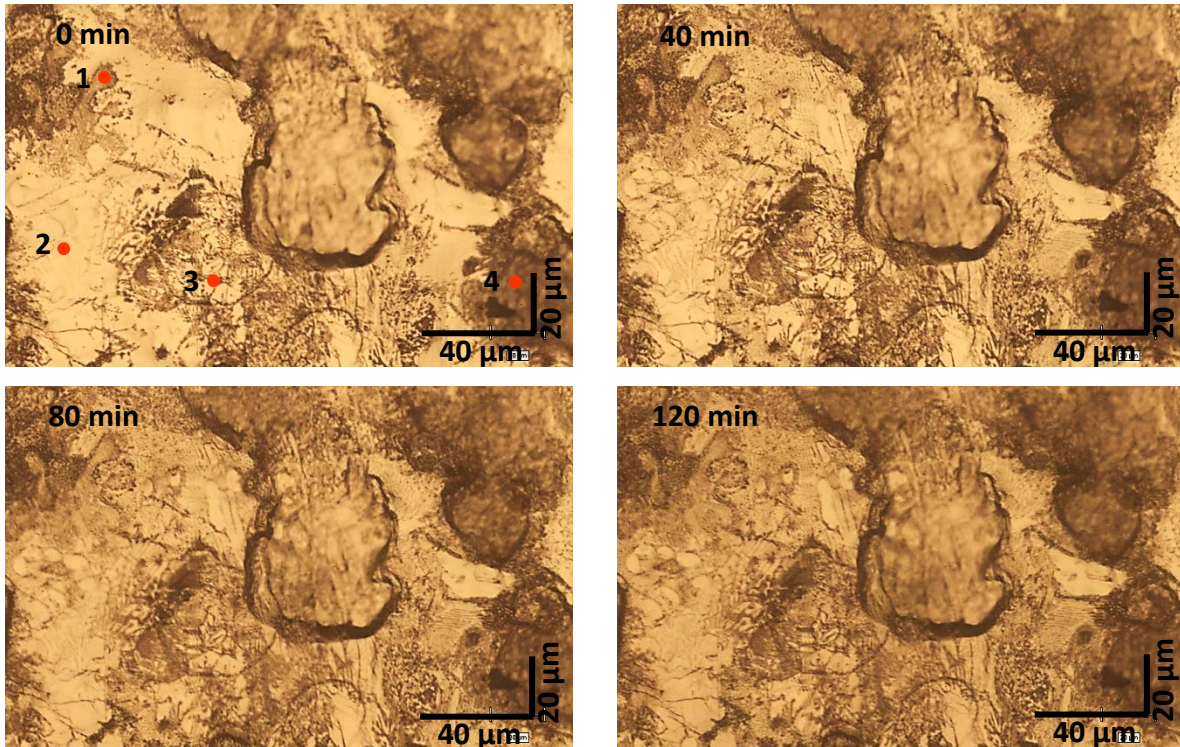


Figure 5.7: Microscopic images at 0, 40, 80 and 120 min related to the exposure to 0.05 M NaCl and 0.5 ml/min flow at pH 7. ●: measurement points of the Raman spectra.

The potential recorded during the measurement stayed constant at $-1.2 V_{SHE}$ (Figure 5.8). The Raman spectra taken at the red points marked in the microscopic picture in Figure 5.7 are shown in Figure 5.8. The points were set at areas with different bulk composition. The Raman spectra show four different peaks which can be, according to Bernard [19–21] and Le Goff [22], assigned to $ZnOH_2$, ZnO and $ZnCO_3$.

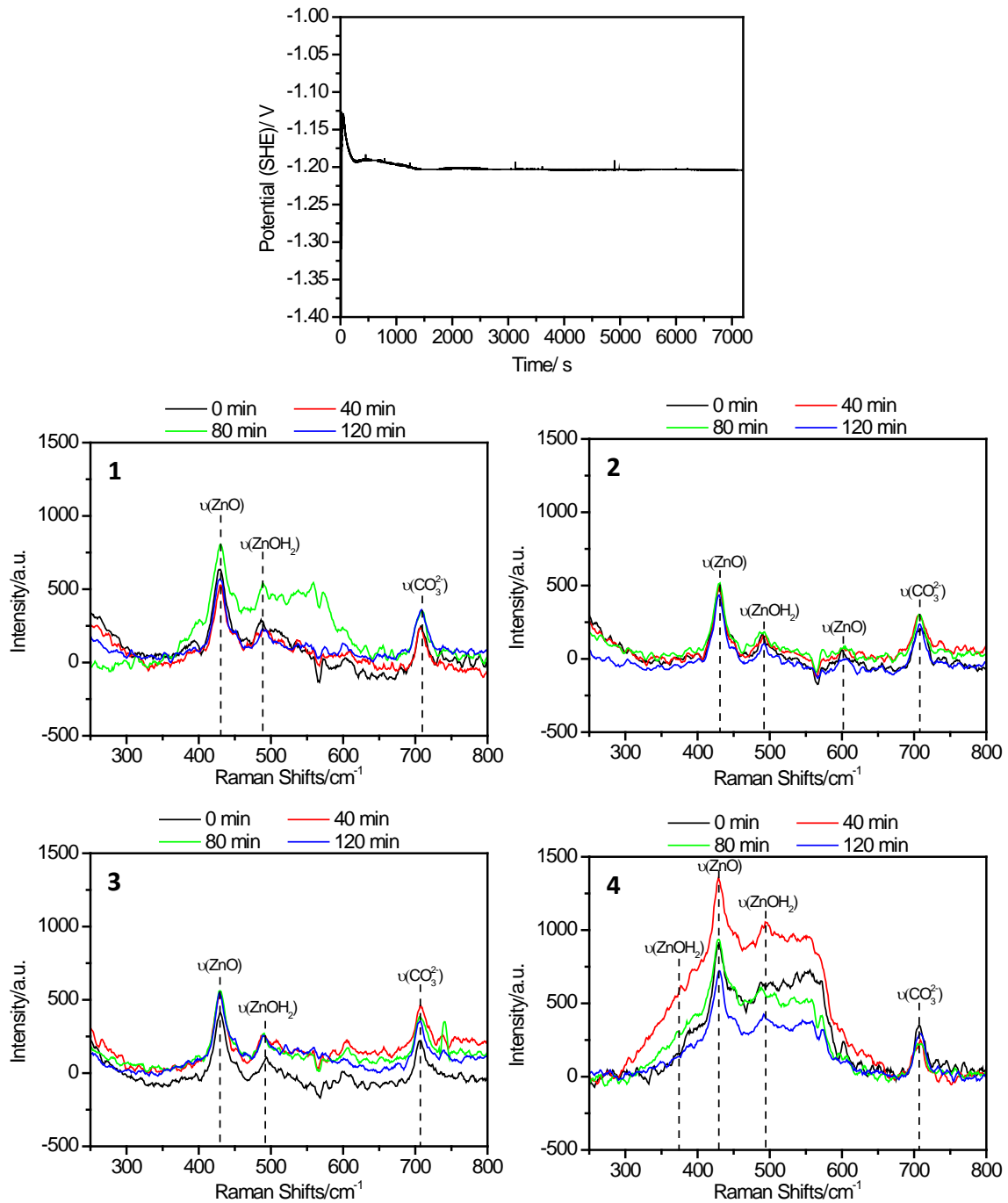


Figure 5.8: Top: Open circuit potential taken during the experiment. Raman spectra at 0, 40, 80 and 120 min related to the exposure to 0.05 M NaCl and 0.5 ml/min flow at pH 7.

In Figure 5.9 the microscopic pictures of ZM exposed to alkaline pH are shown. The sample was exposed 120 min to the electrolyte under flow. In the microscopic images corrosion starts to occur.

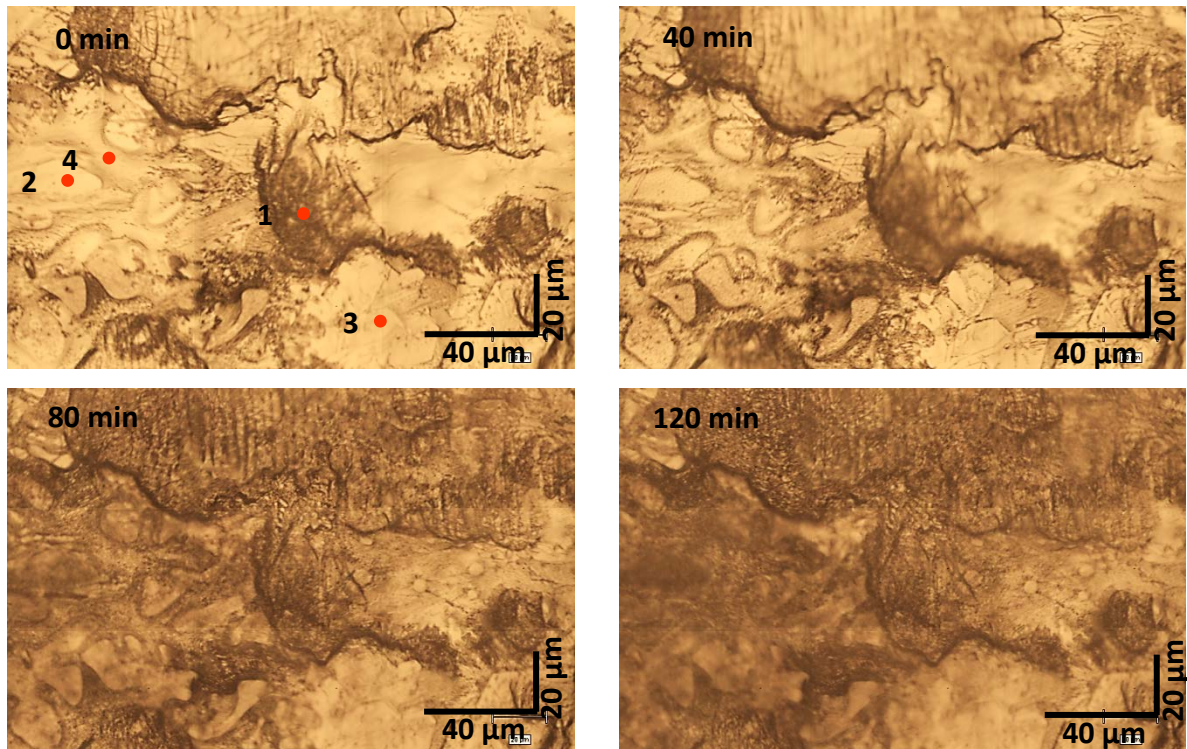


Figure 5.9: Microscopic images at 0, 40, 80 and 120 min related to the exposure to 0.05 M NaCl and 0.5 ml/min flow at pH 11. ● : measurement points of the Raman spectra.

The OCP started at $-1.05 V_{SHE}$ and stayed one hour constant. After one hour a sudden increase of about 100 mV was observed (Figure 5.10). Afterwards the potential decreased slowly again.

The Raman spectra taken at the red points marked in the microscopic picture in Figure 5.9 are shown in Figure 5.10. The points were set at areas with different bulk composition. The Raman spectra show four different peaks which can be, according to Bernard [19–21] and Le Goff [22], assigned to $ZnOH_2$, ZnO and $ZnCO_3$.

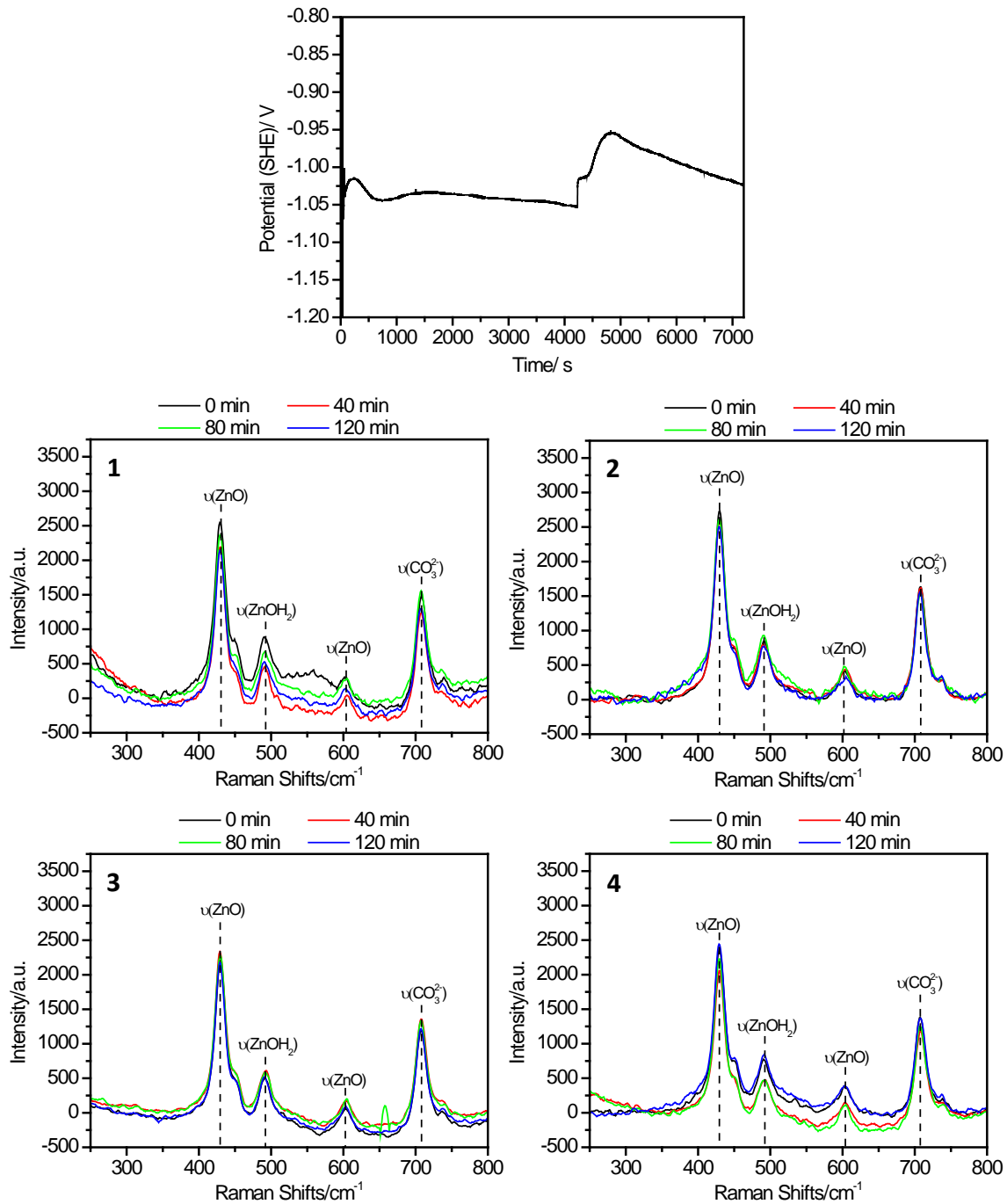


Figure 5.10: Top: Open circuit potential taken during the experiment. Raman spectra at 0, 40, 80 and 120 min related to the exposure to 0.05 M NaCl and 0.5 ml/min flow at pH 11.

5.4 Conclusions

The SEM pictures clearly demonstrated the complex microstructure composed of Zn, Zn–Mg and Zn–Al phases. The in-situ corrosion analysis in 0.05 M sodium chloride solution showed

that the corrosion started at several points on the surface and as main corrosion product ZnO was observed. Further these starting points acted as initiator from where the corrosion products grew over the surface with time. Additionally an increase of the pH was observed which stabilized the formed zinc oxide. The Raman spectra of the pH dependent measurements showed different composition of the oxide layer after exposure to the electrolyte. In the case of pH 3 and 7 the dissolution and oxidation of zinc were in equilibrium therefore the OCP stayed constant during the exposure. At pH 11 the amount was slowly increasing at all points.

6 In-situ corrosion analysis of oxide covered iron/ zinc alloy cut edges

The initial corrosion of oxide covered iron/ zinc substrates and iron/ zinc magnesium cut edges was investigated in neutral 0.05 M sodium chloride by means of Raman spectroscopy. To prevent pH changes of the corrosive solution during the measurement due to the oxygen reduction the experiments were performed under a high electrolyte flow. The Raman spectra showed a slow corrosion process on the zinc alloy coating and no corrosion process was observed on the iron side.

6.1 Experimental

6.1.1 Materials and sample preparation

If not indicated otherwise, all chemicals were of p.a. grade (pro analysis) and were used as supplied without any further purification. As substrates hot-dip galvanized steel sheets (ZM) were used as samples of technical interest. The interstitial free Z and ZM (sheet thickness 0.85 mm) were supplied by voestalpine Stahl GmbH (Linz, Austria) in the non skin passed state, i.e. without being temper rolled after application of the zinc coating. The thickness of the zinc coatings (alloy composition: (Z) Zn + 0.05% Al; (ZM) Zn + 2% Al + 2% Mg) after hot dip galvanizing were 7.5 μm . Samples were cut from the supplied material in 10 by 10 mm² samples and cleaned in three different solvents in an ultra-sonic bath for 20 min to ensure complete removal of any oils or surface contaminations. As solvents tetrahydrofuran (THF), iso-propanol and ethanol with analytical grade (Merck KGaA, Darmstadt, Germany) were used. After every solvent treatment the samples were dried under flow of dry nitrogen. The samples were measured in cut edge geometry.

6.1.2 Surface Analysis

Prior to the in-situ corrosion test the surface morphology and chemistry was analyzed by means of SEM and EDX. Focus ion beam (FIB) cross sectioning was prepared with LEO

1550VP. The cut was milled with a current of 1nA. Morphological characterization and surface composition was verified by means of a SEM with a field emission gun (LEO 1550VP) combined with an energy-dispersive x-ray spectroscopy (EDX) unit (Oxford Instruments). The measurements were performed at an accelerating voltage of 20 kV and a working distance of 8 mm, which results in a penetration depth of electrons higher than 1 μm .

6.1.3 In-situ Raman spectroscopy

The corrosion products were analyzed during the corrosion process by means of a confocal Raman microscope. The Raman spectra were obtained using a InVia Renishaw confocal Raman microprobe system (Renishaw plc, UK) equipped with an Leica DM 2500 M confocal microscope and an air cooled HeNe laser ($\lambda = 632.8 \text{ nm}$). Measurements were performed using a HCX APO L63x immersion objective for water with a numerical aperture of 0.9 and a 1800 grooves/mm diffraction grating. The laser power was set to 17.5 mW and an exposure time of 15 s. A scheme of the setup is shown in Figure 4.1. The flow through cell is equipped with a three electrode setup to measure also the potential during the corrosion process. The samples were exposed 0.05 M NaCl solution and the time dependent Raman maps were taken in intervals of 30 min. The Raman maps were obtained in streamline mode, instead of a point the laser is enlarged to a line. This allows a faster scan of larger areas. Prior to the Raman measurements microscopic pictures were taken.

6.2 Cut edge morphology and chemistry

The cross section of the zinc coated steel prepared by means of focus ion beam technique is shown in Figure 6.1. On the surface a low concentration of iron is observed but a high concentration of aluminum.

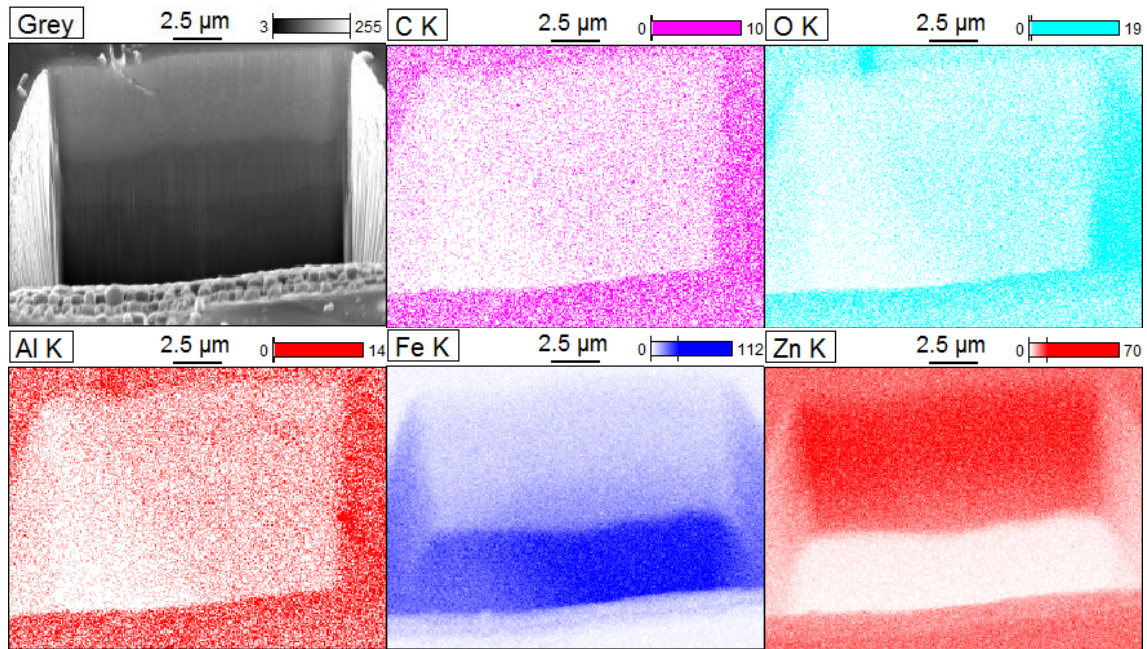


Figure 6.1: SEM analysis (top, left) and EDX mappings of the cross section prepared by FIB of zinc coated steel substrate. EDX mappings of local C, O, Al, Fe and Zn content.

In Figure 6.2 the cross section of zinc magnesium coated steel is shown. The zinc magnesium coating has a complex micro-structure composed of several phases. It was shown by Arndt et al [185] that the topmost surface is covered by a smooth, homogenous oxide layer consisting of a mixture of magnesium oxide and aluminum oxide, exhibiting a higher amount of magnesium than aluminum and a total thickness of 4.5 to 5 nm. Arndt et al [185] performed Auger element mappings on zinc magnesium alloy coated steel and observed that the bulk coating is composed of zinc dendrites and of binary eutectic Zn_2Mg-Zn . Near the interface steel/ alloy coating a ternary eutectic phase was found which consists of $Zn_2Mg-Zn-Al$.

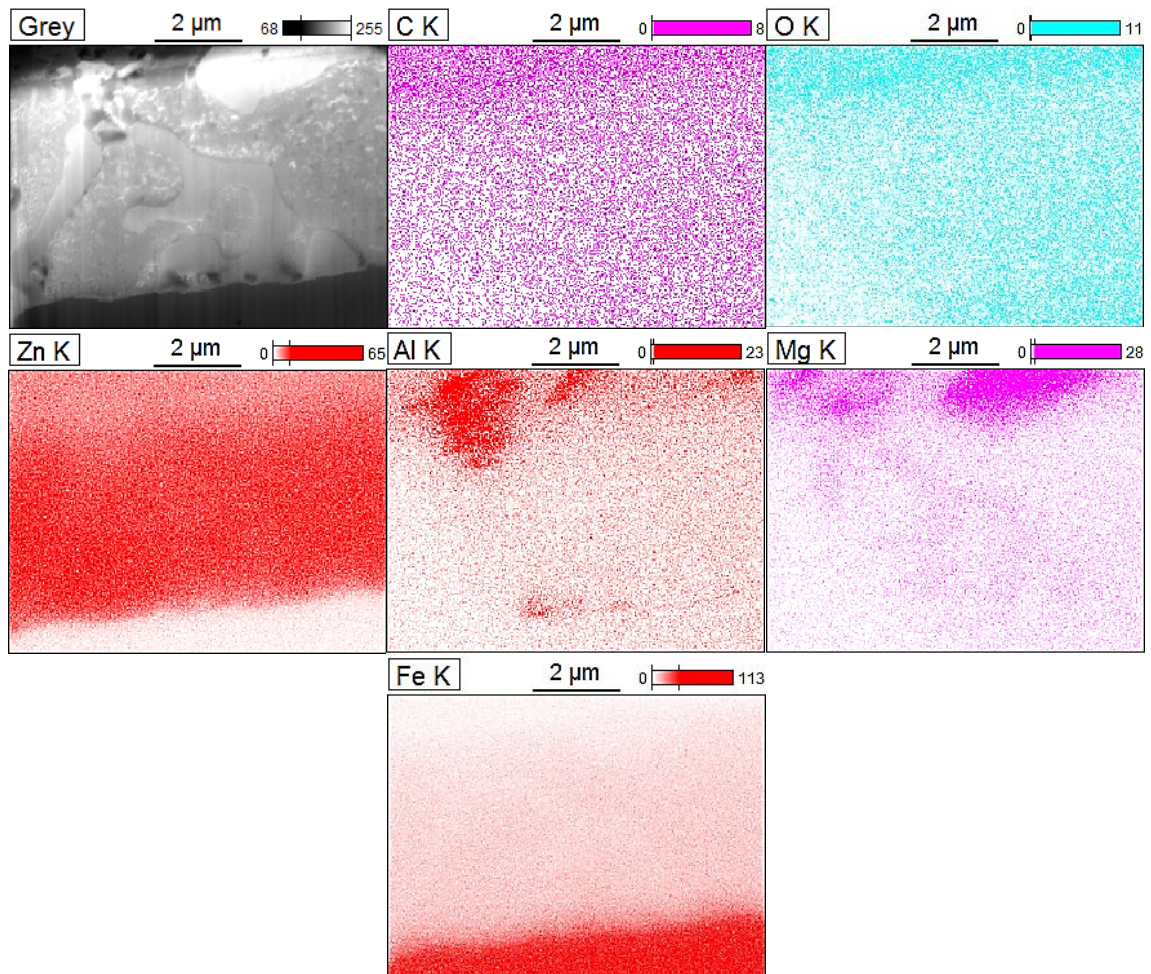


Figure 6.2: SEM analysis (top, left) and EDX mappings of the cross section prepared by FIB of zinc magnesium coated steel substrate. EDX mappings of local C, O, Zn, Al, Mg and Fe content.

6.3 Corrosion process and mechanism

The in-situ corrosion process was studied in neutral 0.05 M NaCl solution and with 0.5 ml/min electrolyte flow. During the corrosion process the open circuit potential was monitored and every 30 min Raman measurements were performed. In Figure 6.3 the microscopic images of zinc/iron cut edge geometry are shown. The sample was exposed 120 min to the electrolyte.

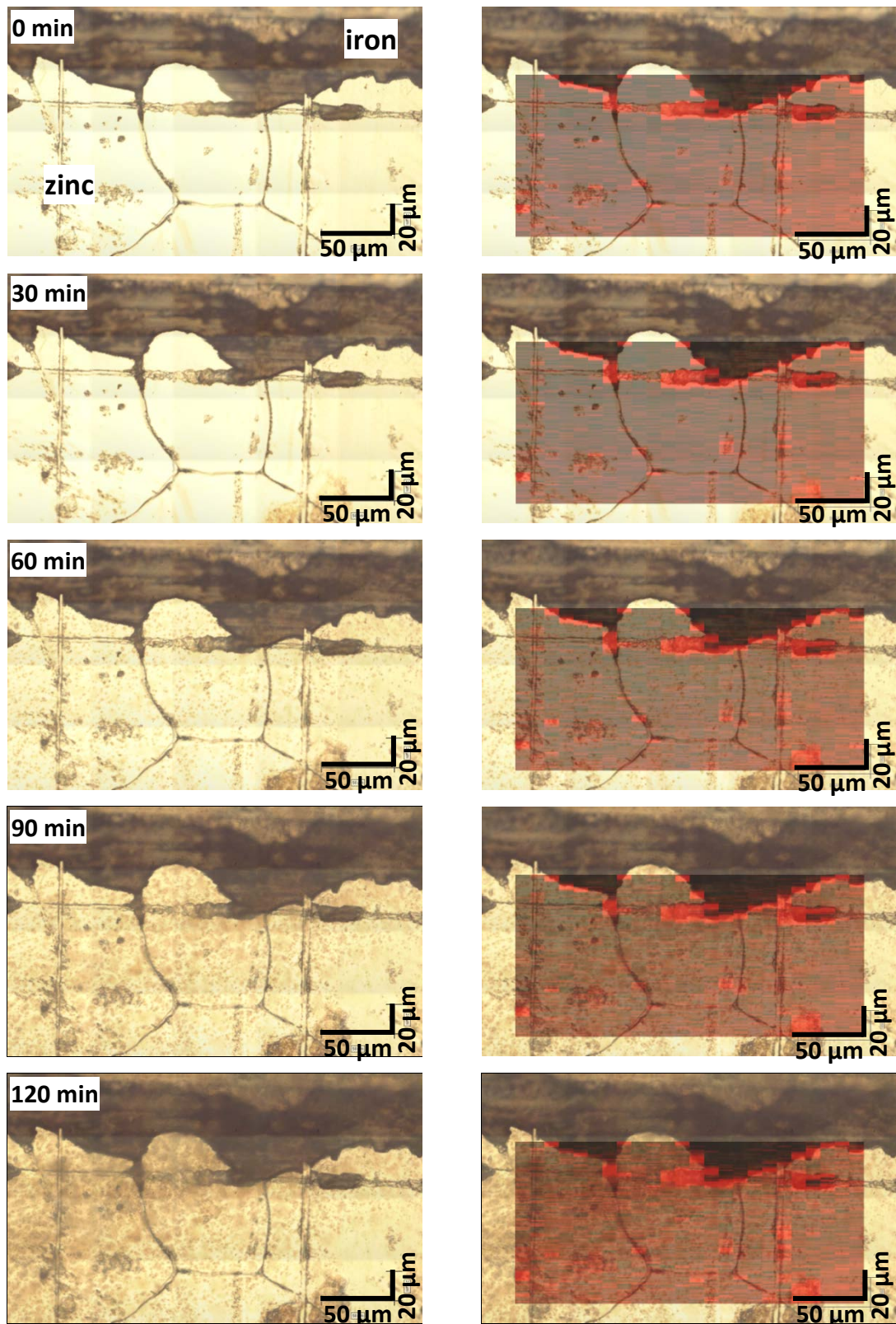


Figure 6.3: Microscopic images of Zn–Al/ Fe interface at 0, 30,60, 90 and 120 min related to exposure to 0.05 M NaCl and 0.5 ml/min flow. Left column: microscopic images. Right column: Raman images at 430 cm^{-1} .

In the microscopic images no significant change on the iron side was observed during the exposure to electrolyte. Due to the cathodic protection of zinc in present of iron zinc is corroding. In Figure 6.3 the Raman mappings of the zinc oxide vibration at 430 cm^{-1} are shown and an increase of zinc oxide is observed on the surface. A comparison of the time dependent Raman spectra is shown in Figure 6.4. The Raman spectra showed three different peaks which can be, according to Bernard [19–21] and Le Goff [22], assigned to ZnOH_2 , ZnO and ZnCO_3 . As main corrosion product ZnO and ZnCO_3 are observed.

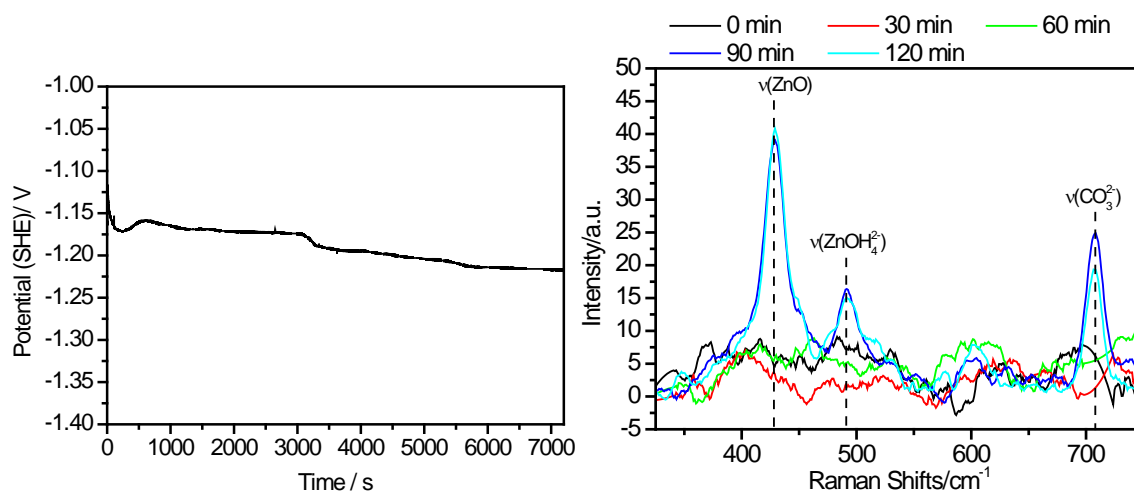


Figure 6.4: Left: Open circuit potential of the iron/zinc cut edge measured during the experiment. Right: Comparison of the Raman spectra of the zinc surface at 0, 30, 60, 90 and 120 min related to the exposure to 0.05 M NaCl at pH7.

The potential recorded during the measurement started at $-1.15\text{ V}_{\text{SHE}}$ and showed a minute decrease during the exposure of around 50 mV (Figure 6.4) which could be due to the formation of corrosion products on the zinc surface.

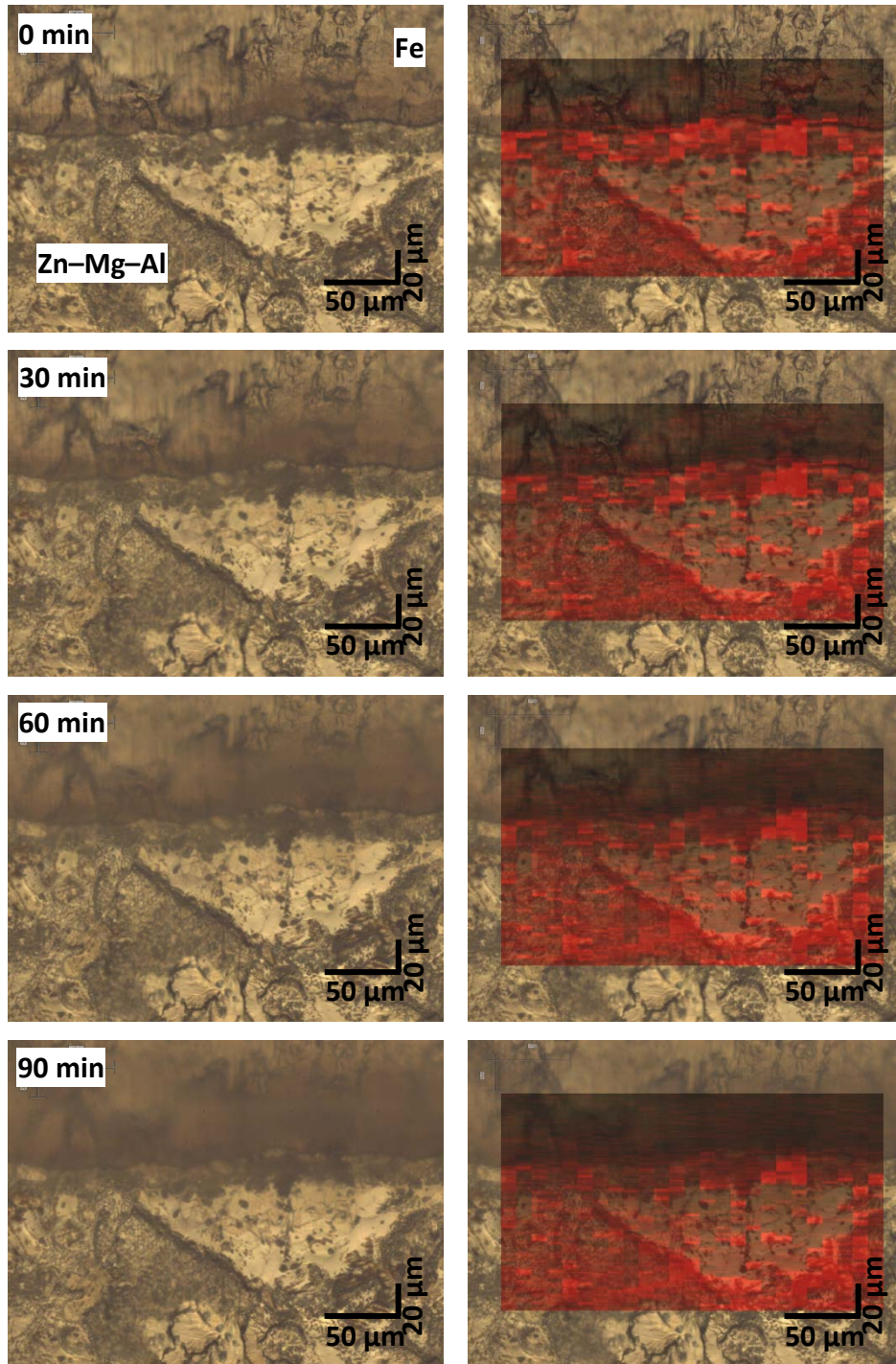


Figure 6.5: Images of Zn-Mg-Al/Fe interface at 0, 30, 60 and 90 min related to exposure to 0.05 M NaCl and 0.5 ml/min flow. Left column: Microscopic images. Right column: Raman images at 430 cm^{-1} .

The microscopic images are shown in Figure 6.5. A layer was built on the iron side during the exposure to electrolyte. In Figure 6.5 the Raman mappings of the zinc oxide vibration at 430 cm^{-1} are shown and no corrosion was observed on the zinc magnesium side. A comparison

of the time dependent Raman spectra is shown in Figure 6.6. The Raman spectra showed two small peaks which can be, according to Bernard [19–21] and Le Goff [22], assigned to ZnO and ZnCO₃.

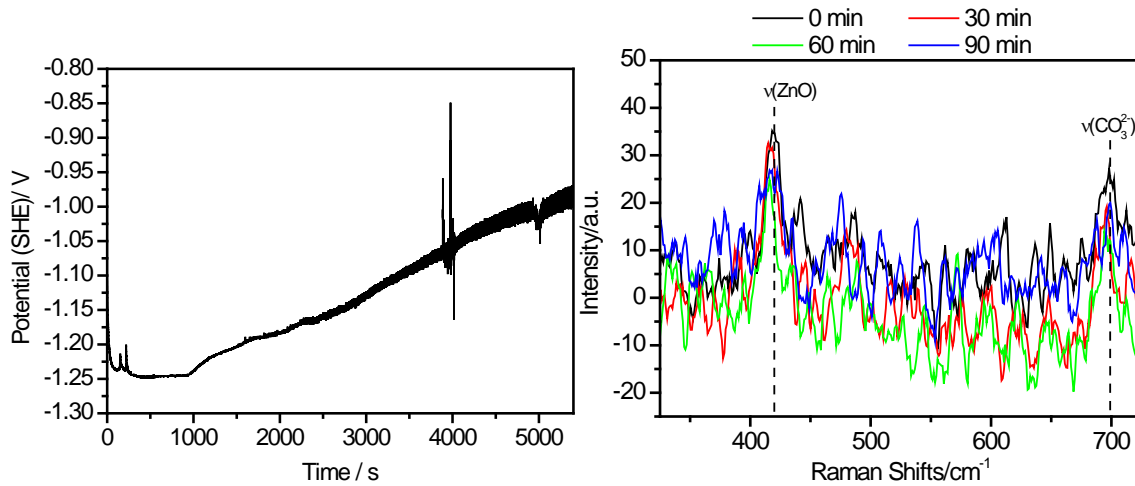


Figure 6.6: Left: Open circuit potential of the iron/zinc magnesium cut edge measured during the experiment. Right: Comparison of the Raman spectra of the zinc surface at 0, 30, 60 and 90 min related to the exposure to 0.05 M NaCl at pH7.

The potential recorded during the measurement started at $-1.23 V_{SHE}$ and showed a significant increase during the exposure of around 300 mV (Figure 6.6) which could be due to the precipitation of salts on the iron surface.

6.4 Conclusions

The in-situ corrosion analysis performed in 0.05 M sodium chloride solution and 0.5 ml/ min flow rate on Zn–Al/Fe and Zn–Mg–Al/Fe interfaces showed to protect the iron. On the zinc/iron surface zinc oxide was mainly formed on the zinc surface. In comparison to this Zn–Mg–Al/ Fe cut edge showed a dissolution of ions which were then precipitated on the iron surface.

7 Adsorption and stability of self-assembled organophosphonic acid monolayers on plasma modified Zn–Mg–Al alloy surfaces¹

The adsorption and stability of adhesion promoting organophosphonic acid monolayers on plasma modified Zn–Mg–Al alloy surfaces were investigated by means of microscopic and spectroscopic techniques. A strip hollow cathode (SHC) was chosen for the plasma surface modification. The chemical composition of the plasma treated surfaces and the influence of reducing and oxidizing plasma modifications on the corrosion properties of Zn–Mg–Al alloy surfaces were analyzed by means of X-ray photoelectron spectroscopy (XPS) and cyclic voltammetry, respectively. The adsorption and stability of phosphonic acid monolayers were comparatively studied on plasma modified and non-plasma modified Zn–Mg–Al alloy surfaces. Self-organization of monofunctional monolayers was confirmed by means of polarization modulated infrared reflection absorption spectroscopy (PM-IRRAS) and XPS. Contact angle measurements were performed to prove the stability of the octadecylphosphonic acid (ODPA) monolayer on the native and different plasma treated surfaces in aqueous media. Plasma modification and ODPA adsorption resulted in a synergistic inhibition of the redox current densities of the alloy surface. The strongest inhibition was observed for an Ar/H₂ plasma + O₂ plasma treatment followed by octadecylphosphonic acid self-assembled monolayer adsorption.

7.1 Experimental

7.1.1 Materials and Sample Preparation

If not indicated otherwise, all chemicals were of p.a. grade (pro analysis) and were used as supplied without any further purification. ODPA was provided by Alfa Aesar and Ethanol by Merck, Germany. For the studies presented here bulk Zn–Mg–Al alloy samples were prepared by melting and casting the raw materials containing 98 wt.% Zn, 1 wt.% Mg and 1 wt.% Al. Samples were cut into disks with a diameter of 30 mm, grinded, polished with

¹ The content of this chapter is adopted from publication [187].

diamond paste of a particle radius of 3 μm and subsequently cleaned in isopropanol for 10 min in an ultrasonic bath and dried in a stream of nitrogen.

7.1.2 Plasma Surface Chemistry

The experimental setup for the plasma modification is based on the so called strip hollow cathode (SHC) method. Basically it consists of two grounded plane parallel metal sheets and a gas channel at the bottom between the sheets as the anode. The sample is mounted on one of the metal sheets. The base pressure of the SHC–setup containing chamber before the inlet of working gases was in the range of 10^{-4} mbar. The gas flows for the according plasma modifications were adjusted to 200 sccm argon, 400 sccm hydrogen and 100 sccm oxygen. Pure gases were used for the experiments, argon and hydrogen with a purity of 99.999% and oxygen with a purity of 99.995% (Linde AG). All plasma treatments were adjusted to 60 s. To create a hollow cathode glow discharge a pulsed DC generator Pinnacle™ Plus (Advanced Energy) was used. For the plasma treatments shown in this paper the power was adjusted to 500 W (Ar/H₂) or 200 W (O₂). In all cases the DC feed–in was pulsed with a frequency of 200 kHz [188].

7.1.3 Adsorption and Self–Organization of Organic Acids

Octadecylphosphonic acid (ODPA, CH₃(CH₂)₁₇PO₃H₂) was used as the precursor molecule. ODPA was dissolved in ethanol with a concentration of 10^{-3} mol/l. The total solution volume in the beaker was 50 ml for each surface preparation. Substrates were immersed into the ODPA solution for 24 h. After rinsing with ethanol the samples were dried in a stream of nitrogen.

7.1.4 Surface Analysis

To investigate the interfacial binding of the adsorbed molecules on the modified Zn–Mg–Al surface, modified surfaces were analyzed via polarization modulated infrared reflection absorption spectroscopy (PM–IRRAS). A Bruker Vertex 70 spectrometer in combination with

a PMA 50 unit for polarization modulation was employed. The infrared beam is guided through the setup by gold coated mirrors, polarized by a ZnSe crystal and reflected at the sample under 80° to the surface normal to a liquid nitrogen cooled mercury cadmium telluride (MCT) detector. The spectra were recorded using a resolution of 4 cm^{-1} and originate from averaging over 1024 single scans.

Complementary X-ray photoelectron spectroscopy (XPS, Quantum 2000, Physical Instruments, USA) was performed, using a monochromated Al $K\alpha$ X-ray source with a spot diameter of $100\ \mu\text{m}$. The take-off angle of the detected photoelectrons was 45° to the surface normal. All spectra were calibrated using the C1s peak (binding energy, $BE=285\text{ eV}$) as internal reference. For a detailed analysis of the components of the measured XPS signals, e.g. the hydroxide to oxide ratio, an appropriate peak fitting was applied [189].

The hydrophilic and hydrophobic properties of the studied materials surfaces were studied by means of static water contact angles according to the sessile drop method (OCA 20, Data Physics) before and after a repeated immersion of the samples in ultra clean water for a time period of 10 min. A drop with a volume of $5\ \mu\text{L}$ was set onto the surface of the sample by means of a syringe. A picture of the drop was taken by a CCD camera. The volume and the static contact angle of the water drop were calculated by an analysis program (SCA 20, Data Physics). The static contact angles of water were measured and plotted as a function of immersion cycles for all studied surfaces.

Cyclic voltammetry was performed on bare and plasma treated samples with and without adsorbed ODPa monolayers to investigate their effect on the redox currents. A Gamry potentiostat with a Gamry ECM8 Multiplexer was used. Prior to the cyclic voltammetry (CV) measurements, the samples were kept for 10 s at OCP. The CV curves were taken in a potential range from $-1150\text{ mV}_{\text{SHE}}$ to $-750\text{ mV}_{\text{SHE}}$ with a sweep rate of 100 mV/s . The starting potential was set to $-800\text{ mV}_{\text{SHE}}$ and four sweeps were measured with an upper and lower potential limit of $-750\text{ mV}_{\text{SHE}}$ and $-1150\text{ mV}_{\text{SHE}}$, respectively. For the comparison of different surface treatments the fourth sweep was plotted. The samples were fixed in a home-made cell with a measuring spot diameter of 1 cm . As electrolyte, borate buffer solution ($0.2\text{ M H}_3\text{BO}_3 + 0.05\text{ M Na}_2\text{SO}_4 + 0.05\text{ M Na}_2\text{B}_4\text{O}_7$) at room temperature was used. The reference electrode was a saturated Ag/AgCl electrode (Radiometer Analytical SAS, France).

7.2 Plasma surface chemistry

The native and the plasma treated samples were analyzed by means of XPS and cyclic voltammetry to study the influence of the plasma modification on the electrochemical surface properties. Zn–Mg–Al alloy samples were first treated with reductive Ar/H₂ plasma for duration of 60 s to receive an oxide surface free of carbon contaminations with reduced film thickness in comparison to the native oxide film. In the next step an O₂ plasma was performed to increase the thickness of the native oxide film via a plasma oxidation process.

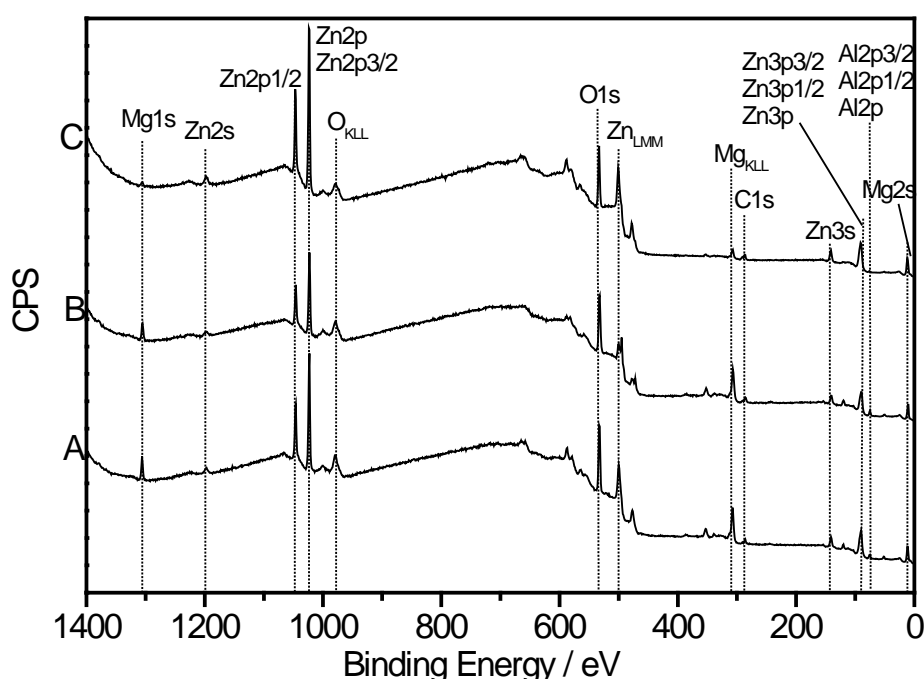


Figure 7.1: XPS survey spectra of polished (A), Ar/H₂ plasma (B) and Ar/H₂ + O₂ plasma treated Zn–Mg–Al surfaces.

Chemical composition of the native and plasma treated oxide films were analyzed by means of XPS. The corresponding survey spectra are shown in Figure 7.1. Both the polished Zn–Mg–Al surface and the plasma treated surfaces showed XPS peaks of oxygen, carbon, zinc, aluminum and magnesium.

Table 7.1: Atomic composition (at%) as analyzed by XPS for a polished, Ar-plasma reduced and plasma oxidized Zn-Mg-Al alloy.

		Polished						Ar/H ₂ plasma						Ar/H ₂ ⁻ + O ₂ plasma					
		Peak Position/eV	FWHM	Peak%	at%	Peak Position/eV	FWHM	Peak%	at%	Peak Position/eV	FWHM	Peak%	at%	Peak Position/eV	FWHM	Peak%	at%		
Mg 2p	Mg(OH) ₂	50.2	2.2	100	1.9	50.3	2.8	100.0	4.5	50.6	2.1	100.0	4.6						
Al 2p	Al ₂ O ₃	74.2	1.8	100	2.6	74.5	2.3	100.0	13.9	74.3	1.9	100.0	9.3						
C 1s	C-H / C-C	285.0	1.8	60.4		285.0	2.3	75.8		285.0	1.9	71.8							
	C-OH	286.5	1.8	4.2	16.0	286.6	2.3	0.0	14.1	286.6	1.9	0.8	10.6						
	C-OOH	288.4	1.8	2.3		288.4	2.3	0.0		288.5	1.9	7.0							
	CO ₃ ²⁻	289.7	1.8	33.1		290.1	2.3	24.2		290.0	1.9	20.4							
O 1s	O ²⁻	530.5	2.0	28.0		530.6	2.0	31.7		530.8	2.0	59.3							
	OH ⁻	532.0	2.0	72.0	45.8	532.1	2.0	68.3	51.0	532.3	2.0	40.7	53.6						
Zn 2p _{3/2}	ZnO	1022.1	2.0	100	33.8	1022.2	2.6	100.0	16.5	1022.2	2.0	100.0	21.9						

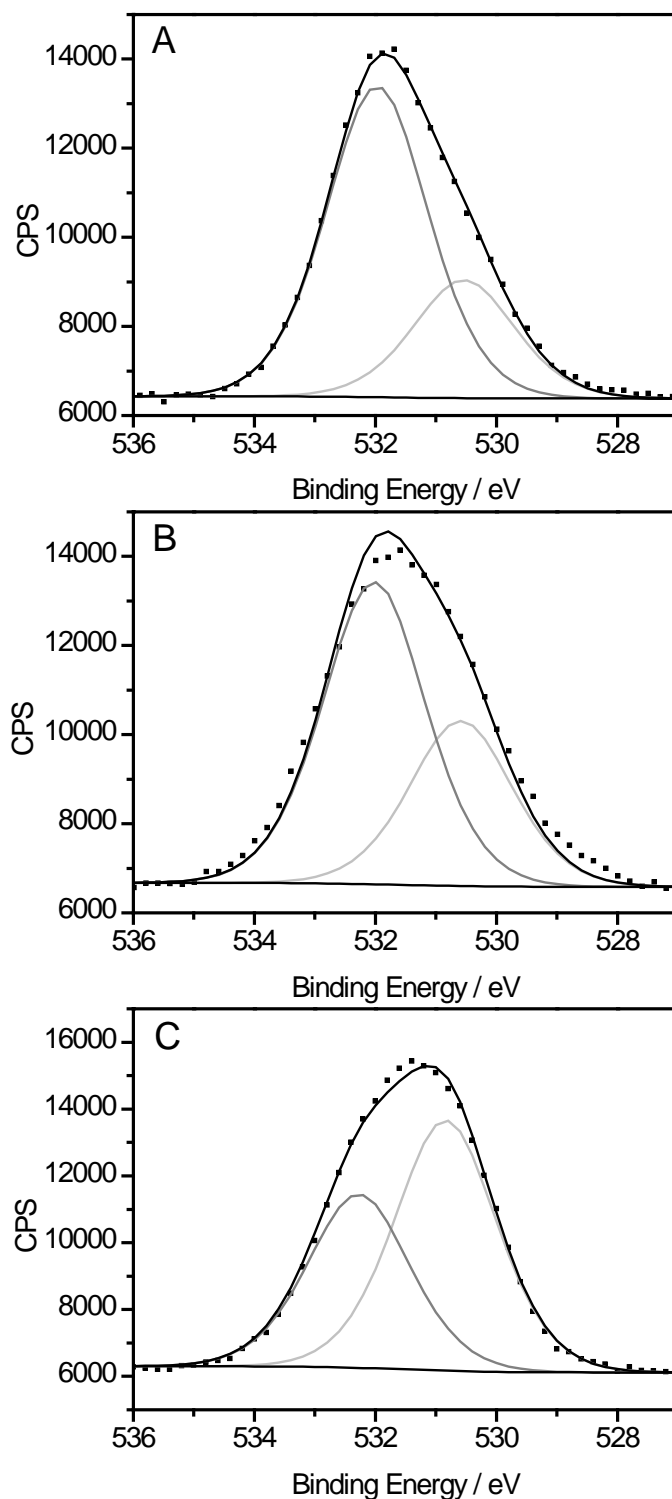


Figure 7.2: O1s detail spectra of (A) a polished Zn–Mg–Al alloy surface, (B) a 60 s Ar/H₂ plasma modified Zn–Mg–Al alloy surface and (C) a subsequent 60 s O₂ plasma modified Zn–Mg–Al alloy surface.

The overall composition and changes in oxide composition due to the reductive and oxidative plasma treatments of the surfaces are given in Table 7.1. The given uncertainty of

the measurements of 0.5 at.% results from an estimation given for the equipment by the manufacturer. Furthermore, the measured high resolution spectra were fitted by peaks of possible oxidation states for each element as listed in column three of the table. Additionally, the fitting parameters, BE and full width at half maximum (FWHM) are given in columns four and five. The relative percentage of different oxidation states of each element, obtained from the fitting procedure are also presented in Table 7.1.

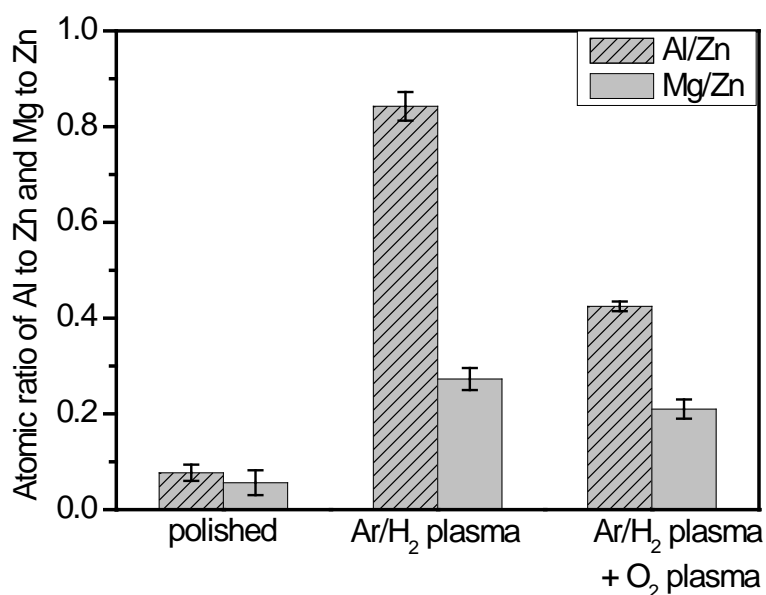


Figure 7.3: Atomic ratio of Al/Zn and Mg/Zn as a function of the surface condition.

The dominant species of the polished Zn–Mg–Al surface are oxygen with 45.8 at.% and zinc with 33.8 at.%. The O1s signal consists of two components, which were fitted by symmetrical profiles with a resulting FWHM of 2.0 eV and a chemical shift of 1.5 eV (Figure 7.2). A BE of 530.5 eV results from the O²⁻ oxidation state of oxygen in the oxide bond, while the component at 532.0 eV consists of the contributions from surface hydroxides and oxygen containing organic adsorbates on the surface. The chemical composition of these organic adsorbates was identified by the components of the C1s signal in Table 7.1. Small content of magnesium and aluminum species was found which is also as listed in Table 7.1, the surface concentrations of Mg and Al were 1.9 and 2.6 at.% respectively, which means that both elements are already enriched within the surface oxide film after the polishing step due to atmospheric oxidation.

Corresponding XPS measurements were performed on the Ar/H₂ modified samples as well and a list of measured elements with the corresponding chemical composition, the BE of the identified components with the FWHM value and the corresponding percentage are summarized in Table 7.1. In comparison to the native oxide film the Ar/H₂ plasma treatment led to a significant reduction of the carbon contamination. The O1s signal ratio of OH⁻ to O²⁻ did not change significantly between the Ar/H₂ plasma modified and the native surface film (Figure 7.2). However, the surface aluminum concentration significantly increased to 13.9 at.% and the surface magnesium concentration to 4.5 at.% as a result of the reductive treatment. The relative enrichment of Al and Mg in comparison to Zn in the surface oxide layer indicates a selective oxidation of Al and Mg during the Ar/H₂ plasma treatment which is solely able to reduce zinc oxides to zinc due to the higher redox potential of Zn/Zn²⁺. The low residual oxygen partial pressure during the low pressure plasma treatment leads to the selective oxidation of Al and Mg and thereby to an enrichment of these elements in the surface oxide which is demonstrated in Figure 7.3. The Mg enrichment in the outermost oxide layer after Ar/H₂ plasma was also observed by Giza and Grundmeier for Zn₂Mg substrates [55].

The comparison of the Zn LMM peak before and after Ar/H₂ plasma modification (see Figure 7.4A,B) illustrates that the contribution of metallic zinc is increased after the reducing plasma step even after the exposure to a normal lab atmosphere during transport to the XPS analysis chamber (exposure time to air: about 5 min). The authors assume that the reduced overall oxide film thickness is due to the partial reduction of the zinc oxide film in the reducing plasma and the enrichment of Mg and Al oxides which then act as a barrier film during the temporary exposure to lab atmosphere.

After the subsequent O₂ plasma modification the carbon contamination decreased even further in comparison to the reduced state. Moreover, the oxidative step led to an increase in the ZnO content of the oxide film as illustrated by the change in the ratios of the alloy components in the oxide film (see Figure 7.3). However, the Al and Mg surface concentrations remained still significantly higher than for the native oxide film.

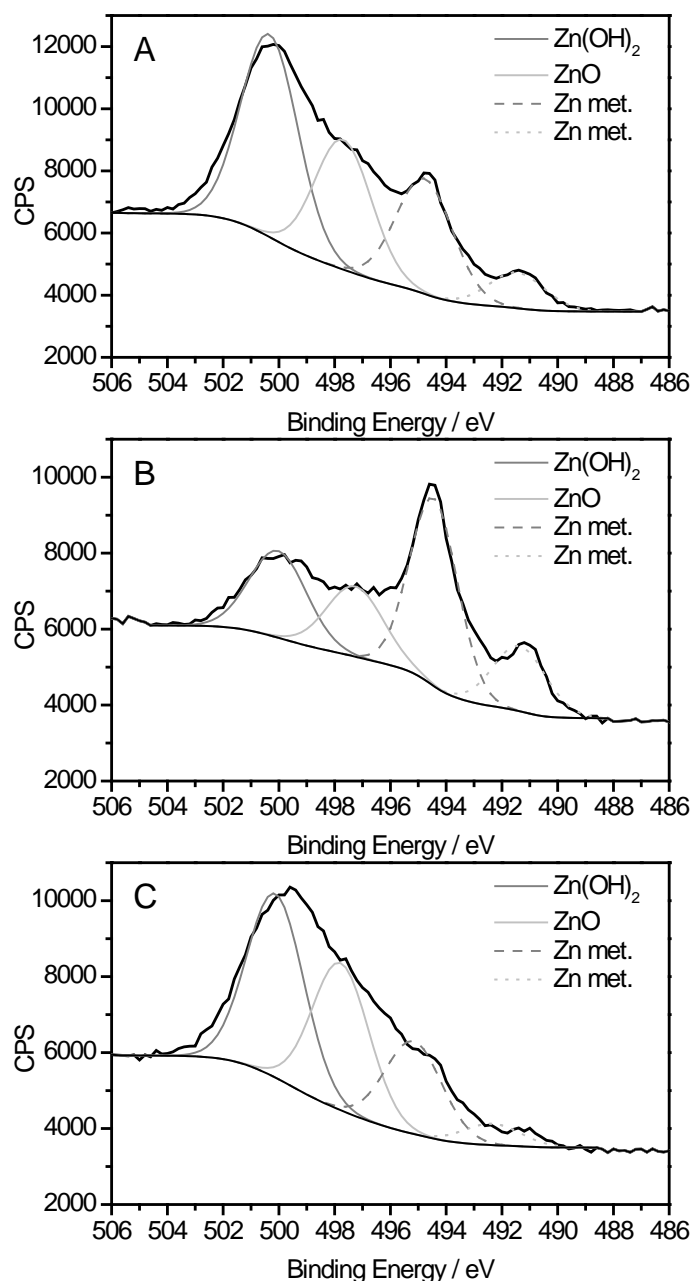


Figure 7.4: ZnLMM detail spectra of (A) a polished Zn–Mg–Al alloy surface, (B) a 60 s Ar/H₂ plasma modified Zn–Mg–Al alloy surface and (C) a subsequent 60 s O₂ plasma modified Zn–Mg–Al alloy surface.

As a consequence of the oxygen plasma treatment, the OH⁻ /O²⁻ ratio was significantly reduced. In comparison to the Ar/H₂ plasma, the absence of hydrogen in the oxygen rich plasma gas causes the surface hydroxyls to oxidize.

The content of metallic zinc in the Zn LMM peak in Figure 7.4C decreases in comparison to the solely Ar/H₂ plasma treated sample. From these results it can be deduced that the O₂

plasma modification led to the increase of the oxide film thickness. This was also observed for Zn₂Mg substrates by Giza and Grundmeier [55].

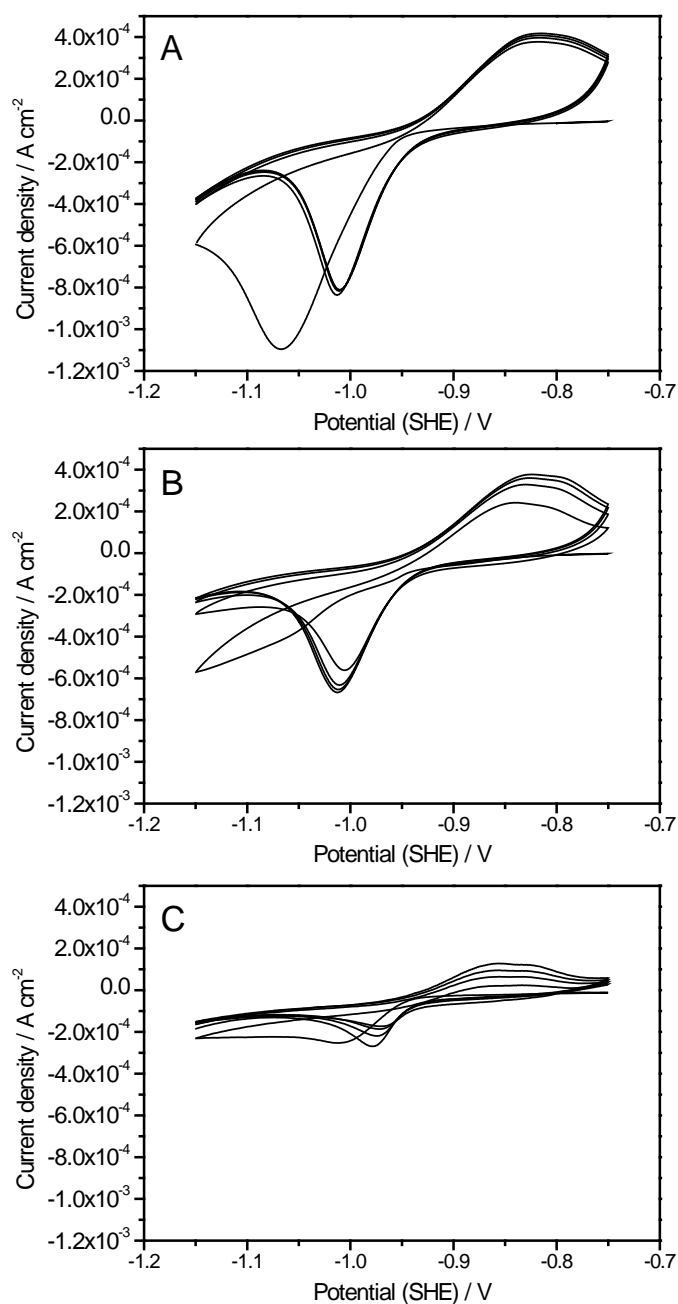


Figure 7.5: Cyclic voltammograms measured in borate buffer of a polished Zn–Mg–Al alloy surface (A), after 60 s Ar/H₂ plasma modification (B) and after subsequent 60 s O₂ plasma modification (C).

Figure 7.5 shows the cyclic voltammograms (CVs) of a polished and two plasma modified surfaces. The CVs were measured in the range often used for zinc and Zn–Al alloys from

–0.75 to –1.15 V_{SHE} [1; 190]. Dafydd et al. suggested that the anodic current peak received on Zn–Al alloys in this potential range completely originate from the oxidation of zinc species and that aluminum does not take part in the oxidation process [34]. Hausbrand showed that the potentials of reduction and oxidation of $ZnMg_2$ are consistent with the redox potentials of zinc [42].

The voltammograms of the polished (Figure 7.5A) and the Ar/ H_2 plasma treated (Figure 7.5B) samples show an anodic peak at approximately –0.81 V_{SHE} which can be assigned to formation of hydroxide and oxide and the corresponding cathodic peak at about –1.0 V_{SHE} which can be related to oxygen reduction of dissolved oxygen. The anodic peak of the subsequently O_2 plasma treated surface lies at –0.84 V_{SHE} and the corresponding cathodic peak at –0.98 V_{SHE} . In Figure 7.5A the just polished sample showed constant high current densities for all four CVs. The reductive plasma treated (Figure 7.5B) and the subsequent O_2 plasma treated samples (Figure 7.5C) showed a slight increase of the current densities during the four cycles.

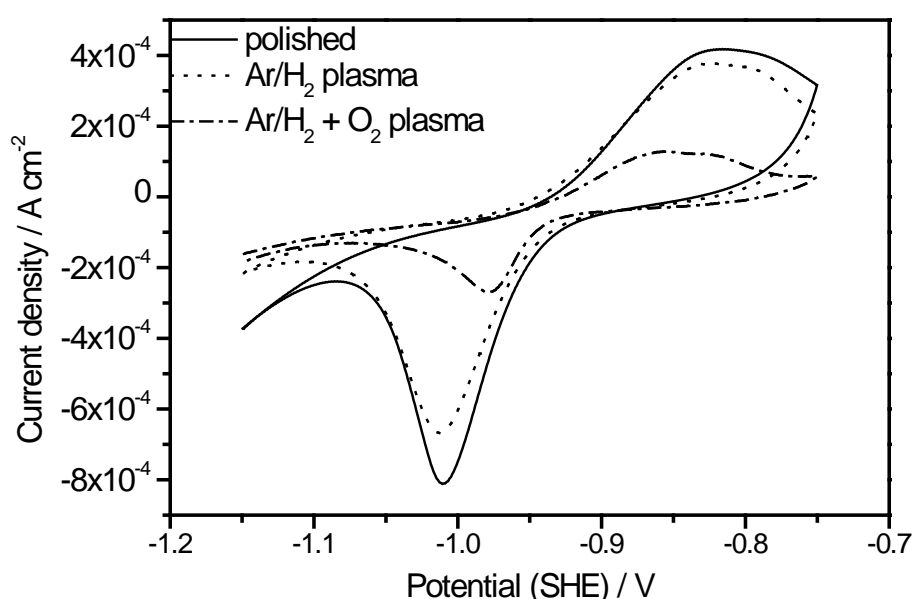


Figure 7.6: Comparison of the last cyclic voltammogram measured in borate buffer of a polished Zn–Mg–Al alloy surface (solid line), after 60 s Ar/ H_2 plasma modification (dotted line) and after subsequent 60 s O_2 plasma modification (dashed line).

The fourth scan of the polished and plasma treated samples is shown in Figure 7.6. Comparison of the anodic current density of the polished and Ar/ H_2 plasma treatment did

not show a significant difference (Figure 7.6). The Ar/H₂ plasma treatment has almost no effect on the redox activity of the surface. However, the subsequent O₂ plasma modification led to a significant reduction of the redox current densities. The decreasing current density of the cathodic peak from polished Zn–Mg–Al (-8×10^{-4} A cm⁻²) to Ar/H₂+O₂ plasma treated surfaces (-3×10^{-4} A cm⁻²) confirms the increase of the oxide film thickness and the reduction of the zinc concentration in the plasma treated oxide film.

7.3 Adsorption and self-organization of organic acids

The PM-IRRAS method was applied for the characterization of the adsorbed ODPA self-assembly monolayer on the native and plasma modified alloy surfaces. PM-IRRAS can be used to analyze mean orientation, packing density and interfacial bond formation of adsorbed molecules [106]. After deposition of the organic acids on the substrates, the interfacial bond formation can be determined by studying the appearance and the peak positions assigned to P=O and P–O vibrations [106].

The wavelength region of 2800 cm⁻¹ – 3000 cm⁻¹ of PM-IRRAS measurements in Figure 7.7A shows four prominent peaks assignable to the C–H stretching modes of CH₂ and CH₃ belonging to the aliphatic chains of ODPA. The PM-IRRAS data shown in Figure 7.7B indicate an absence of the peaks of the free acid group P–OH and P=O (1230 cm⁻¹). The absence of the free acid groups P–OH and P=O suggests that the adsorbed phosphonic acid functionality is deprotonated, which is consistent with the detected broad PO₃²⁻ stretching mode. Hence coordinative binding modes of the octadecylphosphonic acid at the oxide layer of the alloy can be assumed. Monodentate coordination is unlikely because the phosphonic acids appear to be completely deprotonated. A bidentate condensation is most likely according to the fundamental studies of Thissen et al. [106].

In all ODPA spectra the stretching mode of PO₃²⁻ appears in a broad peak at 1080 cm⁻¹. The peak at 950 cm⁻¹ is assigned to the Al–O–vibration [85].

The methylene stretching modes between 2900 and 3000 cm⁻¹ usually shift to lower frequencies with increasing conformational order of the alkyl chains [191–194]. It has been observed that an ordered aliphatic monolayer contains chains in an all-trans configuration is

characterized by a certain peak position of the methylene groups ($\nu(\text{CH}_2)_{\text{as}} < 2920 \text{ cm}^{-1}$ and ($\nu(\text{CH}_2)_{\text{s}} < 2850 \text{ cm}^{-1}$ for the IRRAS measurements [12; 92; 110; 195].

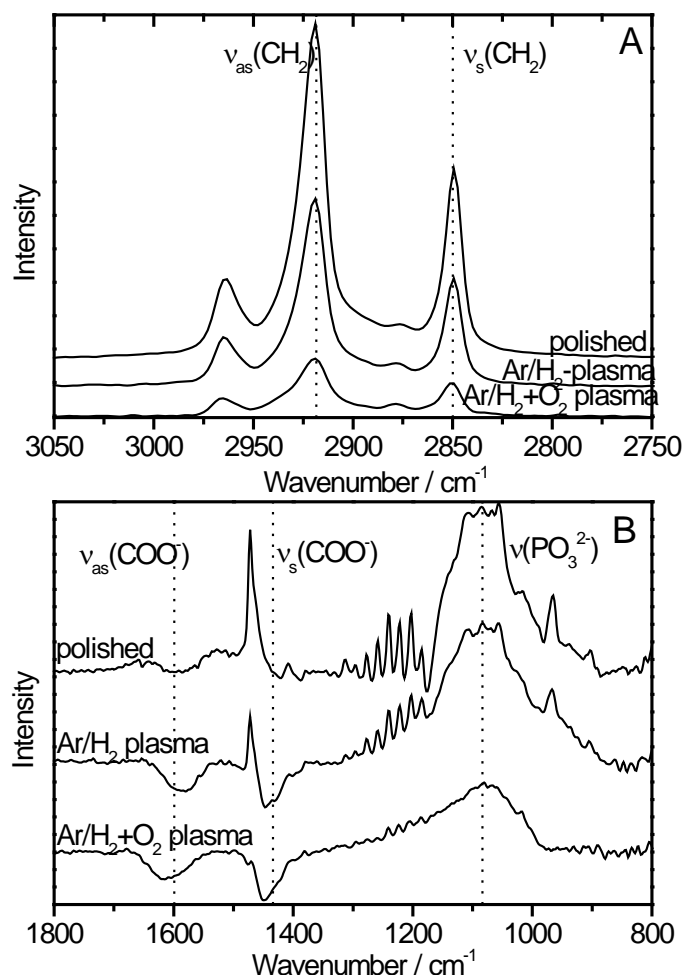


Figure 7.7: A and B: PM-IRRAS of Zn–Mg–Al alloy polished and after plasma modifications immersed in 10^{-3} mol/l ODP. All spectra are referenced to the surface spectra taken before ODP adsorption.

For the here studied surfaces the position of symmetric and asymmetric methylene group vibration was observed at 2918 cm^{-1} and 2849 cm^{-1} (see Figure 7.7A). This positions lead to the assumption that the ODP layers formed a well ordered monolayer for all studied substrates. Based on the ratio of the $\nu(\text{CH}_2)$ to $\nu(\text{CH}_3)$ peaks the averaged tilt angle of the aliphatic chains can be calculated according to Tillman et al. [112].

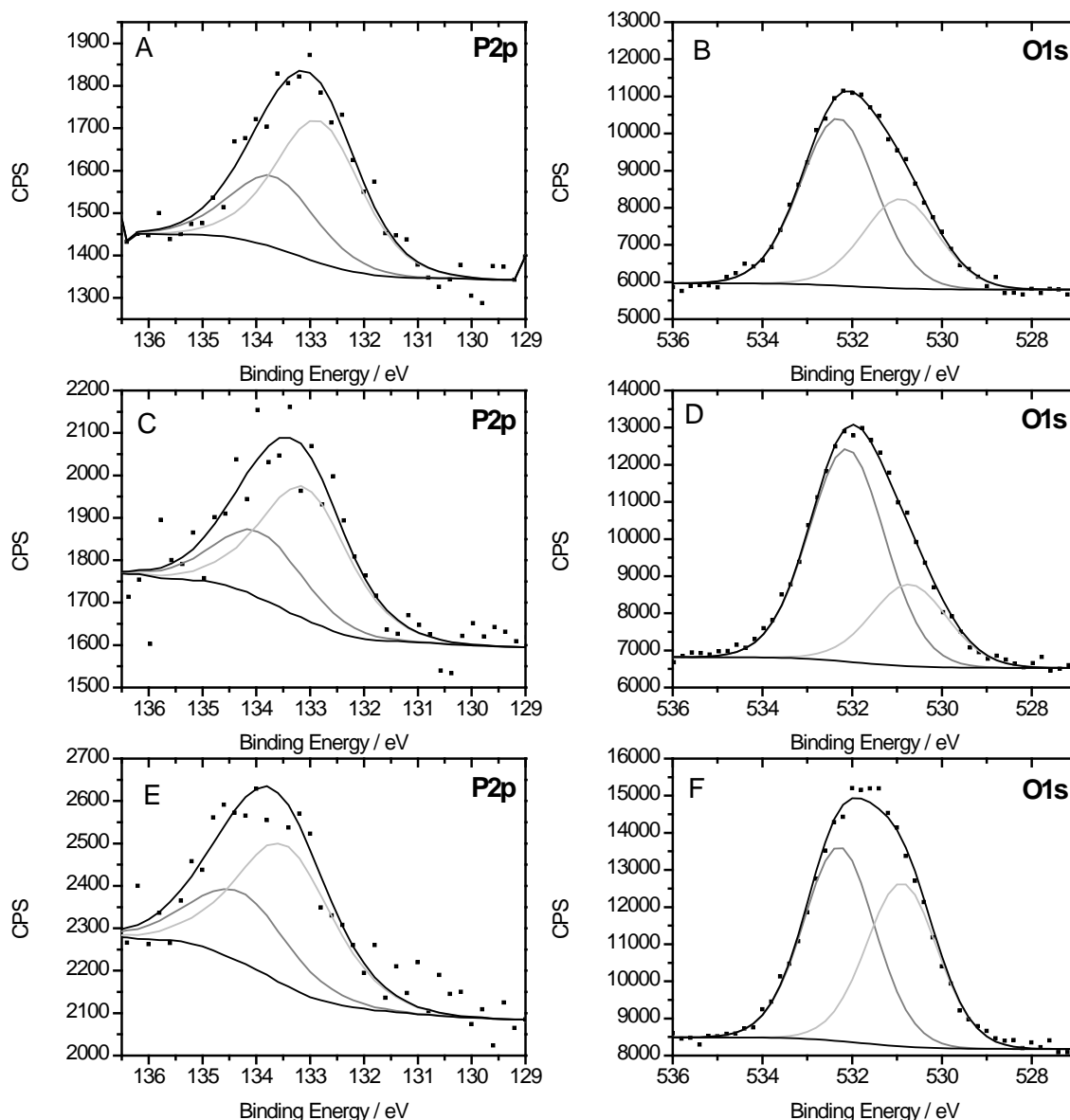


Figure 7.8: A, C and E: XPS P 2p detail spectra of Zn–Mg–Al alloy polished and after plasma modifications immersed in 10^{-3} mol/l ethanolic ODPA solution. B, D and F: XPS O 1 s spectra of samples pretreated as above and immersed in 10^{-3} mol/l ODPA. First row (A and B): samples were polished. Second row (C and D): samples were modified via Ar/H₂ plasma. Third row (E and F): samples were treated in O₂ plasma subsequently.

On the polished substrate the angle to the surface normal was 44° and with a reductive plasma as pretreatment an angle of 39° resulted. However, the ODPA adsorption on oxidative plasma treated Zn–Mg–Al surface showed an angle of 28°. Based on this assumption, it appears that the ordering of the phosphonic acid monolayers on Zn–Mg–Al alloys depend on the chemistry of the passive film. The highest order is seen on the ODPA

covered substrate after oxygen plasma. The higher $\nu(\text{CH}_2)$ peak intensities especially for the polished surface can at least partly be explained by the less up-right orientation of the aliphatic film. The intensities of the vibration peaks of CH_2 and CH_3 groups at 1470 cm^{-1} showed the same trend as the stretching vibrations with regard to the peak intensities. Based on the ex-situ measurements and the residual aliphatic contaminations on all surfaces a more detailed interpretation of these data could not be done for the here studied system.

The results of the XPS measurements of the Zn–Mg–Al surface after the adsorption of ODPA with the corresponding peak positions and atomic concentrations based on the curve fitting are listed in Table 7.2. The XPS O1s and P2p detail spectra of the Zn–Mg–Al surfaces after the adsorption of ODPA SAMs are shown in Figure 7.8.

The XPS analysis of the bare substrates in comparison to the ODPA covered substrates show a similar behavior. Both plasma treatments led to an increase of the surface aluminum and magnesium content. The O1s spectra for polished and Ar/H₂ plasma treated samples showed a higher content of OH^- in the outermost layer. For the Ar/H₂ and subsequently O₂ plasma treated surface the ratio of OH^- and O^{2-} is almost 1:1.

Table 7.2: Atomic composition (at%) of ODPA covered samples analyzed by XPS.

	Polished						Ar/H ₂ plasma						Ar/H ₂ ⁻ + O ₂ plasma					
	Peak Position /eV	FWHM	Peak%	at%	Peak Position /eV	FWHM	Peak%	at%	Peak Position /eV	FWHM	Peak%	at%	Peak Position /eV	FWHM	Peak%	at%		
Mg 2p	51.0	2.2	100.0	0.6	51.0	1.9	100.0	2.5	50.8	2.1	100.0	2.6	50.8	2.1	100.0	2.6		
Al 2p	75.1	1.8	100.0	1.6	74.7	1.9	100.0	3.9	74.7	1.8	100.0	5.0	74.7	1.8	100.0	5.0		
P2p _{3/2}	132.8	2.0	66.7	2.8	133.1	2.0	66.7	2.6	133.3	2.1	66.7	2.8	133.3	2.1	66.7	2.8		
P2p _{1/2}	133.7	2.0	33.3		134.0	2.0	33.3		134.2	2.1	33.3		134.2	2.1	33.3			
C 1s	284.0	1.5	55.6		284.0	1.4	25.8		283.8	1.4	13.5		283.8	1.4	13.5			
	285.0	1.5	38.4	64.8	285.0	1.4	72.3	55.8	285.0	1.4	83.4	51.2	285.0	1.4	83.4	51.2		
	286.4	1.5	6.0		286.2	1.4	1.9		286.2	1.4	3.1		286.2	1.4	3.1			
O 1s	530.9	2.0	34.4		530.7	2.0	27.7		530.9	1.9	48.0	30.9	530.9	1.9	48.0	30.9		
	532.3	2.0	65.6	23.6	532.1	2.0	72.3	28.7	532.3	1.9	52.0		532.3	1.9	52.0			
Zn 2p _{3/2}	1022.4	2.4	100.0	6.6	1022.3	2.4	100.0	6.6	1022.4	2.2	100.0	7.4	1022.4	2.2	100.0	7.4		

Prior to the adsorption of the phosphonic acid, no intensities of phosphorus species could be observed in the XP spectrum. The overall composition of the surface confirmed that ODPA could be irreversibly adsorbed on the Zn–Mg–Al surface. The maximum of the P2p peak was observed for binding energies between 133.8 and 134.2 eV. The FWHMs varied from 1.7 to 2.1 eV and the spectrum was significantly broadened towards higher binding energies (BE).

This effect is attributed to the P2p_{3/2}–P2p_{1/2} spin–orbit coupling [196]. The distance between these two peaks is 0.9 eV so that they appear to be overlapped. The P2p BE value of this experiment is within those limits reported in the literature for Na₂HPO₄ and NaH₂PO₄ found at 133.2 eV and 134.2 eV, respectively [197]. The observed ratio of hydroxide peak area to the overall O1s peak before ODPA adsorption is, according to the results of Bram et al. [111], large enough for an effective adsorption of organic acids to the Zn–Mg–Al surface.

7.4 Stability of organic acids on Zn–Mg–Al alloys

The stability of the adsorbed organic acids was studied in aqueous solutions. Static water contact angle measurements were performed for the study of the hydrophobicity of the respective ODPA covered surfaces before and after the immersion in water for defined periods of time. Such water contact angle measurements are a simple and reliable source of information concerning the state of ordering of adsorbed long chain aliphatic monolayers with a non–polar terminating group such as CH₃. The resulting tendencies are illustrated in Figure 7.9.

For comparison the values for the bare oxide covered alloy were also presented. The bare substrates showed a decrease of the contact angle with time starting from 45° and 65° most probably based on the dissolution of organic contamination in the aqueous phase and the hydroxylation of the surface oxide. The initial contact angles of the ODPA SAM covered surfaces samples were about 100°–110° indicating a well ordered aliphatic monolayer[106]. The SAM coated and bare alloy surface samples were then immersed in water several times for 10 min and afterwards dried in a stream of pure nitrogen. After seven cycles of immersion, the contact angle of the bare substrates was about 10° to 30°.

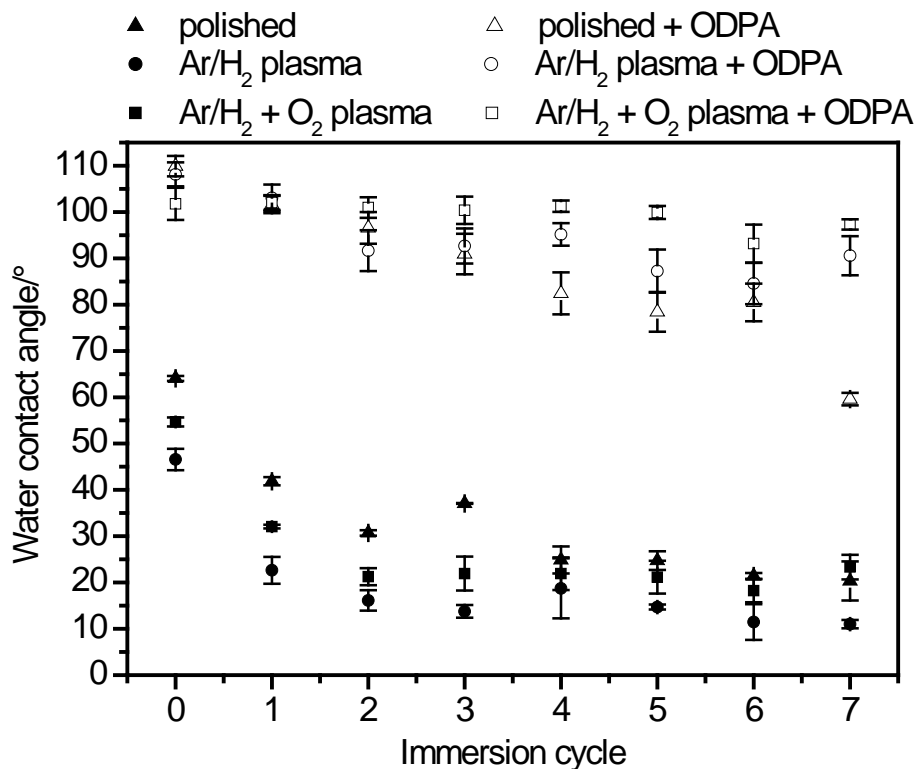


Figure 7.9: Water contact angle of polished and plasma treated Zn–Mg–Al alloy coated with ODPA versus the number of immersion cycles in water. The samples were immersed in water for 10 min in each case and afterwards dried in a stream of nitrogen. The measurements were accomplished with three different states of the alloy surface: the polished surface (circle), the Ar/H₂ plasma treated surface (diamond) and the subsequently O₂ plasma treated surface (cross).

In contrast, contact angles over the immersion time for ODPA covered plasma treated surfaces decreased only slowly with time. The combination of the reductive/ oxidative plasma treatment led to the most stable contact angles. Especially the ODPA SAM on the just-polished surface showed a significantly lower stability which can be attributed to the residual surface contamination which hinders the adsorption and self-assembly of the organophosphonic acid.

7.5 Blocking of surface sites oxide covered on Zn–Mg–Al alloys by ODPA SAMs

The reactivity of Zn–Mg–Al alloy surfaces was analyzed by means of cyclic voltammetry in borate buffer.

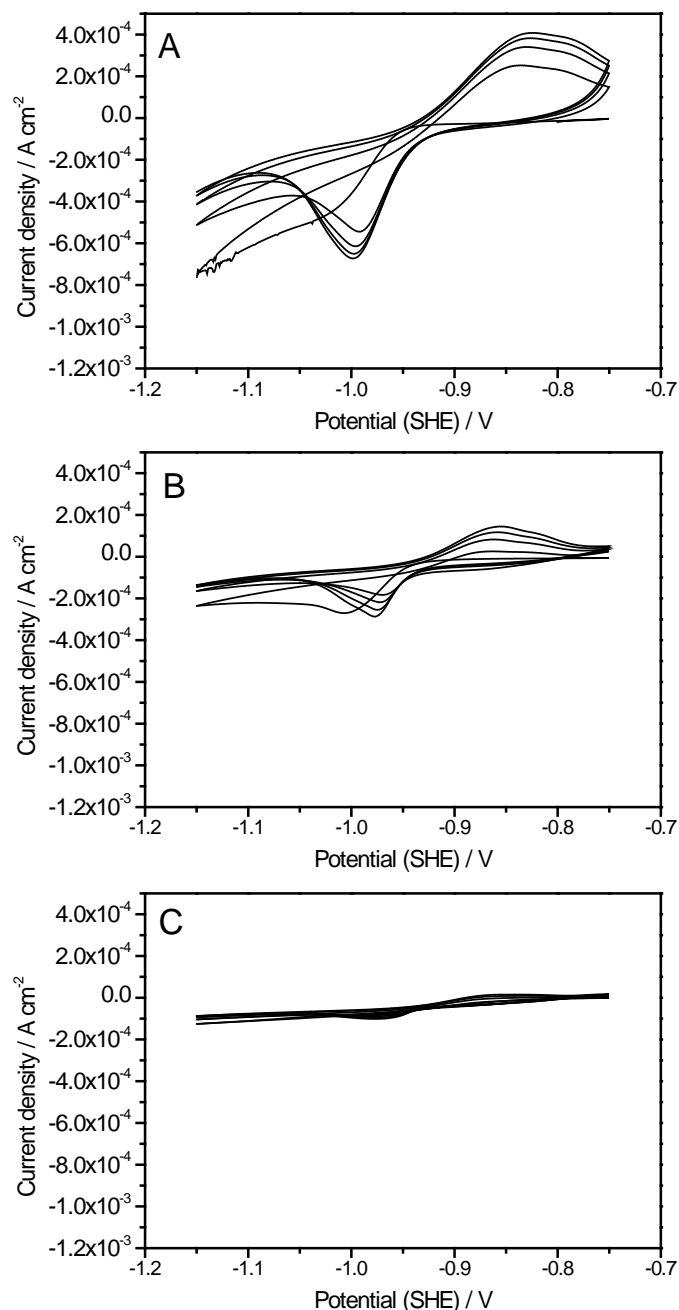


Figure 7.10: Cyclic voltammograms measured in borate buffer of ODPA monolayer covered samples; a polished Zn–Mg–Al alloy surface (A), after 60 s Ar/H₂ plasma modification (B) and after subsequent 60 s O₂ plasma modification (C).

In Figure 7.10 the cyclic voltammograms of the polished and plasma modified surfaces covered by ODPA are shown. For all substrates, the ODPA monolayer formation led to significant reduction in the redox current densities in comparison to the bare substrate.

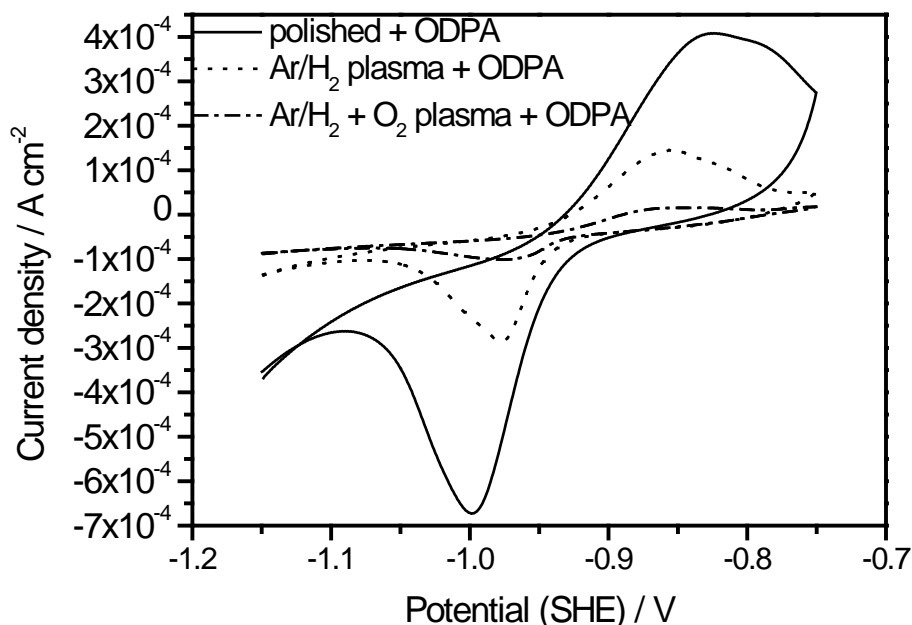


Figure 7.11: Comparison of the fourth cyclic voltammogram measured in borate buffer of ODPA monolayer covered samples; a polished Zn–Mg–Al alloy surface (solid line), after 60 s Ar/H₂ plasma modification (dotted line) and after subsequent 60 s O₂ plasma modification (dashed line).

The polished sample covered with an ODPA monolayer showed an increase of the current density during the potential sweeps (Figure 7.10A). After four cycles the current density reached the same value as for the uncovered sample (Figure 7.5A). This indicates that the ODPA layer is almost completely removed after the fourth cycle due to the low stability of the ODPA monolayer on the zinc alloy as already observed by means of contact angle studies. The reductive plasma treated sample covered with ODPA (Figure 7.10B) showed only a slight increase of the current densities during the cycles (Figure 7.5B). For the sample treated with an Ar/H₂ plasma, a subsequent O₂ plasma and ODPA adsorption (Figure 7.10C) no significant current density increase was observed during the cycles. In Figure 7.11 the comparison of the last cycle of the polished and plasma treated samples covered with ODPA is shown. The maximum current density of the anodic peak decreased from $4.0 \times 10^{-4} \text{ A cm}^{-2}$

on the polished surface to about $1.5 \times 10^{-4} \text{ A cm}^{-2}$ on the Ar/H₂ and to $0.15 \times 10^{-4} \text{ A cm}^{-2}$ for the additionally O₂ plasma modified Zn–Mg–Al alloy surface.

For the plasma treated and ODPa covered Zn–Mg–Al substrate a strong decrease of the anodic and cathodic current density was observed. The comparison of the bare and covered with ODPa substrate of Zn–Mg–Al with Ar/H₂ shows a decrease of the maximum anodic current density from $3.8 \times 10^{-4} \text{ A cm}^{-2}$ to $1.5 \times 10^{-4} \text{ A cm}^{-2}$. For the samples with subsequent O₂ plasma treatment the maximum anodic current density for the bare substrate decreased from $1.3 \times 10^{-4} \text{ A cm}^{-2}$ to $0.15 \times 10^{-4} \text{ A cm}^{-2}$ for the SAM covered sample.

7.6 Conclusions

XPS results clearly demonstrate the change of the chemical composition of the passive film formed on a Zn–Al–Mg alloy as a result of reducing and oxidizing plasma treatments. The Ar/H₂ plasma reduces the carbon contamination and increases the content of aluminum and magnesium oxide in the outermost oxide layer while ZnO is partially reduced to Zn. An additional O₂ plasma treatment again increases the ZnO layer thickness which is likely to occur below the Al and Mg rich oxide film formed after the reducing plasma.

This mixed surface Al,Mg–oxide film formation leads to a strong inhibition of redox processes of the alloy surface as revealed by cyclic voltammetry. The formation of self-assembled monolayers of ODPa was influenced by the oxide layer composition. As revealed by means of PM–IRRAS data and static water contact angles, ODPa SAMs show an improved ordering and a higher stability in aqueous solutions for surfaces enriched in Mg and Al–oxides in comparison to those which are rich in ZnO. The combination of an oxide enriched in Al and Mg with an ODPa SAM leads to a strong inhibition of redox reactions of the oxide film surface.

8 Surface chemistry and adhesive properties of plasma modified Zn–Mg–Al alloy coatings²

Aminopropylphosphonic acid (APPA) was investigated as a short-chain bi-functional adhesion promoter to enhance the interface stability of an epoxy amine adhesive coated zinc magnesium aluminum alloy coated steel. The effect of oxidative and reductive plasma treatments on the surface chemistry, the adhesive and electrochemical properties of the passive film was studied by means of Fourier transform – infrared reflection absorption spectroscopy (FT–IRRAS), X-ray photoelectron spectroscopy (XPS), a 90° peel test at >95 % r.h. and scanning Kelvin probe (SKP) measurements. FT–IRRAS in combination with XPS analysis showed that even in the plasma cleaned state and after the adsorption of the phosphonic acid, the passive film still contains carbonate ions. Both plasma treatments led to a negative shift of the interfacial electrode potential and to a significant increase in the peel force of an epoxy film, due to desorption of weakly bound carboxylic acids as well as enrichment of Mg and Al ions in the passive film surface.

8.1 Experimental

8.1.1 Modification of the surface by plasma treatment

Zinc magnesium aluminum coated steel provided by ThyssenKrupp Steel Europe AG (ZM) was cut into coupons of 45 mm x 10 mm size and cleaned with a three-step solvent cleaning procedure. The substrates were introduced subsequently in an ultrasonic bath for 30 min, first in THF then in iso-propanol and finally in ethanol (all solvents, reagent grade, Merck, Germany). After each step the coupons were dried with clean, compressed air.

The low pressure plasma treatments were performed in a custom made plasma chamber operated at a base pressure of 10^{-4} mbar [80; 199]. Pure Ar or an equimolar mixture of Ar/O₂ (Air Liquide, Argon 5.0 and Oxygen 4.5) was dosed into the plasma chamber to reach a process pressure of 0.3 mbar. The duration of the plasma treatments was selected as 380 s.

² The content of this chapter is adopted from publication [198].

8.1.2 Application of adhesion promoter and the model polymer coating

Two different sets of samples were prepared and analyzed to investigate the individual effects of different plasma treatments and the subsequent APPA adsorption. In the first set the model epoxy–amine polymer was applied directly onto the as–cleaned and plasma modified ZnMgAl alloy samples, whereas in the second set APPA adsorption was performed on the samples prior to the coating of the polymer film. The adhesion promoter APPA (99.99%, Sigma Aldrich, Germany) treatment was performed by means of self–assembly from 1 mM aqueous solution of the respective salt. The adsorption time was chosen as 1.5 h, followed by a rinsing step with de–ionized water and drying under a stream of clean, dry air. As the model polymer film a hot–curing two–component epoxy resin adhesive was used (epoxy resin D.E.R. 331 P provided by Dow Chemicals, Germany and amine hardener Jeffamin D400 provided by Huntsmann, Germany). The adhesive was mixed and degased in vacuum for two hours prior to the application on the zinc magnesium aluminum alloy. The adhesive film was countered by an aluminum foil to form a joint to avoid artefacts like preferential evaporation during the hardening. The hardening was performed for 1 h at 393K with a mechanical pressure of approximately 50 g/cm² [9] on the sandwich–type ZM alloy/(with and without APPA)/adhesive/aluminum foil specimen arrangement. After the hardening, the aluminum foil was removed, leaving the substrate with about 130µm thick layer of the free standing polymer film.

8.1.3 Characterization of the surface chemistry after plasma treatments and APPA adsorption

X–ray photoelectron spectroscopy was used to study the influence of the low pressure plasma treatments on the surface chemistry of ZM and the adsorption of APPA. X–ray photoelectron spectra were recorded with an Omicron ESCA+ System (Omicron NanoTechnology GmbH, Germany), utilizing a Al K α X–ray source and a spot diameter of 600µm, with a step size of 0.05 eV at a constant pass energy of 25 eV and a base pressure of < 2·10^{–9} mbar. The take–off angle was set to 60° with respect to the surface plane. The spectra were fitted with the CASA XPS [200] software using a Shirley background and a

mixture of Gaussian and Lorentzian fitting for the peak shapes. For the quantification, relative sensitivity factors supplied from Omicron GmbH were implemented in the CASA XPS database. All spectra were calibrated using the C1s peak (binding energy, BE = 285 eV) as internal reference.

A custom made height regulated scanning Kelvin probe was used to analyze the plasma induced changes in the oxide chemistry [55; 124; 127; 130]. The experiments were performed under high humidity (>90% r.h.) and the interface potentials were referenced to Cu/CuSO₄ prior to the measurements.

The formation of aminopropylphosphonic acid films on as-cleaned and plasma modified surfaces was investigated by means of Fourier transform – infrared reflection absorption spectroscopy (FT–IRRAS, Bruker Vertex V70). The spectra were collected at an 80° incidence angle by means of a MIR–DTGS (mid–infrared deuterated triglycine sulfate) detector, with a resolution of 4 cm⁻¹ by averaging over 512 single scans to achieve spectra with a high signal to noise ratio.

8.1.4 Peel–test measurements

To measure the wet de–adhesion force, peel–off tests were performed [37; 126; 154]. The samples coated with the free–standing polymer film were exposed to high humidity (>97%) at 40 °C for 24 hours prior to the peel–test measurements. Peel–tests were performed at a constant angle perpendicular to the sample surface and with constant 4mm/min peel velocity using a force gauge (model ZP–5, Imada, Tokyo, Japan) and a motorized peel tester (MV–220 Motorized Test Stand, Imada, Tokyo, Japan) under 90% relative humidity at a temperature of 20.5 ± 0.5 °C.

8.2 Characterization of the plasma modified samples

X–ray photoelectron spectroscopic (XPS) studies have been performed to reveal the influence of the plasma modification on the native oxide layer. The overall atomic compositions and component percentages of possible oxidation states for each element

along with the respective binding energy (BE) and full width at half maximum (FWHM) values used for the analysis are summarized in Table 8.1. As seen in Table 8.1, the outermost native oxide layer, which determines the chemical and electrochemical properties of the alloy surface, consists of a solid solution of magnesium–aluminum–zinc hydroxide with a small amount of respective oxides and carbonates. The dominant species on the solvent cleaned ZM surface was oxygen with 45.4 at.% and carbon with 27.8 at.%. The C1s spectra indicated the presence of different organic species like aliphatic hydrocarbons, alcohols, carboxylic acids and carbonates. All plasma treatments reduced the oxygen containing carbon contaminations.

In Figure 8.1 the O1s detail spectra of the solvent cleaned and plasma treated surfaces are presented. On the as-cleaned sample the O1s signal is composed of three components, which were fitted by symmetrical profiles resulting in a FWHM of 2.1 eV. The peak observed at 530.6 eV was assigned to oxygen O^{2-} ions in the metal oxide, whereas the component at 532.1 eV includes the contributions from surface hydroxides and oxygen containing organic adsorbates at the surface. The peak at 533.4 eV was assigned to molecular water, generally present in the oxy-hydroxides of aluminum and magnesium surfaces and the carbonate-based species in the oxide layer.

The comparison of the as-cleaned and plasma treated surfaces has shown no significant changes in the overall oxygen content and the differences were observed mainly in the hydroxide to oxide ratio indicating a successful modification of the surface chemistry in favour of oxidic species. For the plasma modified samples, the maximum of the O1s signal shifted slightly to lower binding energies compared to the as-cleaned sample which could be explained with the change in the oxide/hydroxide ratio.

Table 8.1: Atomic composition (at%) as analyzed by XPS at 60° for native, Ar plasma and Ar/O₂ plasma treated ZM surfaces.

	Solvent cleaned						Ar plasma						Ar/O ₂ plasma					
	BE/eV	FWHM	Peak%	at%	BE/eV	FWHM	Peak%	at%	BE/eV	FWHM	Peak%	at%	BE/eV	FWHM	Peak%	at%		
Mg 2p	Mg ^{0/2+}	50.2	2.2	100.0	13.9	50.4	1.8	100.0	11.3	50.4	2.0	100.0	50.4	2.0	100.0	12.2		
Al 2p	Al ^{0/3+}	74.3	2.0	100.0	9.4	74.4	1.8	100.0	13.0	74.5	1.9	100.0	74.5	1.9	100.0	12.5		
C 1s	C–C/ C–H	285.0		64.4		285.0		75.9		285.0		75.4			75.4			
	C–OH	286.4	1.7	19.4	27.8	286.2	1.5	12.2	28.7	286.3	1.5	12.3	286.3	1.5	12.3	28.0		
	C–OOH	288.6		8.1		288.9		6.5		288.9		7.3			7.3			
	CO ₃ ²⁻	290.0		8.1		290.2		5.5		290.3		5.1			5.1			
O 1s	O ²⁻	530.6		16.0		531.0		27.8		530.9		29.9			29.9			
	OH ⁻	532.1	2.1	70.8	45.4	532.2	1.9	62.7	44.3	532.2	2.0	61.4		2.0	61.4	44.2		
	H ₂ O	533.4		13.2		533.3		9.5		533.3		8.8			8.8			
Zn 2p _{3/2}	Zn ^{0/2+}	1022.7	2.3	100.0	3.5	1022.6	2.0	100.0	2.7	1022.5	2.2	100.0	1022.5	2.2	100.0	3.2		

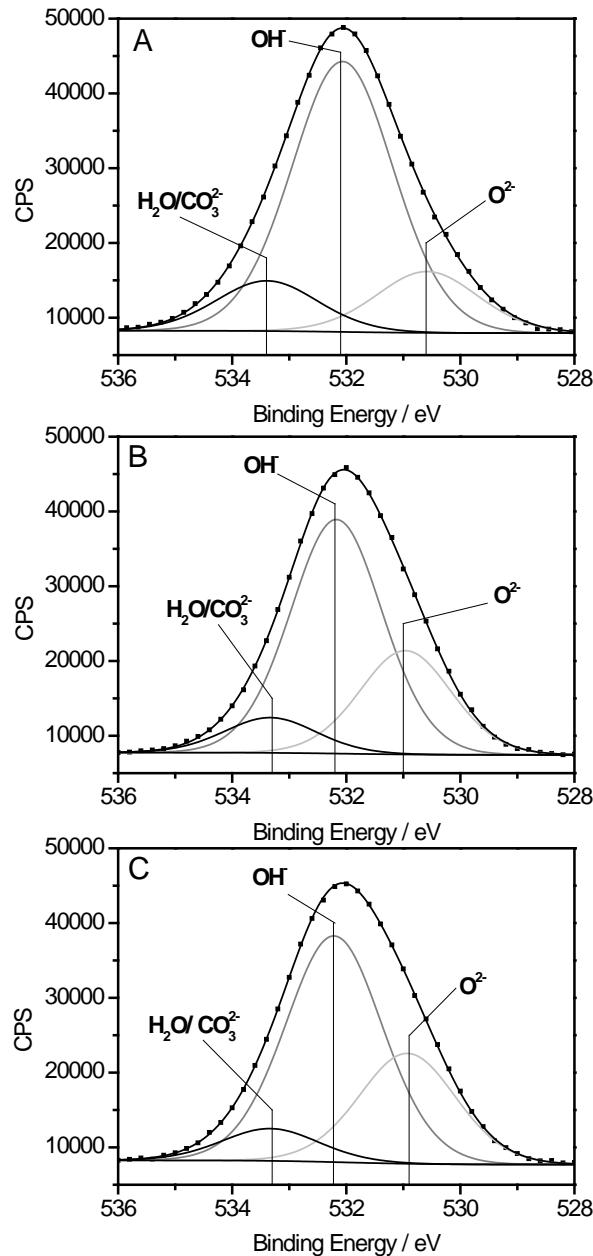


Figure 8.1: XPS O1s detail spectra of (A) as-cleaned, (B) Ar plasma and (C) Ar/O₂ plasma treated ZM surfaces.

In Figure 8.2, the changes in Al, Mg and Zn to the sum of the metals on the as-cleaned and plasma activated ZM surfaces are presented. For the as-cleaned surface the magnesium content dominates the metallic contributions on the surface. After the reductive Ar plasma treatment, an increase in the aluminum content and a decrease in the magnesium content were observed (Figure 8.2). The oxidative Ar/O₂ plasma treatment resulted in a slight increase in aluminum concentration compared to the as-cleaned surface along with a slight

decrease in magnesium yielding an almost equimolar ratio of both metals (Figure 8.2). However a significantly higher amount of Al and Mg compared to Zn were observed on the plasma modified surfaces, especially on the Ar plasma treated surfaces. The surface concentration of zinc was virtually not affected by the plasma treatments.

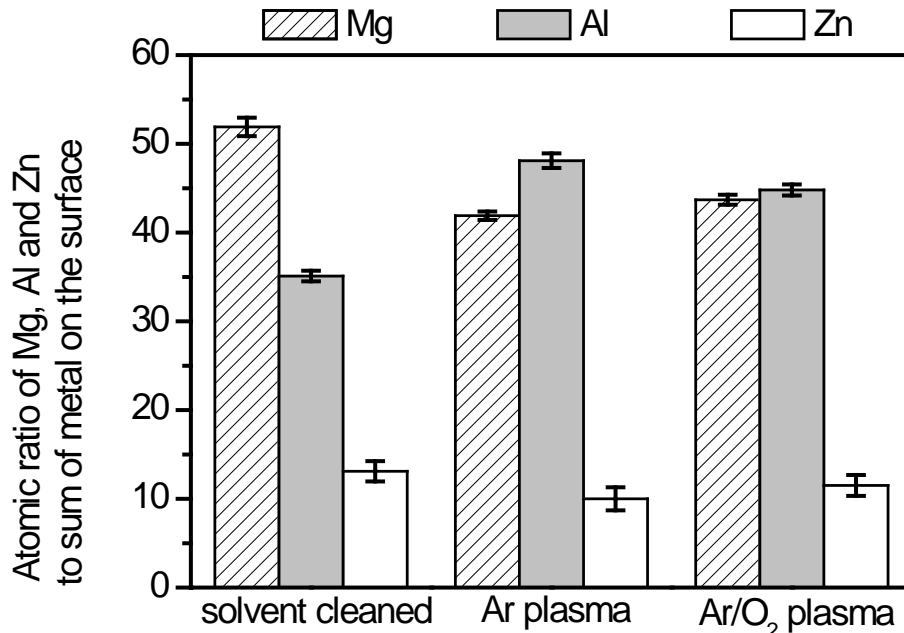


Figure 8.2: Atomic ratio of Mg, Al and Zn to sum of metal concentration on the surface as a function of the surface condition.

Furthermore, scanning Kelvin probe (SKP) measurements were performed to investigate the changes in the electrochemical properties of the alloy surfaces after the plasma treatments. Half of the sample was protected during the plasma treatment to enable a direct comparison of the potential of the native and the plasma modified oxide surface film. In the SKP profiles presented in Figure 8.3, shifts to more negative potentials were observed both after the argon and the oxygen plasma treatments. The native oxide layer on zinc magnesium showed a potential of -360mVSHE while the potential of the plasma modified surface was about 300 mV more negative. It is known that the Volta potential is influenced by several factors such as oxide thickness, oxide conductivity, chemical composition, and surface adsorbates [201; 202]. Additionally, the Volta potential correlates with the band gap width which is affected by parameters like e.g. the (hydr)oxide content, oxide resistance, doping concentration, etc. [60; 203].

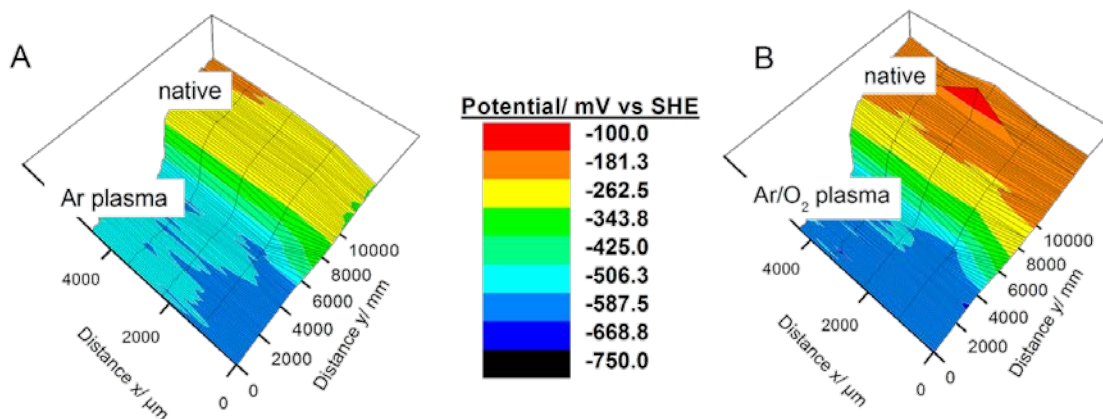


Figure 8.3: SKP potential profile of a Zn–Mg–Al sample half treated with a) Ar– and b) Ar/O₂– plasma treated in dry atmosphere (< 10% r.h.)

For the Ar and Ar/O₂ plasma modified substrates, the increase of the Al concentration on the surface caused a strong decrease of the potential which is explained by the combined effect of the insulating nature of aluminum oxide and the lowered hydroxide/oxide ratio of the surface films after plasma treatment [60; 64].

8.3 Adsorption of APPA on the plasma modified sample surface

The formation of APPA monolayers on the as-cleaned and plasma modified alloy surfaces was studied by means of FT–IRRAS and XPS. FT–IRRAS enables the determination of the interfacial interaction modes based on the appearance and the peak positions of P–O and P=O vibrations [9; 106]. The FT–IRRA difference spectra of the ZM after APPA adsorption, with the respectively pretreated substrates as reference, are presented in Figure 8.4. In all spectra the peak observed at 1000 cm⁻¹ was assigned to the Al–O and Al–OH vibration according to Wapner et al [9]. In the spectrum of the solvent cleaned sample an additional peak has been observed at 1170 cm⁻¹ which was assigned together with the deformation vibrations at 800 – 950 cm⁻¹ to the ZnOH vibrations [13]. A broad peak was observed around 1100 cm⁻¹ for the Ar and Ar/O₂ plasma treatments. This peak is assigned to the asymmetric P–O vibration of phosphonate groups. The absence of the free acid groups P=O and P–OH suggests that the adsorbed phosphonic acid functionality is deprotonated, which is in consistent with the presence of the broad peak belonging to the PO₃²⁻ stretching mode. In the case of solvent cleaned surfaces, the peak maximum in the range of the P–O vibration

shifted to lower wavenumbers which could be explained by an overlapping with the aluminum oxide vibration. Additionally, a peak at around 880 cm^{-1} appeared on the solvent cleaned substrate. This peak can be assigned to the P–OH vibrations of the phosphonic acid group [7; 8; 42; 97].

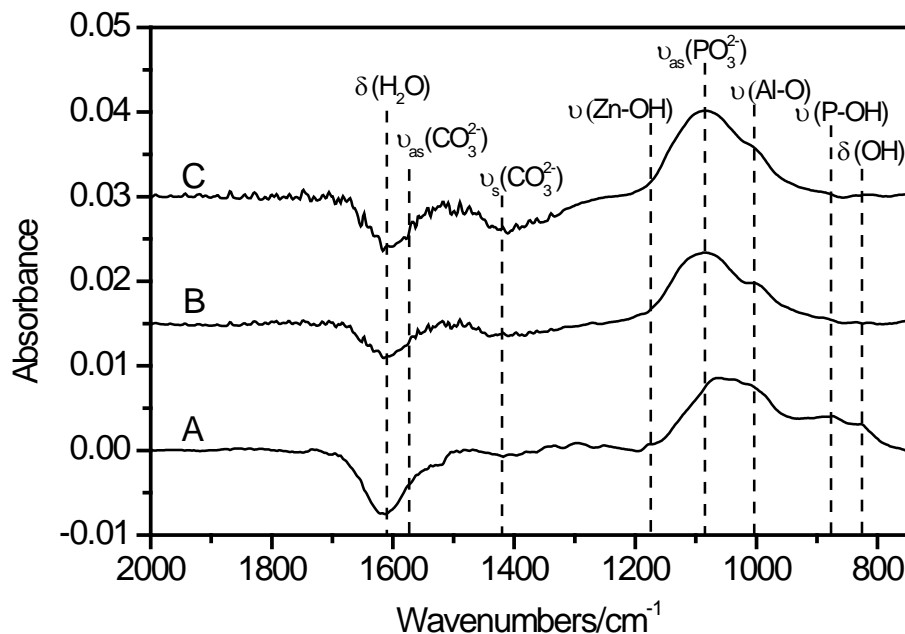


Figure 8.4: FT-IRRA difference spectra of (A) solvent cleaned, (B) Ar plasma and (C) Ar/O₂ plasma treated ZM surfaces (the difference spectra has been calculated by taking as-cleaned (for A), Ar plasma treated (for B) and Ar/O₂ (for C) plasma treated ZM surfaces as reference).

The presence of the P–OH vibration modes in the spectrum leads to the conclusion that the binding mechanism on the solvent cleaned surface is governed by a mixed mode adsorption, where tri-dentate bonds coexist with bidentate bonds. The negative peak around 1600 cm^{-1} is assigned to the deformation vibration of water, which is decreasing after the adsorption of APPA for all surfaces. In the infrared spectra of the Ar/O₂ treated surface an additional negative peak has been observed at 1420 cm^{-1} , which was assigned to the symmetric vibration of carbonate groups indicating a minute remove of surface contaminations by the aqueous APPA solution.

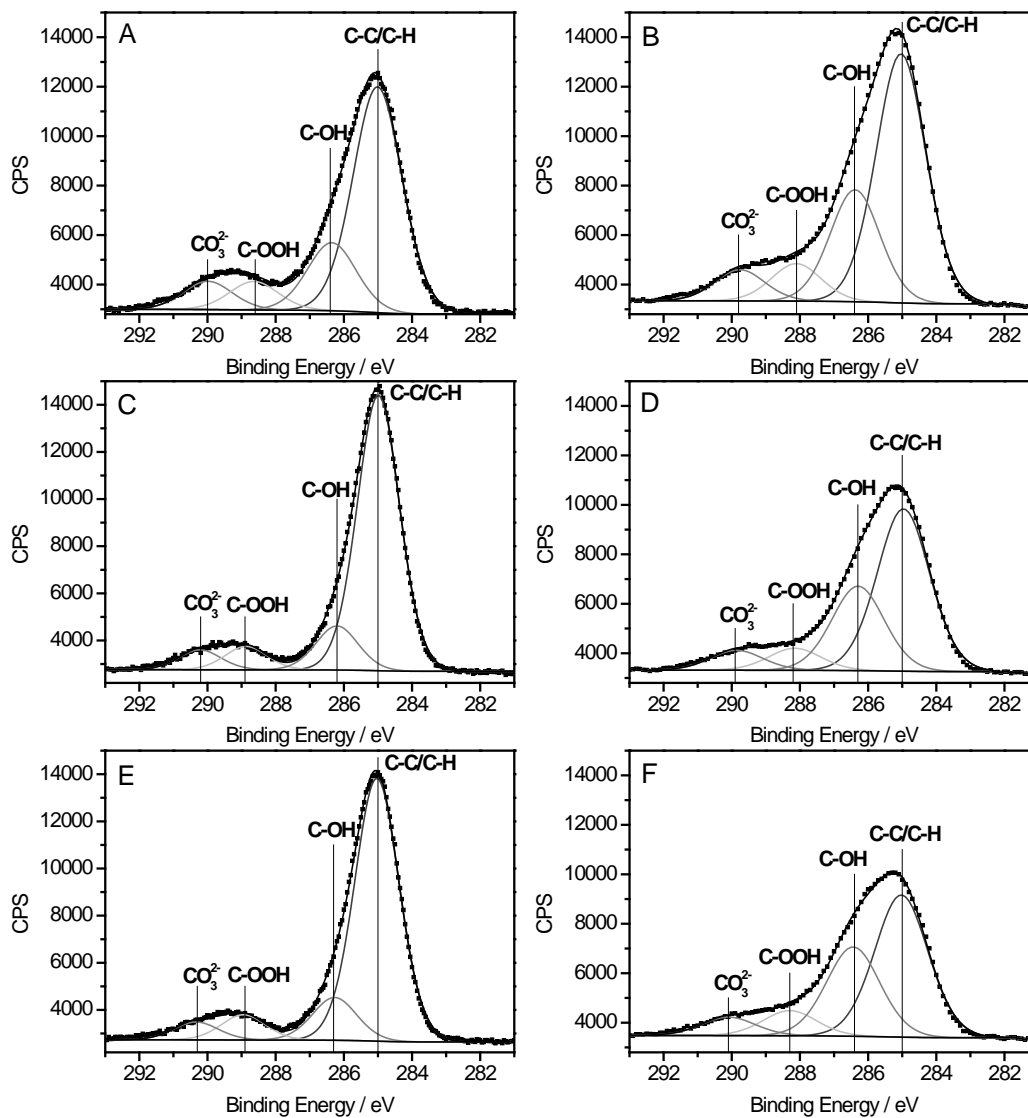


Figure 8.5: (A), (C) and (E): XPS C1s detail spectra of ZM as-cleaned and after plasma modifications. (B), (D) and (F): XPS C1s spectra of samples pretreated as above and immersed in 10^{-3} M aqueous APPA solution. First row ((A) and (B)): solvent cleaned samples. Second row ((C) and (D)): samples were Ar plasma treated. Third row ((E) and (F)): samples were activated via Ar/O₂ plasma.

The C 1s detail spectra of the XPS measurements of the ZM surface before and after the adsorption of APPA are shown in Figure 8.5. The C1s spectra of all samples contain four components. In comparison to the bare substrates the C1s spectra for the as-cleaned and plasma treated samples after APPA adsorption a slight decrease of the carbonate and organocarboxylates was observed. This result supported the FT-IRRAS results regarding the negative peak in the region for carbonate species.

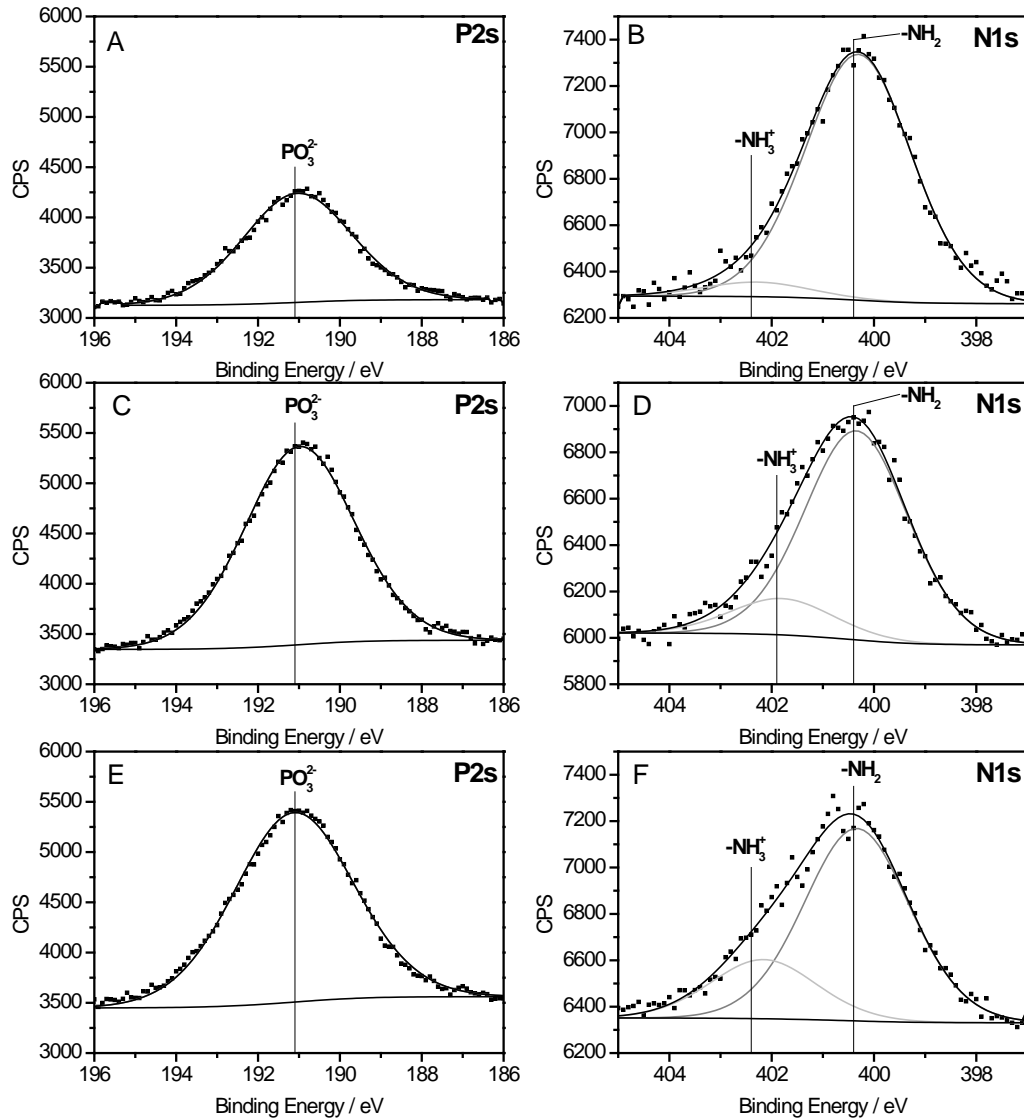


Figure 8.6: (A), (C) and (E): XPS P2s detail spectra of ZM as-cleaned and after plasma modifications immersed in 10^{-3} M aqueous APPA solution. (B), (D) and (F): XPS N1s spectra of samples pretreated as above and immersed in 10^{-3} M APPA. First row ((A) and (B)): solvent cleaned samples. Second row ((C) and (D)): samples were Ar plasma treated. Third row ((E) and (F)): samples were activated via Ar/O₂ plasma.

The data of the XPS analysis on the ZM surfaces after the adsorption of APPA with the corresponding peak positions and atomic concentrations are presented in Table 8.2. After APPA adsorption, the O1s signal did not show any peak for water which is also observed in the FT-IRRA spectra. The N1s and P2s detail spectra of the ZM surfaces after the adsorption of APPA are shown in Figure 8.6.

Table 8.2: Atomic composition (at.%) of APPA covered samples analyzed by XPS.

	Solvent cleaned						Ar plasma						Ar/O ₂ plasma					
	BE/eV	FWHM	Peak%	at%	BE/eV	FWHM	Peak%	at%	BE/eV	FWHM	Peak%	at%	BE/eV	FWHM	Peak%	at%		
Mg 2p	50.2	2.2	100.0	8.4	50.3	2.3	100.0	6.7	50.4	2.5	100.0	6.6						
Al 2p	74.4	2.0	100.0	7.4	74.4	2.2	100.0	9.0	74.4	2.3	100.0	10.1						
P 2s	191.1	3.1	100.0	2.7	191.1	3.2	100.0	4.8	191.3	3.4	100.0	4.7						
C 1s	285.0		57.9		285.0		56.2		285.0		51.7							
	286.4	1.7	26.1	28.7	286.3	1.8	29.3	19.6	286.4	1.8	32.5	17.8						
	288.1		8.7		288.2		7.6		288.3		9.1							
	289.5		7.3		289.9		6.9		290.1		6.7							
N 1s	400.4	2.4	94.4	1.5	400.4	2.4	85.2	1.3	400.5	2.4	64.4	1.3						
	402.4		5.6		401.9		14.8		402.4		35.6							
O 1s	532.0	2.5	85.4	45.6	531.7	2.4	76.4	50.6	531.8	2.6	71.1	51.9						
	533.5		14.6		533.0		23.6		533.2		28.9							
Zn 2p _{3/2}	1022.7	2.4	100.0	5.8	1022.6	2.5	100.0	7.9	1022.7	2.8	100.0	7.7						

Prior to the adsorption of APPA, no phosphorus or nitrogen containing species were observed in the XP spectrum. The overall composition of the surface confirmed that APPA could be irreversibly adsorbed on the ZM surface. The maximum of the P2s peak was observed for binding energies around 191.0 eV. The N1s peak consists of two peaks for the NH₂ and NH₃⁺ ion. The binding energy for the non protonated NH₂ group is located at around 400.3 eV and at 402.3 eV for the protonated state. The adsorption of the aminophosphonate adhesion promoter on the ZM surface occurs via the phosphonic acid functionality as shown by means of FT-IRRAS measurements (Figure 8.4). Nevertheless, a partial adsorption via the amine function cannot be fully excluded. The presence of two amine species might indicate the adsorption of carboxylic acids on the amino terminated surface. The formation of the alkylammonium salt of the carbamic acid as primary product between carbon dioxide and neat amines (R–NHCO₂⁻ +NH₃–R) has already been discussed for adsorbed aminosilane layers by Dreyfuss et al [204] and for adsorbed aminophosphonate layers by Wapner et al [9].

8.4 The effect of plasma treatments and APPA adsorption on the adhesion of epoxy amine coating on Zn–Mg–Al alloy surfaces

In order to analyse the influence of the plasma treatment and application of APPA as adhesion promoter on the adhesion strength, wet de-adhesion forces were measured by means of a 90° peel-test setup [37; 126; 154]. In Figure 8.7, the peel forces of the model epoxy-amine polymer film on the as-cleaned and plasma treated ZM surfaces with and without APPA layer are presented.

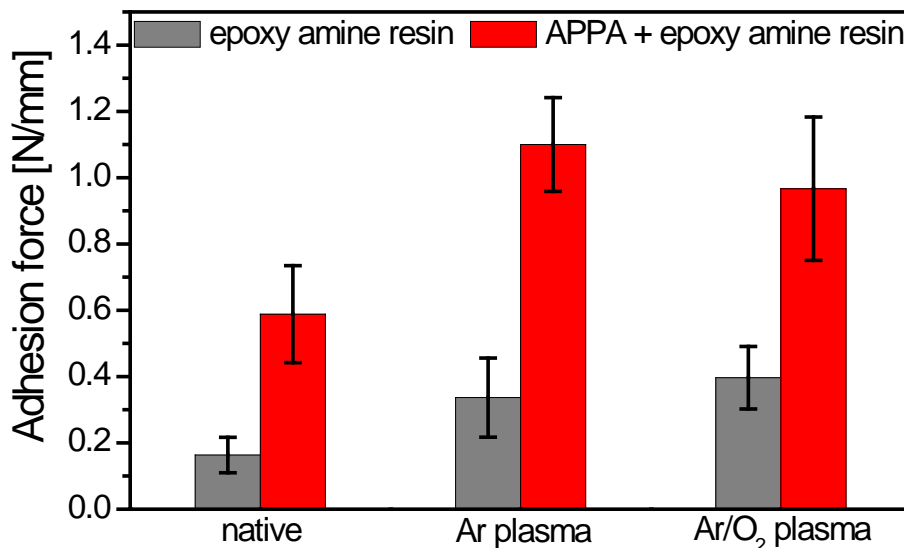


Figure 8.7: Peel forces measured in humid atmosphere of the native and plasma treated surfaces with and without APPA layer coated with epoxy amine resin.

The peel forces observed on the Ar/O₂ and with Ar plasma treated samples were 0.4 N/mm and 0.34 N/mm, respectively. In comparison, for the as-cleaned alloy surface a much lower peel force of 0.16 N/mm was observed. Considering the cleaning effect observed with both plasma treatments, the increase in adhesion forces could be explained by the lowering of the carboxylate-based surface contaminants. Moreover, it is known that the presence of surface hydroxyls and water have an adverse effect on macroscopic adhesion [9; 113]. Based on the XPS results, a decrease in the surface hydroxyl concentration and a significant decrease in adsorbed molecular water were observed together with a decrease in the carboxylate containing surface contaminations. The combination of these effects could explain the observed increase of adhesion after both plasma treatments.

The adhesion force strongly increased for all systems when APPA was applied on the alloy surface. APPA treatment on the solvent cleaned substrate resulted in a three-fold increase of peel force. On the Ar and Ar/O₂ plasma treated surfaces similar even higher adhesion forces of 1.1 N/mm and 0.97 N/mm were observed when APPA was applied as an interfacial adhesion promoter. This result is in good agreement with the spectroscopic findings.

8.5 Conclusions

The influence of Ar and Ar/O₂ plasma modifications and the adsorption of APPA as a monomolecular adhesion promoting layer were investigated on ZnMgAl–alloy surfaces. The results demonstrated that by plasma treatments, not only the surface contaminations could be reduced but the hydroxide–rich surface layer was converted to an oxide rich film. Moreover, the Al surface concentration increased. However, the passive film contained carbonate ions before and after the plasma activation step. Both chemical changes led to a negative shift of the surface potentials as measured by SKP. Moreover, the change in surface chemistry towards higher aluminum concentrations and slight removal of water after both plasma treatments resulted in an increase of the peel forces of the epoxy amine polymer on the ZM surface in humid environment.

APPA adsorption was investigated on as–cleaned and plasma treated alloy surfaces and the coordinative bonding of the APPA and the remove of molecular water was observed on both plasma treated ZM surfaces. The peel test results showed a significant increase of the peel forces after APPA adsorption on all investigated surfaces in comparison to the bare oxide surfaces. The plasma activation led to an increased density of coordinative bonds between the phosphonic acid group and the oxide covered alloy surface which resulted in higher peel forces in humid environment. The results show that the molecular adhesion promotion by means of bi–functional phosphonic acids can be successfully done for a ZnMg Al–alloy. However, a plasma activation of the surface leads to an even improved interfacial binding process.

9 Overall conclusions and outlook

The aim of the presented work was to develop a deeper understanding of the mechanism of corrosion and corrosion protection of zinc magnesium aluminum coated steel. The corrosion properties of zinc aluminum coated steel was used as a reference. In this context the influence of plasma and phosphonic acids were tested in form of long chain for self-assembly and as short chain molecule as adhesion promoter.

The SEM images clearly demonstrated inclusions on the surface and by means of EDX this inclusions could be identified as aluminum/iron particles on the surface. Additionally the SKPFM measurements showed potential differences on the grain independent of the topography which could be assigned to the inclusions observed in SEM and EDX. The EBSD measurement has shown the preferred orientation of the crystallized zinc underneath the native oxide layer to be 0001.

The in-situ corrosion analysis performed in 0.05 M NaCl showed the growth of mainly zinc oxide preferred at the grain boundaries and at defects on the surface. Additionally an increase of the pH was observed which stabilize the formed zinc oxide on the surface. The Raman spectra obtained during electrolyte flow showed different composition of the oxide layer directly after the exposure to the electrolyte dependent on the pH. In the case of pH 3 the dissolution and oxidation of zinc were in equilibrium therefore the OCP stayed constant during the exposure. In neutral and alkaline pH the OCP was 100 mV decreasing. The amount of oxide and hydroxide is on the grain increasing at pH 7 and at the grain boundary the amount stays constant. At pH 11 the amount is slowly increasing at all points.

The SEM pictures clearly demonstrated the complex microstructure composed of Zn, Zn-Mg and Zn-Al phases. The in-situ corrosion analysis in 0.05 M sodium chloride solution showed that the corrosion started at several points and was then growing over the surface. As main corrosion product ZnO was monitored in the Raman spectra. Additionally an increase of the pH was observed which stabilize the formed of zinc oxide. The Raman spectra of the pH dependent measurements showed different composition of the oxide layer after exposure to the electrolyte. In the case of pH 3 and 7 the dissolution and oxidation of zinc were in equilibrium therefore the OCP stayed constant during the exposure. At pH 11 the amount is slowly increasing at all points.

The in-situ corrosion analysis performed in 0.05 M sodium chloride solution and 0.5 ml/ min flow rate on Zn-Al/Fe and Zn-Mg-Al/Fe interfaces showed to protect the iron. On the zinc/iron surface zinc oxide was mainly formed in the zinc surface. In comparison to this Zn-Mg-Al/ Fe cut edge showed a dissolution of ions which were then precipitated on the iron surface.

XPS results clearly demonstrate the change of the chemical composition of the passive film formed on a Zn-Al-Mg alloy as a result of reducing and oxidizing plasma treatments. The Ar/H₂ plasma reduces the carbon contamination and increases the content of aluminum and magnesium oxide in the outermost oxide layer while ZnO is partially reduced to Zn. An additional O₂ plasma treatment again increases the ZnO layer thickness which is likely to occur below the Al and Mg rich oxide film formed after the reducing plasma.

This mixed surface Al,Mg-oxide film formation leads to a strong inhibition of redox processes of the alloy surface as revealed by cyclic voltammetry. The formation of self-assembled monolayers of ODPa was influenced by the oxide layer composition. As revealed by means of PM-IRRAS data and static water contact angles, ODPa SAMs show an improved ordering and a higher stability in aqueous solutions for surfaces enriched in Mg and Al-oxides in comparison to those which are rich in ZnO. The combination of an oxide enriched in Al and Mg with an ODPa SAM leads to a strong inhibition of redox reactions of the oxide film surface.

In this paper, the influence of reductive and oxidative plasma modification and the adsorption of APPA as adhesion promoter were investigated on ZM surfaces. The results demonstrated that with both plasma treatments, the hydroxide-rich surface layer was converted to an oxide rich film and the Al concentration was increasing resulting in a negative shift of the SKP potentials. Moreover, the change in surface chemistry towards higher aluminum concentrations and slight removal of water after both plasma treatments resulted in an increase of the adhesion forces of the model epoxy amine polymer on the ZM surface.

APPA adsorption was investigated on as-cleaned and plasma treated alloy surfaces and the coordinative bonding of the APPA and the remove of molecular water was observed on both plasma treated ZM surfaces. The peel test results have shown a significant increase of the adhesion forces after APPA adsorption on all investigated surfaces with respect to the bare

substrates. The presence of coordinative bonds between the phosphonic acid group and the alloy surface have resulted in higher adhesion forces on plasma treated surfaces in comparison to the solvent cleaned surface.

Understanding the corrosion processes of the alloy interface was shown to be crucial for explaining the performance of corrosion protection of the modified alloy surfaces. But some questions related to the characterisation of the corrosion mechanism are still open, e.g. the influence of anions and cations on the corrosion rate analyzed by means of in-situ X-ray diffraction. In-situ experiments performed by Raman spectroscopy to monitor the corrosion products formed at the polymer/metal interface during the delamination process could be a possibility.

References

- [1] N. Fink, B. Wilson, G. Grundmeier, *Electrochimica Acta* 51 (2006) 2956–2963.
- [2] G. Klimow, N. Fink, G. Grundmeier, *Electrochimica Acta* 53 (2007) 1290–1299.
- [3] C. Stromberg, P. Thissen, I. Klueppel, N. Fink, G. Grundmeier, *Electrochimica Acta* 52 (2006) 804–815.
- [4] B. Wilson, N. Fink, G. Grundmeier, *Electrochimica Acta* 51 (2006) 3066–3075.
- [5] G. Grundmeier, M. Stratmann, *Annual Review of Materials Research* 35 (2005) 571–615.
- [6] K. Wapner, G. Grundmeier, *Surface & Coatings Technology* 200 (2005) 100–103.
- [7] V. Barranco, J. Carpentier, G. Grundmeier, *Electrochimica Acta* 49 (2004) 1999–2013.
- [8] I. Maege, E. Jaehne, A. Henke, H.J.P. Adler, C. Bram, C. Jung, M. Stratmann, *Progress in Organic Coatings* 34 (1998) 1–12.
- [9] K. Wapner, M. Stratmann, G. Grundmeier, *International Journal of Adhesion and Adhesives* 28 (2007) 59–70.
- [10] M. Giza, P. Thissen, G. Grundmeier, *Langmuir* 24 (2008) 8688–8694.
- [11] P. Thissen, J. Wielant, M. Koyer, S. Toews, G. Grundmeier, *Surface & Coatings Technology* 204 (2010) 3578–3584.
- [12] P. Thissen, S. Janke, G. Grundmeier, D. Tabatabai, F. Feil, W. Fürbeth, in K.U. Kainer (Ed.) *Magnesium, 8th International Conference on Magnesium Alloys and their Applications, Wiley-VCH, Weinheim, 2010*, p. 1357.
- [13] T. Titz, F. Horzenberger, K. Van den Bergh, G. Grundmeier, *Corrosion Science* 52 (2010) 369–377.
- [14] R. Serra, M.L. Zheludkevich, G. Grundmeier, M.G.S. Ferreira, *Material Science Forum* 514–516 (2006) 1401–1405.
- [15] A. Nazarov, T. Prosek, D. Thierry, *Electrochimica Acta* 53 (2008) 7531–7538.
- [16] T. Prosek, D. Thierry, C. Taxen, J. Maixner, *Corrosion Science* 49 (2007) 2676–2693.
- [17] T. Prosek, A. Nazarov, U. Bexell, D. Thierry, J. Serak, *Corrosion Science* 50 (2008) 2216–2231.
- [18] T. Prosek, N. Larche, M. Vlot, F. Goodwin, D. Thierry, *Materials and Corrosion–Werkstoffe Und Korrosion* 61 (2010) 412–420.
- [19] M.C. Bernard, A. Hugot–Le Goff, D. Massinon, N. Phillips, *Corrosion Science* 35 (1993) 1339–1349.
- [20] M.C. Bernard, A.H.–L. Goff, N. Phillips, *Journal of The Electrochemical Society* 142 (1995) 2167–2170.
- [21] M.C. Bernard, A.H.–L. Goff, N. Phillips, *Journal of The Electrochemical Society* 142 (1995) 2162–2167.
- [22] A. Hugot–Le Goff, M.C. Bernard, N. Phillips, H. Takenouti, *Materials Science Forum* 192–194 (1995) 779–788.
- [23] S. Bonk, M. Wicinski, A.W. Hassel, M. Stratmann, *Electrochemistry Communications* 6 (2004) 800–804.
- [24] Y.Y. Chen, S.C. Chung, H.C. Shih, *Corrosion Science* 48 (2006) 3547–3564.

-
- [25] Z.Y. Chen, D. Persson, C. Leygraf, *Corrosion Science* 50 (2008) 111–123.
- [26] M.R. Elsharif, Y.J. Su, C.U. Chisholm, A. Watson, *Corrosion Science* 35 (1993) 1259–1265.
- [27] P. Colomban, S. Cherifi, G. Despert, *Journal of Raman Spectroscopy* 39 (2008) 881–886.
- [28] N.C. Hosking, M.A. Strom, P.H. Shipway, C.D. Rudd, *Corrosion Science* 49 (2007) 3669–3695.
- [29] R. Lindstrom, J.E. Svensson, L.G. Johansson, *Journal of the Electrochemical Society* 149 (2002) B57–B64.
- [30] D. Persson, D. Thierry, N. LeBozec, *Corrosion Science* 53 (2011) 720–726.
- [31] S. Schuerz, M. Fleischanderl, G.H. Luckeneder, K. Preis, T. Haunschmied, G. Mori, A.C. Kneissl, *Corrosion Science* 51 (2009) 2355–2363.
- [32] S. Schürz, G.H. Luckeneder, M. Fleischanderl, P. Mack, H. Gsaller, A.C. Kneissl, G. Mori, *Corrosion Science* 52 (2010) 3271–3279.
- [33] B. Li, A. Dong, G. Zhu, S. Chu, H. Qian, C. Hu, B. Sun, J. Wang, *Surface & Coatings Technology* 206 (2012) 3989–3999.
- [34] H. Dafydd, D.A. Worsley, H.N. McMurray, *Corrosion Science* 47 (2005) 3006–3018.
- [35] L. Diaz–Ballote, R. Ramanauskas, *Corrosion Reviews* 17 (1999) 411–422.
- [36] Z.I. Ortiz, P. Diaz–Arista, Y. Meas, R. Ortega–Borges, G. Trejo, *Corrosion Science* 51 (2009) 2703–2715.
- [37] W. Fürbeth, M. Stratmann, *Corrosion Science* 43 (2001) 207–227.
- [38] W. Fürbeth, M. Stratmann, *Corrosion Science* 43 (2001) 229–241.
- [39] W. Fürbeth, M. Stratmann, *Corrosion Science* 43 (2001) 243–254.
- [40] G. Grundmeier, M. Brettmann, P. Thiemann, *Applied Surface Science* 217 (2003) 223–232.
- [41] R. Hausbrand, M. Stratmann, M. Rohwerder, *Steel Research International* 74 (2003) 453–458.
- [42] R. Hausbrand, M. Stratmann, M. Rohwerder, *Corrosion Science* 51 (2009) 2107–2114.
- [43] R.S. Jayasree, V.P.M. Pillai, V.U. Nayar, I. Odnevall, G. Keresztury, *Materials Chemistry and Physics* 99 (2006) 474–478.
- [44] A.R. Marder, *Progress in Materials Science* 45 (2000) 191–271.
- [45] T.H. Muster, I.S. Cole, *Corrosion Science* 46 (2004) 2319–2335.
- [46] T.H. Muster, A.K. Neufeld, I.S. Cole, *Corrosion Science* 46 (2004) 2337–2354.
- [47] A.K. Neufeld, I.S. Cole, A.M. Bond, S.A. Furman, *Corrosion Science* 44 (2002) 555–572.
- [48] W.R. Osorio, C.M.A. Freire, A. Garcia, *Revista De Metalurgia* (2005) 160–164.
- [49] W.R. Osorio, C.M. Freire, A. Garcia, *Materials Science and Engineering A* 402 (2005) 22–32.
- [50] W.R. Osorio, C.A. Siqueira, C.M.A. Freire, A. Garcia, *Revista De Metalurgia* (2005) 176–180.
- [51] R. Posner, G. Giza, R. Vlasak, G. Grundmeier, *Electrochimica Acta* 54 (2009) 4837–4843.
- [52] N.R. Short, S. Zhou, J.K. Dennis, *Surface & Coatings Technology* 79 (1996) 218–224.
- [53] X.G. Zhang, *Journal of the Electrochemical Society* 143 (1996) 1472–1484.
- [54] Y.H. Kim, C.Y. Rae, K.H. Kim, W.S. Chung, *Journal of the Electrochemical Society* 151 (2004) B319 – B324.
- [55] M. Giza, G. Grundmeier, *Plasma Processes and Polymers* 8 (2011) 607–616.
-

-
- [56] P. Volovitch, C. Allely, K. Ogle, *Corrosion Science* 51 (2009) 1251–1262.
- [57] R. Hausbrand, M. Rohwerder, M. Stratmann, C. Schwerdt, B. Schuhmacher, G. Grundmeier, *Proc. Galvatech* June, 2001, p.161.
- [58] B. Schuhmacher, W. Muschenborn, M. Stratmann, B. Schultrich, C.P. Klages, M. Kretschmer, U. Seyfert, F. Forster, H.J. Tiller, *Advanced Engineering Materials* 3 (2001) 681–689.
- [59] B. Schuhmacher, C. Schwerdt, U. Seyfert, O. Zimmer, *Surface & Coatings Technology* 163 (2003) 703–709.
- [60] R. Hausbrand, M. Stratmann, M. Rohwerder, *Journal of the Electrochemical Society* 155 (2008) C369–C379.
- [61] C. Fotea, J. Callaway, M.R. Alexander, *Surface and Interface Analysis* 38 (2006) 1363–1371.
- [62] M. Maxisch, P. Thissen, M. Giza, G. Grundmeier, *Langmuir* 27 (2011) 6042–6048.
- [63] M. Maxisch, C. Ebbert, B. Torun, N. Fink, T. de los Arcos, J. Lackmann, H.J. Maier, G. Grundmeier, *Applied Surface Science* 257 (2011) 2011–2018.
- [64] G. Grundmeier, M. Stratmann, *Applied Surface Science* 141 (1999) 43–56.
- [65] N.J. Shirtcliffe, M. Stratmann, G. Grundmeier, *Surface and Interface Analysis* 35 (2003) 799–804.
- [66] B.A. Kalin, V.L. Yakushin, V.I. Vasiliev, S.S. Tserevitinov, *Surface & Coatings Technology* 96 (1997) 110–116.
- [67] J.E. Svensson, L.G. Johansson, *Corrosion Science* 34 (1993) 721–740.
- [68] J. Kawafuku, J. Katoh, M. Toyama, K. Ilkeda, H. Nishimoto, H. Sato, in: *Proceedings of the 5th Automotive Corr. & Prevention Conference*, Michigan, United States (1991).
- [69] M. Morishita, K. Koyama, M. Murase, Y. Mori, *Isij International* 36 (1996) 714–719.
- [70] M. Morishita, K. Koyama, Y. Mori, *Isij International* 37 (1997) 55–58.
- [71] M. Morishita, K. Koyama, Y. Mori, *Materials Transactions, JIM* 38 (1997) 719–723.
- [72] T. Tsujimura, A. Komatsu, A. Andoh, *Proc. Galvatech* June, 2001, p. 145.
- [73] T. Ishikawa, M. Ueda, K. Kandori, T. Nakayama, *Corrosion Science* 49 (2007) 2547–2556.
- [74] W. Feitknecht, *Met. Corros.* (1947) 192.
- [75] W. Feitknecht, *Werkstoffe und Korrosion* (1955) 15.
- [76] W. Feitknecht, *Chem. Ind.* (1959) 1102.
- [77] A. Hugot–Le Goff, S. Joiret, B. Saidani, R. Wiart, *Journal of Electroanalytical Chemistry and Interfacial Electrochemistry* 263 (1989) 127–135.
- [78] M.C. Bernard, A. Hugot–Le Goff, D. Massinon, N. Phillips, *Corrosion Science* 35 (1993) 1339–1349.
- [79] T.C. Damen, S.P.S. Porto, B. Tell, *Physical Review* 142 (1966) 570–574.
- [80] O. Ozcan, K. Pohl, P. Keil, G. Grundmeier, *Electrochemistry Communications* 13 (2011) 837–839.
- [81] J.S. Fordyce, R.L. Baum, *Journal of Chemical Physics* 43 (1965) 843–846.
- [82] S.K. Sharma, M.D. Reed, *Journal of Inorganic and Nuclear Chemistry* 38 (1976) 1971–1972.
-

-
- [83] K.J. Cain, C.A. Melendres, V.A. Maroni, *Journal of the Electrochemical Society* 134 (1987) 519–524.
- [84] J. McBreen, W.E. O’Grady, 171st Meeting of the Electrochemical Society, Philadelphia, PA Extended Abstract No. 348 (1987) 511.
- [85] T. Wink, S.J. vanZuilen, A. Bult, W.P. vanBennekom, *Analyst* 122 (1997) R43–R50.
- [86] R. Luschtinetz, A.F. Oliveira, J. Frenzel, J.O. Joswig, G. Seifert, H.A. Duarte, *Surface Science* 602 (2008) 1347–1359.
- [87] K. Demidenok, V. Bocharova, M. Stamm, E. Jahne, H.J.P. Adler, A. Kiriya, *Langmuir* 23 (2007) 9287–9292.
- [88] A. Raman, M. Dubey, I. Gouzman, E.S. Gawalt, *Langmuir* 22 (2006) 6469–6472.
- [89] M. Textor, L. Ruiz, R. Hofer, A. Rossi, K. Feldman, G. Hahner, N.D. Spencer, *Langmuir* 16 (2000) 3257–3271.
- [90] B.R.A. Neves, M.E. Salmon, P.E. Russell, E.B. Troughton, *Langmuir* 17 (2001) 8193–8198.
- [91] H.Y. Nie, *Analytical Chemistry* 82 (2010) 3371–3376.
- [92] J.T. Woodward, A. Ulman, D.K. Schwartz, *Langmuir* 12 (1996) 3626–3629.
- [93] L. Forget, F. Wilwers, J. Delhalle, Z. Mekhalif, *Applied Surface Science* 205 (2003) 44–55.
- [94] E. Hoque, J.A. DeRose, P. Hoffmann, H.J. Mathieu, B. Bhushan, M. Cichomski, *Journal of Chemical Physics* 124 (2006) 174710.
- [95] B. Adolphi, E. Jahne, G. Busch, X.D. Cai, *Analytical and Bioanalytical Chemistry* 379 (2004) 646–652.
- [96] M. Eschner, R. Frenzel, F. Simon, D. Pleul, P. Uhlmann, H. Adler, *Macromolecular Symposia* 210 (2004) 77–84.
- [97] T.T. Foster, M.R. Alexander, G.J. Leggett, E. McAlpine, *Langmuir* 22 (2006) 9254–9259.
- [98] F. Sinapi, L. Forget, J. Delhalle, Z. Mekhalif, *Surface and Interface Analysis* 34 (2002) 148–154.
- [99] T. Hauffman, O. Blajiev, J. Snauwaert, C. van Haesendonck, A. Hubin, H. Terryn, *Langmuir* 24 (2008) 13450–13456.
- [100] F. Schreiber, *Progress in Surface Science* 65 (2000) 151–256.
- [101] A. Ulman, *Chemical Reviews* 96 (1996) 1533–1554.
- [102] I. Doudevski, D.K. Schwartz, *Applied Surface Science* 175 (2001) 17–26.
- [103] D.L. Allara, R.G. Nuzzo, *Langmuir* 1 (1985) 45–52.
- [104] E. Hoque, J.A. DeRose, G. Kulik, P. Hoffmann, H.J. Mathieu, B. Bhushan, *Journal of Physical Chemistry B* 110 (2006) 10855–10861.
- [105] D.L. Allara, *Biosensors & Bioelectronics* 10 (1995) 771–783.
- [106] P. Thissen, M. Valtiner, G. Grundmeier, *Langmuir* 26 (2010) 156–164.
- [107] J. van den Brand, P.C. Snijders, W.G. Sloof, H. Terryn, J.H.W. de Wit, *Journal of Physical Chemistry B* 108 (2004) 6017–6024.
- [108] J. van den Brand, S. Van Gils, P.C.J. Beentjes, H. Terryn, V. Sivel, J.H.W. de Wit, *Progress in Organic Coatings* 51 (2004) 339–350.
- [109] R. Quinones, E.S. Gawalt, *Langmuir* 23 (2007) 10123–10130.
-

-
- [110] E.S. Gawalt, M.J. Avaltroni, N. Koch, J. Schwartz, *Langmuir* 17 (2001) 5736–5738.
- [111] C. Bram, C. Jung, M. Stratmann, *Fresenius Journal of Analytical Chemistry* 358 (1997) 108–111.
- [112] N. Tillman, A. Ulman, J.S. Schildkraut, T.L. Penner, *Journal of the American Chemical Society* 110 (1988) 6136–6144.
- [113] A.J. Kinloch, K.T. Tan, J.F. Watts, *Journal of Adhesion* 82 (2006) 1117–1132.
- [114] E. Jaehne, S. Oberoi, H.–J.P. Adler, *Progress in Organic Coatings* 61 (2008) 211–223.
- [115] S. Oberoi, E. Jahne, H.J.P. Adler, *Macromolecular Symposia* 217 (2004) 147–159.
- [116] K.S. Midwood, M.D. Carolus, M.P. Danahy, J.E. Schwarzbauer, J. Schwartz, *Langmuir* 20 (2004) 5501–5505.
- [117] J. Pahnke, J. Ruhe, *Macromolecular Rapid Communications* 25 (2004) 1396–1401.
- [118] F. Awaja, M. Gilbert, G. Kelly, B. Fox, P.J. Pigram, *Progress in Polymer Science* 34 (2009) 948–968.
- [119] D.E. Packham, *Journal of Adhesion* 84 (2008) 240–255.
- [120] J.W. McBain, D.G. Hopkins, *The Journal of Physical Chemistry* 29 (1924) 188–204.
- [121] O. Negele, W. Funke, *Progress in Organic Coatings* 28 (1996) 285–289.
- [122] H. Leidheiser, W. Funke, *Journal of the Oil & Colour Chemists Association* 70 (1987) 121–132.
- [123] W. Funke, *Journal of the Oil & Colour Chemists Association* 62 (1979) 63–67.
- [124] J. Wielant, R. Posner, R. Hausbrand, G. Grundmeier, H. Terryn, *Surface and Interface Analysis* 42 (2010) 1005–1009.
- [125] J. Wielant, R. Posner, R. Hausbrand, G. Grundmeier, H. Terryn, *Corrosion Science* 51 (2009) 1664–1670.
- [126] J. Wielant, R. Posner, R. Hausbrand, G. Grundmeier, H. Terryn, *Surface and Interface Analysis* 42 (2010) 1005–1009.
- [127] M. Santa, R. Posner, G. Grundmeier, *Journal of the Electrochemical Society* 158 (2011) C36–C41.
- [128] R. Posner, M. Santa, G. Grundmeier, *Journal of the Electrochemical Society* 158 (2011) C29–C35.
- [129] R. Posner, K. Wapner, S. Amthor, K.J. Roschmann, G. Grundmeier, *Corrosion Science* 52 (2010) 37–44.
- [130] R. Posner, K. Wapner, M. Stratmann, G. Grundmeier, *Electrochimica Acta* 54 (2009) 891–899.
- [131] G. Grundmeier, R. Posner, *Galvanotechnik* (2010) 1253–1255.
- [132] K. Wapner, G. Grundmeier, *Advanced Engineering Materials* 6 (2004) 163–167.
- [133] K. Wapner, Ph. D. Thesis, Ruhr–Universität Bochum, Bochum, 2006.
- [134] A.J. Kinloch, *Journal of Materials Science* 17 (1982) 617–651.
- [135] A.J. Kinloch, *Durability of structural adhesives*, Applied Science Publishers, London and New York, 1983.
- [136] A.J. Kinloch, L.S. Welch, H.E. Bishop, *The Journal of Adhesion* 16 (1984) 165–177.
- [137] A.J. Kinloch, *Surface and Interface Analysis* 8 (1986) 227–227.
-

-
- [138] A.J. Kinloch, C.C. Lau, J.G. Williams, *International Journal of Fracture* 66 (1994) 45–70.
- [139] A.J. Kinloch, *Adhesion and Science Engineering 1: The Mechanics of Adhesion*, Elsevier, 2002.
- [140] M.R. Bowditch, *International Journal of Adhesion and Adhesives* 16 (1996) 73–79.
- [141] E.P. O'Brien, S.L. Case, T.C. Ward, *The Journal of Adhesion* 81 (2005) 41–58.
- [142] J.F. Watts, R.A. Blunden, T.J. Hall, *Surface and Interface Analysis* 16 (1990) 227–235.
- [143] M. Yu, J. Hwang, T.J. Deming, *Journal of the American Chemical Society* 121 (1999) 5825–5826.
- [144] D.C. Hansen, S.C. Dexter, J.H. Waite, *Corrosion Science* 37 (1995) 1423–1441.
- [145] D.R. Lefebvre, P.R. Elliker, K.M. Takahashi, V.R. Raju, M.L. Kaplan, *Journal of Adhesion Science and Technology* 14 (2000) 925–937.
- [146] O. Ozcan, K. Pohl, B. Ozkaya, G. Grundmeier, *The Journal of Adhesion* 89 (2013) 1–12.
- [147] K. Wapner, M. Stratmann, G. Grundmeier, *Electrochimica Acta* 51 (2006) 3303–3315.
- [148] K. Wapner, B. Schoenberger, A. Stratmann, G. Grundmeier, *Journal of the Electrochemical Society* 152 (2005) E114–E122.
- [149] J. Wielant, R. Posner, G. Grundmeier, H. Terryn, *Journal of Physical Chemistry C* 112 (2008) 12951–12957.
- [150] R. Posner, G. Giza, M. Marazita, G. Grundmeier, *Corrosion Science* 52 (2010) 1838–1846.
- [151] R. Posner, M. Marazita, S. Amthor, K.J. Roschmann, G. Grundmeier, *Corrosion Science* 52 (2010) 754–760.
- [152] R. Posner, Ph. D. Thesis, Universität Paderborn, Paderborn, 2009.
- [153] R. Posner, P.E. Sundell, T. Bergman, P. Roose, M. Heylen, G. Grundmeier, P. Keil, *Journal of the Electrochemical Society* 158 (2011) C185–C193.
- [154] A. Leng, H. Streckel, M. Stratmann, *Corrosion Science* 41 (1999) 547–578.
- [155] G. Grundmeier, W. Schmidt, M. Stratmann, *Electrochimica Acta* 45 (2000) 2515–2533.
- [156] A. Leng, H. Streckel, K. Hofmann, M. Stratmann, *Corrosion Science* 41 (1999) 599–620.
- [157] A. Leng, H. Streckel, M. Stratmann, *Corrosion Science* 41 (1999) 579–597.
- [158] R. Posner, T. Titz, K. Wapner, M. Stratmann, G. Grundmeier, *Electrochimica Acta* 54 (2009) 900–908.
- [159] M. Santa, R. Posner, G. Grundmeier, *Journal of Electroanalytical Chemistry* 643 (2010) 94–101.
- [160] W.E. Smith, G. Dent, *Modern Raman Spectroscopy – A Practical Approach*, John Wiley & Sons, Ltd, 2005.
- [161] M. Hesse, H. Meier, B. Zeeh, *Spektroskopische Methoden in der organischen Chemie*, Georg Thieme Verlag, Stuttgart, 1991.
- [162] G. Wedler, *Lehrbuch der physikalischen Chemie*, Wiley VCH, 1997.
- [163] D. Meschede, *Gerthsen Physik*, Springer Verlag, Germany, Berlin, 2004.
- [164] M. Maxisch, Ph. D. Thesis, Universität Paderborn, Paderborn, 2012.
- [165] H. Günzler, H.U. Gremlich, *IR-Spektroskopie: Eine Einführung*, Wiley–VCH, Germany, 2003.
- [166] R.G. Greenler, *The Journal of Chemical Physics* (1966) 310–315.
-

-
- [167] J.F. Watts, J. Wolstenholme, *An Introduction to Surface Analysis by XPS and AES*, John Wiley & Sons, Ltd, 2003.
- [168] J.F. Moulder, W.F. Stickle, P.E. Sobol, K.D. Bomben, *Handbook of X-ray Photoelectron Spectroscopy*, Physical Electronics, Inc., USA, 1995.
- [169] M. Stratmann, H. Streckel, *Ber. Bunsenges. Phys. Chemie* 92 (1988) 1244.
- [170] M. Santa, Ph. D. Thesis, Universität Paderborn, Paderborn, 2010.
- [171] M. Stratmann, H. Streckel, R. Feser, *Corrosion Science* 32 (1991) 467–470.
- [172] Ö. Özkanat, B. Salgin, M. Rohwerder, J.M.C. Mol, J.H.W. de Wit, H. Terryn, *The Journal of Physical Chemistry C* 116 (2012) 1805–1811.
- [173] F. Di Quarto, M.C. Romano, M. Santamaria, S. Piazza, C. Sunseri.
- [174] C.H. Hamann, W. Vielstich, *Electrochemistry*, 2004.
- [175] A. Losch, J.W. Schultze, H.D. Speckmann, *Applied Surface Science* 52 (1991) 29–38.
- [176] E. Klusmann, U. König, J.W. Schultze, *Materials and Corrosion* 46 (1995) 83–91.
- [177] Ö. Özcan, Ph. D. Thesis, Ruhr–Universität Bochum, Bochum, 2010.
- [178] M. Rohwerder, F. Turcu, *Electrochimica Acta* 53 (2007) 290–299.
- [179] K. Oura, V.G. Lifshits, A.A. Saranin, A.V. Zotov, M. Katayama, *Surface Science, An Introduction*, Springer Berlin – Heidelberg, 2003.
- [180] N.T. Correia, J.J.M. Ramos, B.J.V. Saramago, J.C.G. Calado, *Journal of Colloid and Interface Science* 189 (1997) 361–369.
- [181] E. Boehm–Courjault, F. Gonzales, A. Jacot, F. Kohler, A. Mariaux, C. Niederberger, M.A. Salgado–Ordorica, M. Rappaz, *Journal of Microscopy* 233 (2009) 160–169.
- [182] R. Parisot, S. Forest, A. Pineau, F. Grillon, X. Demonet, J.M. Maigne, *Metallurgical and Materials Transactions a–Physical Metallurgy and Materials Science* 35A (2004) 797–811.
- [183] Y.H. Zhu, W.B. Lee, C.F. Yeung, T.M. Yue, *Materials Characterization* 46 (2001) 19–23.
- [184] S.O. Klemm, J.–C. Schauer, B. Schuhmacher, A.W. Hassel, *Electrochimica Acta* 56 (2011) 9627–9636.
- [185] M. Arndt, J. Duchoslav, H. Itani, G. Hesser, C.K. Riener, G. Angeli, K. Preis, D. Stifter, K. Hingerl, *Analytical and Bioanalytical Chemistry* 403 (2012) 651–661.
- [186] J. Sullivan, S. Mehraban, J. Elvins, *Corrosion Science* 53 (2011) 2208–2215.
- [187] K. Pohl, J. Otte, P. Thissen, M. Giza, M. Maxisch, B. Schuhmacher, G. Grundmeier, *Surface & Coatings Technology* 218 (2013) 99–107.
- [188] K. Nikolov, N. Samann, B. Schuhmacher, *Plasma Processes and Polymers* 4 (2007) S821–S825.
- [189] M.R. Alexander, G.E. Thompson, G. Beamson, *Surface and Interface Analysis* 29 (2000) 468–477.
- [190] B. Schinking, R. Petzold, H.J. Tiller, G. Grundmeier, *Applied Surface Science* 179 (2001) 79–87.
- [191] D.M. Spori, N.V. Venkataraman, S.G.P. Tosatti, F. Durmaz, N.D. Spencer, S. Zurcher, *Langmuir* 23 (2007) 8053–8060.
- [192] H.L. Snyder, B.T. Smtih, T.P. Parr, R.M. Martin, *Chemical Physics* 65 (1982) 397–406.
-

- [193] R.A. Macphail, H.L. Strauss, R.G. Snyder, C.A. Elliger, *Journal of Physical Chemistry* 88 (1984) 334–341.
- [194] R.G. Nuzzo, L.H. Dubois, D.L. Allara, *Journal of the American Chemical Society* 112 (1990) 558–569.
- [195] D.K. Schwartz, *Annual Review of Physical Chemistry* 52 (2001) 107–137.
- [196] M. Maxisch, C. Ebbert, B. Torun, N. Fink, T. de los Arcos, J. Lackmann, H.J. Maier, G. Grundmeier, *Applied Surface Science* 257 (2011) 2011–2018.
- [197] F. Parmigiani, L.E. Depero, *Structural Chemistry* 5 (1994) 117–122.
- [198] K. Pohl, O. Ozcan, M. Giza, B. Schuhmacher, G. Grundmeier, submitted to *International Journal of Adhesion and Adhesives*.
- [199] J. Raacke, M. Giza, G. Grundmeier, *Surface & Coatings Technology* 200 (2005) 280–283.
- [200] CasaXPS Version 2314. C.S. Ltd., 2005, www.casaxps.com.
- [201] E. Juzeliunas, A. Sudavicius, K. Jüttner, W. Fürbeth, *Electrochemistry Communications* 5 (2003) 154–158.
- [202] G. Back, A. Nazarov, D. Thierry, *Corrosion* 61 (2005) 951–960.
- [203] P. Taheri, K. Pohl, G. Grundmeier, J.R. Flores, F. Hannour, J.H.W. de Wit, J.M.C. Mol, H. Terryn, *The Journal of Physical Chemistry C* 117 (2013) 1712–1721.
- [204] K.P. Battjes, A.M. Barolo, P. Dreyfuss, *Journal of Adhesion Science and Technology* 5 (1991) 785–799.

Abbreviations and symbols

Abbreviations

AC	alternating current
AES	Auger electron spectroscopy
AFM	atomic force microscopy
AOI	angle of incidence
APPA	3-aminopropylphosphonic acid
at.%	atomic percentage
BE	binding energy
CCD	charge-coupled device
CV	cyclic voltammetry
DC	direct current/
DC mode	dynamic contact mode
EBSD	electron backscatter diffraction
EDX	electron dispersive X-ray
FIB	Focus ion beam
FT-IR	Fourier transform infrared spectroscopy
FT-IRRAS	Fourier transform infrared reflection absorption spectroscopy
FWHM	full width at half maximum
IC	ion chromatography
Mag	Magnitude
MBT	2-mercaptobenzothiazole
MCT	mercury cadmium telluride detector
MIR-DTGS	mid-infrared deuterated triglycine sulfate detector
OCP	open circuit potential
ODPA	octadecylphosphonic acid
p.a.	pro analysis
PM-IRRAS	polarization modulated IRRAS
ppm	parts per million
PVD	physical vapour deposition
r.h.	relative humidity
SAM	self-assembled monolayer
sccm	standard cubic centimeter per minute
SEM	scanning electron microscopy
SERS	surface enhanced Raman spectroscopy
SHC	strip hollow cathode
SKP	scanning Kelvin probe
SKPFM	scanning Kelvin probe force microscopy
THF	tetrahydrofuran
Tof-SIMS	Time-of-flight secondary ion mass spectrometry
UHV	ultra-high vacuum
WD	work distance
wt%	weight percent
XPS	X-ray photoelectron spectroscopy
Z	hot-dipped galvanized steel, coating: Zn + <0.5wt% Al

ZE	electrogalvanized steel
ZM	hot-dipped galvanized steel, coating: Zn + 1–2wt% Mg +1–2wt% Al

Symbols

A	frontal tip area of SKP needle
α	angle between alkyl chain axis and surface normal or polarisability
c	concentration of illuminated material
\bar{c}	light speed
C	capacitance
γ_{SG}	solid/gas interface tension
γ_{SL}	solid/liquid interface tension
γ_{LG}	liquid/gas interface tension
d_0	Distance between sample surface and tip
dx	length of illuminated material
E	electromagnetic field
E_p	electromagnetic field of parallel polarized light
E_s	electromagnetic field of perpendicular polarized light
E_{bind}	binding energy
E_{kin}	kinetic energy
ϵ	Dielectric constant
ϵ_0	Permittivity of free space
F_e	electric force
θ	contact angle
I_{CH_2}/I_{CH_3}	intensity of the valence vibration band
J	photon flux
K	term includes all the instrumental factors
k	adsorption factor or force constant
λ	wavelength or electron attenuation length
μ	dipole moment or reduced mass
ν_0	frequency of the electromagnetic wave
$\bar{\nu}$	wavenumber
n	number of methylene groups
Q	Charge
ρ	concentration of atom or ion in solid
σ	cross section for photoelectron production
t	time
V	Voltage
ϕ_{sample}	electron work function of the sample
$\Delta\phi_S^{Ref}$	work function difference between reference and sample
W_{cap}	electric energy stored in the capacitor
ω	tip vibration frequency

List of Figures

Figure 1.1: Schematic overview of the scientific approach followed in the present study.....	2
Figure 2.1: General overview of solid corrosion products on pure zinc observed with different electrolyte under atmospheric conditions and long-time exposure.	5
Figure 2.2: Stability diagram of zinc corrosion products taken from Reference [21].....	9
Figure 2.3: Scheme of the corrosive reaction in 0.5 M NaCl and the formation of possible corrosion products [74–76].	10
Figure 2.4: Schematic of mono- and bi-dentate binding model developed in the literature [8; 104; 110].....	19
Figure 2.5: Schematic of the electrochemical reaction during the cathodic delamination process.....	21
Figure 2.6: Scheme of the backside-SERS setup for the in-situ investigation of ion transport processes along the sample surface according to Reference [159]	23
Figure 3.1: Schematic of the Rayleigh and Raman scattering process [160].	25
Figure 3.2: Schematic drawing of IRRRA spectroscopy as a function of the polarization state taken from Reference [164].	28
Figure 3.3: Schematic of IRRRA spectroscopy taken from Reference [164].	28
Figure 3.4: Reflection curve of p-polarized light as a function of the AOI taken from Reference [164].	29
Figure 3.5: Schematic of the Kelvin probe setup [152; 170].	31
Figure 3.6: Scheme of the bulk band structure of the passive oxides of zinc, Zn ₂ Mg, magnesium and aluminum. Valence band position E_V and conduction band position E_C are indicated with a solid line. Fermi levels E_F are indicated with dotted line. The positions of the bands in the electronic structure were taken from reference [60]. For the positions of the conduction bandedge of aluminum, Kelvin Probe measurements of Özkanat et al. [172] were used and the band gaps of the passive layer were taken from Reference [173], thus providing the position of the valence band. The valence band position of Zn ₂ Mg and aluminum is indicated by a dotted line.	32
Figure 3.7: Potential-time curve at the working electrode in the cyclic voltammetry [174]. ..	33
Figure 3.8: Schematic setup of scanning Kelvin probe force microscopy (SKPFM) [177].	34
Figure 3.9: Schematic setup of atomic force microscopy in contact mode.....	37
Figure 3.10: Contact angle between liquid drop and solid surface.	38

Figure 4.1: Scheme of the applied Raman spectroscopic setup for the in-situ investigation of corrosion processes.....	41
Figure 4.2: SEM analysis of hot-dipped galvanized steel surface, SEM parameters: WD = 4.9 mm and EHT = 20.0 kV, (A) Mag = 100x, Detector = SE 2, (B, C) Mag = 1kx and (D, E) Mag = 10kx, (A, C) Detector = SE 2 and (C, E) InLens.	42
Figure 4.3: SEM image 70° tilted and EBSD grain orientation mapping, red frame area of EBSD image and the inverse pole figure.	43
Figure 4.4: SEM analysis (top) and EDX mappings of local Al, O, Zn and C content of hot-dipped galvanized steel surface. SEM parameters: Mag = 1kx, WD = 4.8 mm, Detector = SE 2, EHT = 20.0 kV.....	45
Figure 4.5: SEM analysis and EDX analysis of hot-dipped galvanized steel surface, SEM parameters: Mag = 8kx, WD = 4.8 mm, Detector = SE 2, EHT = 20.0 kV.....	46
Figure 4.6: AFM (A, C) and SKFPM (B, D) images of a grain, first row (A, B) 80 nm by 80 nm scan area, second row 30 nm by 30 nm scan area, closer view in the area marked with the red frame, topography (A, C) and potential (B, D).....	48
Figure 4.7: First row: microscopic picture. Second row: AFM (left) and SKFPM (right) image of a grain boundary, topography (left) and potential (right). Last row: SEM analysis (left) and EDX mappings of Al and O content at the before measured SKPFM area. SEM parameters: Mag = 1kx, WD = 4.8 mm, Detector = SE 2, EHT = 20.0 kV.	49
Figure 4.8: (A, C, E and G): Microscopic images of the zinc surface at 0, 20, 40 and 60 min related to the exposure to 0.05 M NaCl at pH 7. (B, D, F and H): Raman images at 430 cm^{-1} . (A and B): 0 min; (C and D): 20 min; (E and F): 40 min; (G and H): 60 min.	50
Figure 4.9: Left: Open circuit potential of the zinc surface measured during the experiment. Right: Comparison of the Raman spectra of the zinc surface at 0, 30 and 60 min related to the exposure to 0.05 M NaCl at pH7.....	51
Figure 4.10: Microscopic images of the zinc surface at 0, 20, 40, 60, 80 and 100 min related to the exposure to 0.05 M NaCl and 0.5 ml/min flow at pH 7. : measurement points of the Raman spectra.....	52
Figure 4.11: Top: Open circuit potential measured during the experiment. Raman spectra at 0, 20, 40, 60, 80 and 100 min related to the exposure to 0.05 M NaCl and 0.5 ml/min flow at pH 7.	53
Figure 4.12: Microscopic images of the zinc surface at 0, 20, 40, 60, 80 and 100 min related to the exposure to 0.05 M NaCl and 0.5 ml/min flow at pH 3. : measurement points of the Raman spectra.....	54
Figure 4.13: Top: Open circuit potential measured during the experiment. Raman spectra at 0, 20, 40, 60, 80 and 100 min related to the exposure to 0.05 M NaCl and 0.5 ml/min flow at pH 3.	55

Figure 4.14: Microscopic images at 0, 20, 40, 60, 80 and 100 min related to the exposure to 0.05 M NaCl and 0.5 ml/min flow at pH 11. : measurement points of the Raman spectra. .. 56

Figure 4.15: Top: Open circuit potential measured during the experiment. Raman spectra at 0, 20, 40, 60, 80 and 100 min related to the exposure to 0.05 M NaCl and 0.5 ml/min flow at pH 11. 57

Figure 5.1: Top: SEM analysis of zinc magnesium aluminum coated steel surface. SEM parameters: Mag = 5kx, WD = 9 mm, Detector = InLens, EHT = 8.0 kV. Bottom: SEM analysis of zinc magnesium aluminum coated steel surface, SEM parameters: Mag = 20kx, WD = 9 mm, Detector = InLens, EHT = 10.0 kV. 61

Figure 5.2: First row: SEM analysis (left) and EDX mappings of local Mg, O, Al and Zn content of hot-dipped galvanized steel surface. SEM parameters: Mag = 5kx, WD = 5 mm, Detector = SE 2, EHT = 20.0 kV. 62

Figure 5.3: Microscopic images of Zn–Mg–Al alloy coated steel at 0, 30, 60, 90, 120 and 150 min related to the exposure to 0.05 M NaCl at pH7. 63

Figure 5.4: Left: Open circuit potential of the zinc magnesium surface measured during the experiment. Right: Comparison of the Raman spectra of the zinc magnesium surface at 0, 30, 60, 90, 120 and 150 min related to the exposure to 0.05 M NaCl at pH7. 64

Figure 5.5: Microscopic images at 0, 40, 80 and 120 min related to the exposure to 0.05 M NaCl and 0.5 ml/min flow at pH 3. : measurement points of the Raman spectra. 65

Figure 5.6: Top: Open circuit potential taken during the experiment. Raman spectra at 0, 40, 80 and 120 min related to the exposure to 0.05 M NaCl and 0.5 ml/min flow at pH 3. 66

Figure 5.7: Microscopic images at 0, 40, 80 and 120 min related to the exposure to 0.05 M NaCl and 0.5 ml/min flow at pH 7. : measurement points of the Raman spectra. 67

Figure 5.8: Top: Open circuit potential taken during the experiment. Raman spectra at 0, 40, 80 and 120 min related to the exposure to 0.05 M NaCl and 0.5 ml/min flow at pH 7. 68

Figure 5.9: Microscopic images at 0, 40, 80 and 120 min related to the exposure to 0.05 M NaCl and 0.5 ml/min flow at pH 11. : measurement points of the Raman spectra. 69

Figure 5.10: Top: Open circuit potential taken during the experiment. Raman spectra at 0, 40, 80 and 120 min related to the exposure to 0.05 M NaCl and 0.5 ml/min flow at pH 11. . 70

Figure 6.1: SEM analysis (top, left) and EDX mappings of the cross section prepared by FIB of zinc coated steel substrate. EDX mappings of local C, O, Al, Fe and Zn content. 74

Figure 6.2: SEM analysis (top, left) and EDX mappings of the cross section prepared by FIB of zinc magnesium coated steel substrate. EDX mappings of local C, O, Zn, Al, Mg and Fe content. 75

- Figure 6.3: Microscopic images of Zn–Al/ Fe interface at 0, 30,60, 90 and 120 min related to exposure to 0.05 M NaCl and 0.5 ml/min flow. Left column: microscopic images. Right column: Raman images at 430 cm^{-1} 76
- Figure 6.4: Left: Open circuit potential of the iron/zinc cut edge measured during the experiment. Right: Comparison of the Raman spectra of the zinc surface at 0, 30, 60, 90 and 120 min related to the exposure to 0.05 M NaCl at pH7..... 77
- Figure 6.5: Images of Zn–Mg–Al/Fe interface at 0, 30, 60 and 90 min related to exposure to 0.05 M NaCl and 0.5 ml/min flow. Left column: Microscopic images. Right column: Raman images at 430 cm^{-1} 78
- Figure 6.6: Left: Open circuit potential of the iron/zinc magnesium cut edge measured during the experiment. Right: Comparison of the Raman spectra of the zinc surface at 0, 30, 60 and 90 min related to the exposure to 0.05 M NaCl at pH7..... 79
- Figure 7.1: XPS survey spectra of polished (A), Ar/H₂ plasma (B) and Ar/H₂ + O₂ plasma treated Zn–Mg–Al surfaces. 83
- Figure 7.2: O1s detail spectra of (A) a polished Zn–Mg–Al alloy surface, (B) a 60 s Ar/H₂ plasma modified Zn–Mg–Al alloy surface and (C) a subsequent 60 s O₂ plasma modified Zn–Mg–Al alloy surface. 85
- Figure 7.3: Atomic ratio of Al/Zn and Mg/Zn as a function of the surface condition..... 86
- Figure 7.4: ZnLMM detail spectra of (A) a polished Zn–Mg–Al alloy surface, (B) a 60 s Ar/H₂ plasma modified Zn–Mg–Al alloy surface and (C) a subsequent 60 s O₂ plasma modified Zn–Mg–Al alloy surface. 88
- Figure 7.5: Cyclic voltammograms measured in borate buffer of a polished Zn–Mg–Al alloy surface (A), after 60 s Ar/H₂ plasma modification (B) and after subsequent 60 s O₂ plasma modification (C). 89
- Figure 7.6: Comparison of the last cyclic voltammogram measured in borate buffer of a polished Zn–Mg–Al alloy surface (solid line), after 60 s Ar/H₂ plasma modification (dotted line) and after subsequent 60 s O₂ plasma modification (dashed line). 90
- Figure 7.7: A and B: PM–IRRAS of Zn–Mg–Al alloy polished and after plasma modifications immersed in 10^{-3} mol/l ODPA. All spectra are referenced to the surface spectra taken before ODPA adsorption..... 92
- Figure 7.8: A, C and E: XPS P 2p detail spectra of Zn–Mg–Al alloy polished and after plasma modifications immersed in 10^{-3} mol/l ethanolic ODPA solution. B, D and F: XPS O 1 s spectra of samples pretreated as above and immersed in 10^{-3} mol/l ODPA. First row (A and B): samples were polished. Second row (C and D): samples were modified via Ar/H₂ plasma. Third row (E and F): samples were treated in O₂ plasma subsequently..... 93
- Figure 7.9: Water contact angle of polished and plasma treated Zn–Mg–Al alloy coated with ODPA versus the number of immersion cycles in water. The samples were immersed in

water for 10 min in each case and afterwards dried in a stream of nitrogen. The measurements were accomplished with three different states of the alloy surface: the polished surface (circle), the Ar/H₂ plasma treated surface (diamond) and the subsequently O₂ plasma treated surface (cross). 97

Figure 7.10: Cyclic voltammograms measured in borate buffer of ODPA monolayer covered samples; a polished Zn–Mg–Al alloy surface (A), after 60 s Ar/H₂ plasma modification (B) and after subsequent 60 s O₂ plasma modification (C). 98

Figure 7.11: Comparison of the fourth cyclic voltammogram measured in borate buffer of ODPA monolayer covered samples; a polished Zn–Mg–Al alloy surface (solid line), after 60 s Ar/H₂ plasma modification (dotted line) and after subsequent 60 s O₂ plasma modification (dashed line). 99

Figure 8.1: XPS O1s detail spectra of (A) as-cleaned, (B) Ar plasma and (C) Ar/O₂ plasma treated ZM surfaces. 106

Figure 8.2: Atomic ratio of Mg, Al and Zn to sum of metal concentration on the surface as a function of the surface condition. 107

Figure 8.3: SKP potential profile of a Zn–Mg–Al sample half treated with a) Ar– and b) Ar/O₂– plasma treated in dry atmosphere (< 10% r.h.) 108

Figure 8.4: FT–IRRA difference spectra of (A) solvent cleaned, (B) Ar plasma and (C) Ar/O₂ plasma treated ZM surfaces (the difference spectra has been calculated by taking as-cleaned (for A), Ar plasma treated (for B) and Ar/O₂ (for C) plasma treated ZM surfaces as reference). 109

Figure 8.5: (A), (C) and (E): XPS C1s detail spectra of ZM as-cleaned and after plasma modifications. (B), (D) and (F): XPS C1s spectra of samples pretreated as above and immersed in 10⁻³ M aqueous APPA solution. First row ((A) and (B)): solvent cleaned samples. Second row ((C) and (D)): samples were Ar plasma treated. Third row ((E) and (F)): samples were activated via Ar/O₂ plasma. 110

Figure 8.6: (A), (C) and (E): XPS P2s detail spectra of ZM as-cleaned and after plasma modifications immersed in 10⁻³ M aqueous APPA solution. (B), (D) and (F): XPS N1s spectra of samples pretreated as above and immersed in 10⁻³ M APPA. First row ((A) and (B)): solvent cleaned samples. Second row ((C) and (D)): samples were Ar plasma treated. Third row ((E) and (F)): samples were activated via Ar/O₂ plasma. 111

Figure 8.7: Peel forces measured in humid atmosphere of the native and plasma treated surfaces with and without APPA layer coated with epoxy amine resin. 114

List of Tables

Table 2.1: Composition of corrosion products on Zn, Zn–Mg, and Mg contaminated with chloride after exposure to humid air [17].	7
Table 2.2: Corrosion products observed during in–situ corrosion experiments in chloride containing environment.	12
Table 2.3: Peak position and assignment to corrosion products observed during in–situ corrosion by Raman spectroscopy.	14
Table 4.1: Composition of certain points measured with EDX and assigned in Figure 4.5.	46
Table 7.1: Atomic composition (at%) as analyzed by XPS for a polished, Ar–plasma reduced and plasma oxidized Zn–Mg–Al alloy.	84
Table 7.2: Atomic composition (at%) of ODPa covered samples analyzed by XPS.	95
Table 8.1: Atomic composition (at%) as analyzed by XPS at 60° for native, Ar plasma and Ar/O ₂ plasma treated ZM surfaces.	105
Table 8.2: Atomic composition (at.%) of APPA covered samples analyzed by XPS.	112

List of Publications

- [1] B. Lange, R. Posner, K. Pohl, C. Thierfelder, G. Grundmeier, S. Blankenburg and W.G. Schmidt; Water adsorption on hydrogenated Si(111) surfaces, *Surface Science* 603 (2009) 60–64.
- [2] O. Ozcan, K. Pohl, P. Keil, G. Grundmeier; Effect of hydrogen and oxygen plasma treatments on the electrical and electrochemical properties of zinc oxide nanorod films on zinc substrates, *Electrochemistry Communications* 13 (2011) 837–839.
- [3] P. Lammel, L.D. Rafailovic, M. Kolb, K. Pohl, A.H. Whitehead, G. Grundmeier, B. Gollas; Analysis of rain erosion behaviour of electroplated nickel–tungsten alloys, *Surface & Coatings Technology* 206 (2012) 2545–2551.
- [4] O. Ozcan, K. Pohl, B. Ozkaya, G. Grundmeier; Molecular studies of adhesion and de-adhesion on ZnO nanorod film covered metals, *The Journal of Adhesion* 89 (2013) 128–139.
- [5] K. Pohl, J. Otte, P. Thissen, M. Giza, M. Maxisch, B. Schuhmacher, G. Grundmeier; Adsorption, Self-Assembly Stability of Organophosphonic Acid Monolayers on Plasma Modified Zn–Mg–Al Alloy Surfaces, *Surface & Coatings Technology* (2013), DOI 10.1016/j.surfcoat.2012.12.035
- [6] P. Taheri, K. Pohl, G. Grundmeier, J.R. Flores, F. Hannour, J.H.W. de Wit, J.M.C. Mol, H. Terryn; Effects of surface treatment and carboxylic acid and anhydride molecular dipole moments on the Volta potential values of zinc surfaces, *The Journal of Physical Chemistry C* 117 (2013) 1712–1721.
- [7] K. Pohl, O. Ozcan, M. Giza, B. Schuhmacher, G. Grundmeier; Surface chemistry and adhesive properties of plasma modified ZnMgAl – alloy coatings, submitted to *International Journal of Adhesion and Adhesive*.
- [8] O. Ozcan, K. Pohl, G. Grundmeier; Corrosion protection of hot-dipped galvanised steel by means of ZnO nanorod films, submitted to *Corrosion Science*.
- [9] O. Ozcan, K. Pohl, C. Müller, G. Grundmeier; Synthesis and characterization of ZnO nanostructures on hot-dipped galvanized steel, submitted to *Thin Film Solids*.
- [10] K. Pohl, M. Voigt, G. Grundmeier; Corrosion resistance and adhesion properties of chemically etched ZnMgAl alloy, *Corrosion Science*, in preparation

Oral presentations

K. Pohl, M. Santa, R. Posner, M. Giza, G. Grundmeier, ECASIA 2010 – 04.–9.09.2011 Cardiff, Wales, UK

K. Pohl, O. Ozcan, G. Grundmeier, MRS Fall 2011 – 28.11.–02.12.2011 Boston, MA, USA

K. Pohl, T. Niendorf, O. Ozcan, G. Grundmeier, Gordon Research Seminar for Aqueous Corrosion 2012 07.–08.07.2012, New London, NH, USA (invited talk)

K. Pohl, O. Ozcan, M. Giza, G. Grundmeier, EUROCORR 2012 – 09.–13.09.2012, Istanbul, Turkey

K. Pohl, O. Ozcan, M. Giza, G. Grundmeier, Electrochemistry 2012 – 17.–19.09.2012 Munich, Germany

Poster presentations

K. Pohl, M. Santa, R. Posner, G. Grundmeier, Gordon Research Seminar for Aqueous Corrosion 2010 24.–25.07.2010, New London, NH, USA

K. Pohl, M. Santa, R. Posner, G. Grundmeier, Gordon Research Conference for Aqueous Corrosion 2010 25.–30.07.2010, New London, NH, USA

K. Pohl, T. Niendorf, O. Ozcan, G. Grundmeier, Gordon Research Conference for Aqueous Corrosion 2012 08.–13.07.2012, New London, NH, USA

Curriculum Vitae

PERSONAL INFORMATION

- Name: Katharina Pohl
- Date of birth: August 15th, 1984
- Place of birth: Nürtingen, Germany

EDUCATION

PhD studies

06/2009 – present *Universität Paderborn*

- PhD student in the Group of Prof. Guido Grundmeier in the Department for Technical and Macromolecular Chemistry
- Start of PhD (06.2009 – 12.2010) at Max–Planck–Institut für Eisenforschung within Christian Doppler Labor für Polymer/Metall–Grenzfläche

11/2008 – 05/2009 Cooperation: *Zentrum für Brennstoffzellentechnik, Duisburg, Germany and Heinrich–Heine–Universität Düsseldorf*

- Diplom thesis: Degradation analysis of proton exchange membrane fuel cell

University

10/2004 – 05/2009 *Heinrich–Heine–Universität Düsseldorf*

- Diploma degree in chemistry

School

2004 *Humboldtgynasium, Solingen*

- Abitur

ADDITIONAL WORK EXPERIENCE

11/2008 – 04/2009 Heinrich–Heine Universität, Düsseldorf, Germany

04/2008 – 09/2008 Max– Planck–Institut für Eisenforschung, Düsseldorf, Germany

01/2008 – 03/2008 Zentrum für Brennstoffzellentechnik, Duisburg, Germany

11/2007 – 12/2007 Heinrich–Heine Universität, Düsseldorf, Germany

03/2006 – 09/2007 Max– Planck–Institut für Eisenforschung, Düsseldorf, Germany